

Dissertation zur Erlangung des Doktorgrades
der Fakultät für Chemie und Pharmazie
der Ludwig-Maximilians-Universität München

**The control of neuronal activity and behavior by members of
the HCN and TPC family.**

Marc Sebastian Stieglitz

aus

Oberstdorf

2018

Erklärung

Diese Dissertation wurde im Sinne von § 7 der Promotionsordnung vom 28. November 2011 von Herrn Prof. Dr. Christian Wahl-Schott betreut.

Eidesstattliche Versicherung

Die Dissertation wurde eigenständig und ohne unerlaubte Hilfsmittel erarbeitet.

München, den 10.09.2018

(Marc Sebastian Stieglitz)

Dissertation eingereicht am: 10.09.2018

1. Gutachter: Prof. Dr. Christian Wahl-Schott

2. Gutachter: Prof. Dr. Martin Biel

Mündliche Prüfung am: 16.10.2018

Für meine Frau

*If the brain were so simple that we could understand it,
we would be so simple that we couldn't.*

- Emerson M. Pugh -

Table of contents

1	INTRODUCTION	1
1.1	Ion channels	1
1.2	Hyperpolarization-activated cyclic nucleotide-gated (HCN) channels	2
1.3	Two-pore channels (TPCs)	8
2	AIM OF THE STUDY	12
3	MATERIALS AND METHODS	13
3.1	Chemicals and solutions	13
3.2	Experimental animals	13
3.3	Working with nucleic acids	13
3.3.1	Genomic DNA isolation for genotyping	14
3.3.2	Polymerase chain reaction	14
3.3.3	Overlap extension PCR	15
3.3.4	Nucleic acid quantification	15
3.3.5	Tissue preparation and RNA extraction	15
3.3.6	First strand cDNA synthesis	16
3.3.7	Quantitative real-time PCR (qPCR)	16
3.3.8	Agarose gel electrophoresis	17
3.3.9	Gel extractions	17
3.3.10	DNA precipitation	18
3.3.11	Restriction enzyme digestion	18
3.3.12	DNA fragment ligation	18
3.3.13	Amplification and isolation of plasmid DNA	19
3.3.14	Cloning of the pAAV2.1-hSyn-Cre-p2A-eGFP	24
3.3.15	Cloning of vectors used for production of lentiviral particles (LV)	24
3.3.16	DNA Sequencing	26
3.4	Cell culture	26
3.5	Production of rAAVs	26
3.5.1	Transfection of HEK293T cells	26
3.5.2	Harvest	27
3.5.3	Iodixanol gradient centrifugation	28
3.5.4	Anion exchange chromatography	29
3.5.5	Concentration of rAAVs	29
3.5.6	rAAV titer determination	30
3.6	Production of lentiviral particles	31

Table of contents

3.6.1	Transfection of HEK293T cells	31
3.6.2	First and second harvest of lentiviral particles	31
3.6.3	Concentration of lentiviral particles	32
3.7	Immunohistochemistry	32
3.7.1	Cryo-sectioning of mouse brains	32
3.7.2	Staining of brain slices	32
3.7.3	Microscopy	33
3.8	Electrophysiology	34
3.8.1	Experimental setup	34
3.8.2	Acute brain slice preparation	34
3.8.3	Patch clamp protocols	35
3.8.4	Solutions used in patch clamp experiments	35
3.8.5	Analysis of electrophysiological data	37
3.9	Preparation of the intact septo-hippocampal formation	37
3.10	Stereotaxic surgery	38
3.11	Behavioral experiments	39
3.11.1	Circadian testing	39
3.11.2	Fear conditioning	40
3.12	Statistics	40
4	RESULTS	41
4.1	HCN channels in the mouse CNS	41
4.2	Establishment of new tools to study theta rhythm generation	52
4.3	The influence of TPC1 and TPC2 on spontaneous synaptic transmission	55
5	DISCUSSION	63
5.1	HCN3 and its role in regulating murine behavior	63
5.1.1	Expression of HCN3	63
5.1.2	Influence of HCN3 on auditory cued fear conditioning	64
5.1.3	HCN channels in the intergeniculate leaflet and their influence on circadian behavior	66
5.2	New tools to study theta rhythm generation	68
5.3	The influence of two-pore channels on spontaneous synaptic transmission	70
6	SUMMARY	75

Table of contents

7	BIBLIOGRAPHY	77
8	LIST OF FIGURES	85
9	LIST OF ABBREVIATIONS	86
10	APPENDIX	89
10.1	Primers used for PCR and qPCR experiments	89
10.2	Antibodies used	91
10.3	Publications	92
10.4	Acknowledgements	93

1 Introduction

The brain, the most complex of our organs, is the site where sensory information is integrated, consolidated and interpreted to govern physiological processes and complex behaviors. It is the organ that enables us not only to carry out voluntary or postural movements, but also higher cognitive functions such as motor learning, memory, language, creativity and many more are created and orchestrated by the complex interplay of diverse cell types found in the brain. The human brain consists of 86 billion neurons and tenfold as many glial cells such as astrocytes and oligodendrocytes [1]. Neurons are highly interconnected cells that can make contacts to tens of thousands of other neurons by structures called synapses. Often neurons are grouped into specific nuclei that send projection, association or commissural fibers to other parts of the brain and nervous system, allowing for the exchange and integration of information of different modalities [2]. To comply with their duties, neurons evolved to express a multitude of proteins and molecules, each with unique properties, enabling them to communicate or function as sensory, effector, or pace making cell.

1.1 Ion channels

In the brain, information is carried by electrical signals. For this to take place, specialized proteins are needed that serve as conductors for electrical activity, which is conferred by charged ions. In the nervous system, proteins that serve as gate for charged ions are called ion channels. They are transmembrane structures that form a pore allowing specific ions to be transported passively along their electrochemical gradient from one side of a biological membrane to the other. There are different ways how ion channels can be classified, for example by their gating mechanisms (e.g. voltage-gated, ligand-gated), the type of ions they pass (e.g. sodium, potassium, chloride), sequence homology (e.g. mucolipins), based on their location within the cell (e.g. plasma membrane, endoplasmic reticulum) or combinations of the defining factors [3].

Several families of ion channels are gated or modulated by second messengers. The term second messenger describes intracellular signaling molecules being released or produced upon exposure of the cell to first messengers, which are extracellular molecules that usually are unable to cross the cellular membrane and therefore bind to their receptors extracellularly. The extracellular signal is forwarded to the inside of the cell, then propagated intracellularly and often amplified to trigger physiological responses like maturation, gene expression, proliferation or apoptosis. Typical second messengers relaying the signal downstream include nucleotides

and dinucleotides such as cyclic adenosine/guanosine monophosphate (cAMP and cGMP, respectively) or nicotinic acid adenine dinucleotide phosphate (NAADP) and lipids such as diacylglycerol or phosphatidylinositol. Furthermore, gases like nitric oxide (NO) or carbon monoxide (CO) can serve as second messengers as well. In general, most second messenger systems share a common principle how the extracellular signal is forwarded intracellularly. First, an extracellular ligand binds to a receptor, which causes a conformational change in the receptor. This change can either lead to a modification of the receptor's activity, or to an exposure of a binding site for G proteins. The G protein binds to the receptor and activates by exchanging a guanosine diphosphate (GDP) for a guanosine triphosphate (GTP). The α subunit of the trimeric G protein detaches from the β and γ subunits and can activate a primary effector. The primary effector becomes activated and is eligible to produce the second messenger which in turn may exert its effects on secondary effectors like protein kinases or ion channels regulated by the messenger [4, 5].

1.2 Hyperpolarization-activated cyclic nucleotide-gated (HCN) channels

The group of ion channels being gated or modulated by second messengers is rather heterogeneous and can be classified according to the messengers they are sensitive to, the ions that pass through, or their localization in the cell. Large conductance potassium channels (BK channels) for example are gated by intracellular Ca^{2+} , are permeable to potassium (K^+) and usually reside in the plasma membrane. On the other hand, inositol trisphosphate (IP_3) receptors are gated by IP_3 , act as a Ca^{2+} channel and are mostly located to the endoplasmic reticulum.

Of particular interest for the current work is another family of ion channels gated by second messengers: hyperpolarization-activated cyclic nucleotide-gated (HCN) channels. They consist of four homologous subunits (HCN1-4), are nonselective cation channels mainly permeable for K^+ and Na^+ and are activated by hyperpolarization and gated by the cyclic nucleotides (second messengers) cAMP and cGMP. HCN channels confer a depolarizing inward current termed I_f (funny), I_q (queer) or I_h (hyperpolarization) that was discovered in the 1970s and 1980s in sinoatrial node cells and neurons [6, 7]. However, it took almost another 20 years until different groups were able to finally identify, clone and characterize HCN channels [8-11].

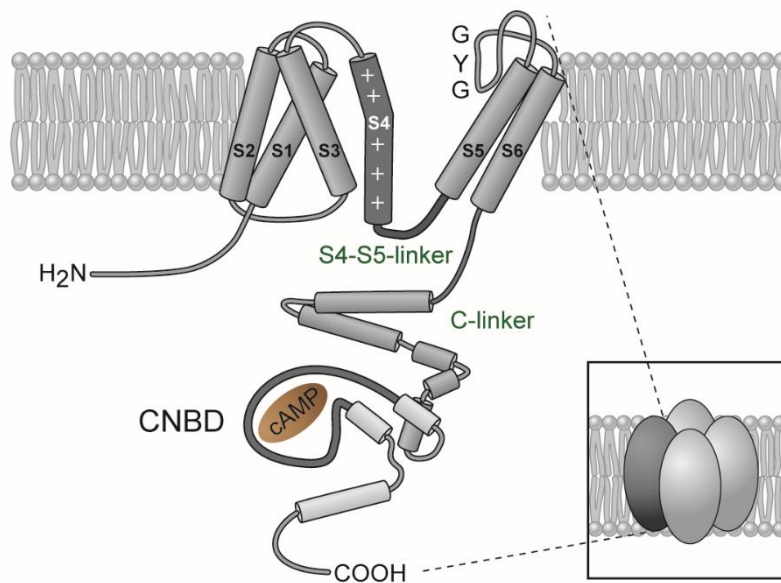


Figure 1 Schematic of a HCN channel subunit. One subunit consists of six transmembrane (TM) domains (S1-S6) and the intracellularly located N- and C-terminus. S5 and S6 form the pore that contains a GYG motif responsible for selectivity. S4 is the voltage-sensing segment exhibiting 9 positively charged amino acids. Deflections of the voltage sensor are propagated via the S4-S5-linker to the C-linker of a neighboring subunit (not shown for clarity). The C-terminus contains a cyclic nucleotide binding domain (CNBD), where cAMP or cGMP are able to bind. The image is adapted from [12].

Functional HCN channels are made up of four subunits and can occur as homo- or heterotetramers [13] (Figure 1). Each subunit consists of three domains: the cytosolic N-terminus, the core region, and the cytosolic C-terminus [14]. The most important domain is the channel core composed of six α -helical transmembrane (TM) segments (S1-S6), whereas S4 serves as voltage sensor and the pore is formed between segments S5 and S6. In line with other typical K^+ channels, the pore contains a glycine-tyrosine-glycine (GYG) motif that serves as the selectivity filter [15]. Despite the common GYG-motif, HCN channels are non-selective cation channels that also allow Na^+ ions to pass the pore. This phenomenon was recently explained using cryogenic electron microscopy structures obtained from HCN1 channels [16] (Figure 2A).

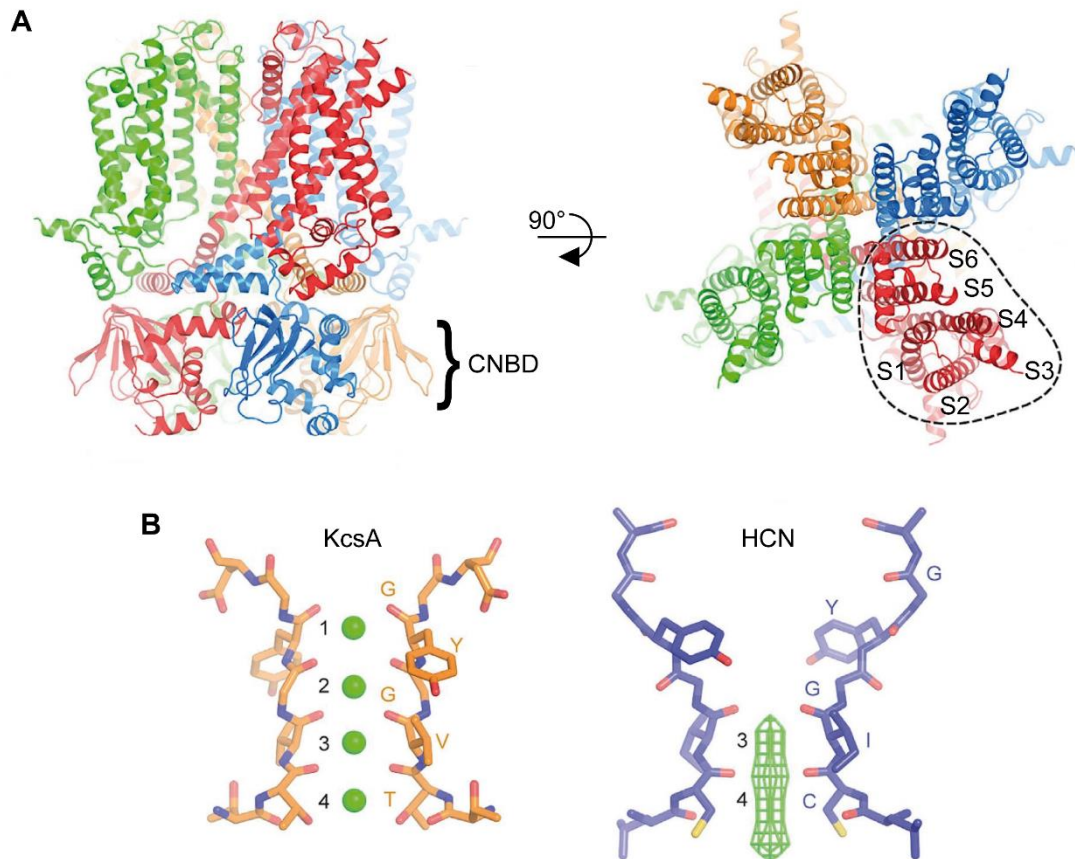


Figure 2 Structure of the human HCN1 channel. **(A)** Left: structure of a human HCN1 tetramer viewed from the side. Each subunit is shown in a different color (green, red, blue, orange). All four subunits contribute to form the cytosolic cyclic nucleotide binding domain (CNBD). Right: structure viewed from extracellular side. S1 – S6 from one subunit are encircled. **(B)** Selectivity filter of KcsA (left) and HCN channel (right). For details see text. Image is adapted from [16].

Usually, the selectivity of the GYG-motif for guiding K^+ ions is explained by the occurrence of four ion binding sites within the filter. When the selectivity filter of HCN1 channels was compared to the filter of KcsA potassium channels, it appeared that in HCN1 the tyrosine is differentially orientated than the tyrosine of the selectivity filter in KcsA channels (Figure 2B). Therefore, carbonyl oxygen atoms of the peptide backbone that would form two ion binding sites to coordinate K^+ ions are no longer facing the ion pathway, leading to a selectivity filter in HCN channels only preserving two of four binding sites [16], which explains the channel's non-selectivity.

HCN channels are opened upon hyperpolarization of the membrane potential. The sensor mainly responsible for voltage sensitivity is located in the S4 segment that exhibits positively charged amino acids (arginine or lysine) at every third position. When the cell is in a more depolarized state, the S4 segment extends into the cytoplasm where it brings its S4-S5-linker into contact with a neighboring C-linker. The force exerted onto the C-linker and consequently on the S6 segment will stabilize the channel's closed formation. Upon hyperpolarization, the S4 segment

is displaced, which releases the force onto the C-linker and S6 domain, thereby allowing the pore to open [14, 16]. On their C-terminal end, HCN channels possess a cyclic nucleotide binding domain (CNBD), where cAMP and cGMP are able to bind to the channel. It is connected to the S6 segment via the C-linker. Binding of cyclic nucleotides to the CNBD induces conformational changes that facilitate channel opening by removing channel inhibition, leading to faster opening kinetics and a shift of the voltage dependence towards more positive values. However, opening of the channels requires hyperpolarization and cannot be induced by binding of cyclic nucleotides alone.

The expression of HCN channel mRNA or protein has been shown primarily in the heart and nervous system, where they therefore have been studied extensively. Further studies suggested expression of HCN members in several other tissues, including pancreatic B cells, testis, or bladder smooth muscle cells, however, their function in these tissues remains elusive [12, 17-20]. In the mouse brain, all HCN channel isoforms are expressed, although differences in expression level and distribution are apparent. Experiments using *in situ* hybridization revealed that HCN1 channel transcripts are present in neocortex, hippocampus, brain stem and cerebellar Purkinje cells. HCN2 mRNA appears to be present throughout the whole brain, with highest levels in thalamic and brain stem nuclei. Contrarily, HCN3 transcripts are expressed only at low to moderate levels in hippocampus, thalamus and amygdala, and high expression seems to be restricted to olfactory bulb and hypothalamus. Furthermore, HCN4 is expressed at high levels only in a few brain regions, mainly in the olfactory bulb and the thalamus, whereas in many other areas very weak or no expression is found [21, 22].

On a physiological level, HCN channels were shown to fulfill several functions. For example, they are partially open at the resting membrane potential of many neurons, passing a depolarizing inward current that sets the resting potential to more depolarized values. Interestingly, HCN channels can function to counteract both, membrane hyperpolarizing as well as depolarizing influences. Hyperpolarization leads to the conduction of a depolarizing inward current (HCN channels are activated), and depolarization of the membrane in turn deactivates HCN channels, thus facilitates hyperpolarization by decreasing the depolarizing current. Both are mechanisms by which HCN channels stabilize the current membrane potential and control neuronal excitability. Furthermore, HCN channels are involved in several other basic and more complex neurophysiological processes as dendritic integration, synaptic transmission, learning, long-term potentiation or generation and maintenance of neural oscillations [12]. Remarkably, these contributions are mainly ascribed to either HCN1, HCN2 or HCN4 channels, whereas studies examining HCN3, especially in the mouse CNS, are sparse. HCN3 channel distribution was analyzed in the rat brain using immunohistochemistry where it was found to be expressed in

several brain areas including hypothalamic nuclei, nuclei of the amygdala, olfactory bulb and hippocampus [23]. In smaller studies performed in mice, HCN3 mRNA and protein were found to be expressed in the olfactory bulb, hypothalamus and to a lesser extent in hippocampus and amygdala [24, 25]. In addition, only very few studies addressed functioning of HCN3 channels in the rat brain [26-28] and similarly in the mouse brain [29, 30].

Notably, Ying and colleagues suggested that HCN3 is the main HCN channel found in a thalamic region named intergeniculate leaflet (IGL) and that it might have influence on the regulation of the circadian system [29]. The IGL is a structure found for example in rodents and cats, which is located between the dorsolateral and ventrolateral geniculate nucleus (dLGN and vLGN, respectively). In non-human primates and humans the pregeniculate nucleus is the homologue of the IGL [31]. The IGL is thought to be critically involved in the integration and transmission of photic and non-photoc entrainment cues to the suprachiasmatic nucleus (SCN) via the geniculohypothalamic tract (GHT) [32]. The SCN is located in the hypothalamus and considered the key player of circadian regulation in mammals (Figure 3). The SCN as well as the IGL receive direct input from photosensitive retinal ganglion cells via the retinohypothalamic tract (RHT) [33]. Apart from photic information from the retina, the IGL also receives inputs from areas such as the raphe nuclei or locus coeruleus, conveying for example information about arousal or availability of food. Both, photic and non-photoc stimuli are integrated in the IGL and transmitted to the SCN, thereby influencing circadian rhythms such as timing of wakefulness and sleep [32].

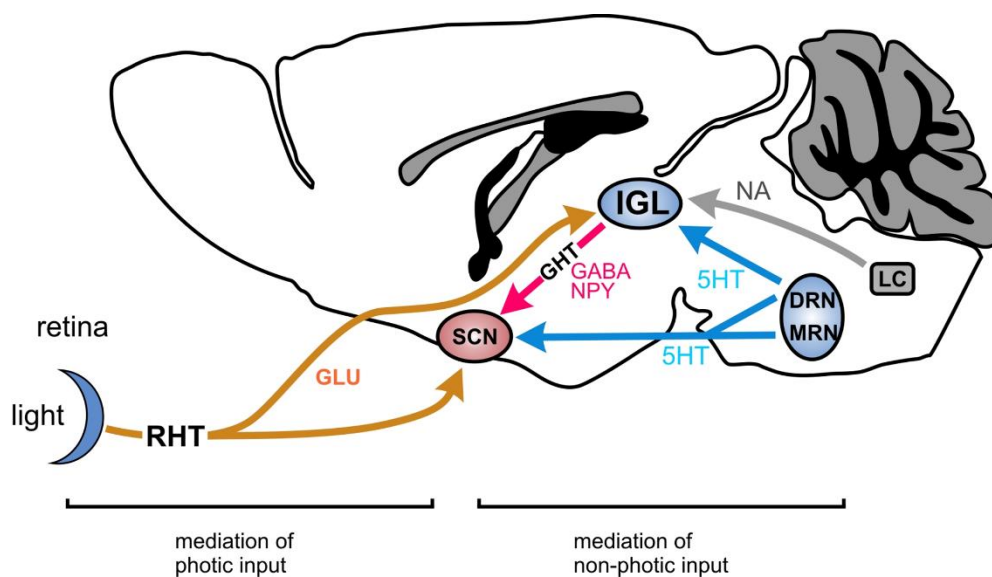


Figure 3 Main pathway of the circadian system in mammals involving SCN and IGL. Photic entrainment cues are conveyed to the IGL and SCN via a glutamatergic projection from the retina, the retinohypothalamic tract (RHT). Non-photoc cues converge on the IGL from dorsal raphe nuclei (DRN) and the locus coeruleus (LC) and other regions involved in the regulation of sleep, arousal and activity. Via the geniculohypothalamic tract (GHT), the IGL integrates these inputs and transfers them to the SCN. GLU, glutamate; GABA, gamma-aminobutyric acid; NPY, neuropeptide Y; 5HT, serotonin; MRN, median raphe nucleus.

Although the involvement of HCN3 channels in circadian regulation has been suggested, functional behavioral data supporting this hypothesis is still lacking, probably because other groups did not make use of a HCN3 knockout (KO) model yet. Previous work from this lab on HCN3 KO animals suggested that HCN3 might indeed influence mouse behavior, including motor stereotypies and locomotion [34], and this could also hold true for the regulation of circadian rhythms.

It has also been suggested that HCN channels are critically involved in the generation of the so-called theta rhythms. Theta rhythms are prominent neural oscillations in the 4-12 Hz frequency band that occur in the hippocampal formation and play an important role for information processing and for the organization of cognitive processes such as learning and memory [35, 36]. Theta oscillations are driven by the activity of the medial septum (MS), which is connected to the hippocampus via fornix fibers [37]. Stimulation of the MS results in theta rhythm generation [38], whereas ablation of the MS eliminates hippocampal theta [39]. In the literature, two different kinds of theta rhythms have been described. Type 1 theta rhythm can be observed during active behaviors such as locomotion, whereas type 2 theta is generated during passive whole body rotations, alert immobility, or target-oriented behavior such as exploration of novel objects [40-42]. The main pacemaker of theta rhythms, the MS, is composed of cholinergic, GABAergic and glutamatergic neurons, which contribute to theta rhythm generation. It appears that GABAergic pacemaker cells of the medial septum via the fornix project to hippocampal inhibitory interneurons, which in turn target the pyramidal cells of the hippocampus. Thus, activity of MS GABAergic neurons indirectly disinhibits hippocampal pyramidal cells rhythmically, contributing to the induction of theta rhythms [43]. GABAergic pacemaker neurons are able to fire in two different modes: tonic firing or low-threshold burst firing mode [44, 45], a feature similar to thalamocortical (TC) neurons [46]. Notably, in both types of neurons, Cav3.1 T-type calcium channels are expressed and deletion of these results in a loss of low threshold spikes and therefore loss of burst firing [42, 47], leaving the neurons locked in tonic firing mode. In the MS this has dramatic consequences for medial septum dependent behavior and theta rhythm. Type 2 theta increases, and so does the aforementioned object exploration. Interestingly, MS GABAergic and TC neurons also both contain HCN channels, mainly HCN2. When HCN2 channels were deleted in TC neurons, the result was the opposite to the deletion of Cav3.1 channels, hence, TC neurons were locked in burst mode [48]. Whether this opposing effect would also hold true for MS neurons has not been clarified to date. A pharmacological approach suggested that blocking MS HCN channels by application of ZD7288 decreases theta rhythms in the hippocampal formation [49, 50]. However, ZD7288 is a nonselective HCN channels blocker that might also have off-target effects. Furthermore, previous work from our

group further suggests that MS HCN2 channels are involved in theta rhythm generation, since MS-specific HCN2 KO animals show severe decreases in theta rhythm and consequently in spatial learning [51]. The possible mechanism behind theta reduction in MS-HCN2 KO animals still remains elusive. Additionally, clarity is needed to what extent the different families of MS neurons (GABAergic, glutamatergic, cholinergic) are involved in the generation or modulation of the theta rhythms.

1.3 Two-pore channels (TPCs)

Another family of ion channels investigated in the current work are two-pore channels (TPC) and when compared to HCN channels they exhibit differences in ion selectivity, modulation by second messengers and localization within the cell. The family of TPCs consists of three members (TPC1-3), whereas in humans and mice only the genes for TPC1 and TPC2 (*TPCN1* and *TPCN2*, respectively) code for functional channels, whereas *TPCN3* represents a pseudogene [52]. Two-pore channels mainly conduct Na^+ and Ca^{2+} and are modulated by phosphatidylinositol-3,5-bisphosphate (PI-3,5-P₂) as well as the second messenger NAADP. However, regarding TPC1 it is still debated whether NAADP influences channel activity or not [53-58]. Furthermore, except for TPC3 which can also be found in the plasma membrane, two-pore channels are located on intracellular organelles such as endosomes, lysosomes, melanosomes or plant vacuoles [57, 59, 60]. Based on their amino acid homology, TPCs are closely related to transient receptor potential (TRP) channels [61], however, while TRP channels are composed of four subunits with six TM domains each, functional TPCs consist of two subunits with 12 membrane-spanning helices each. From an evolutionary point of view, it appears that TPC subunits most likely are the result of a intragenic duplication of a six TM domain-containing subunit, meaning that two domains are already fused genetically [62]. Using X-ray crystallography, the structure of TPC1 from the plant *Arabidopsis thaliana* (AtTPC1) has been determined by two groups independently to a resolution of 2.87 and 3.3 Å [60, 63], and recently, using cryogenic electron microscopy, the structure of the mouse TPC1 (mTPC1) has been elucidated as well [64].

The general structure of a TPC1 subunit is depicted in Figure 4A and the crystal structure of mTPC1 in Figure 4B. One subunit consists of two 6-TM domains, domain I and domain II. The pore is formed between TM helices 5 and 6 of each domain (IS5-IS6 and IIS5-IIS6). Two pore helices (P1 and P2) that extend into the ion conduction pore are situated in-between S5 and S6 in both 6-TM domains [60, 63, 64]. TPC1 is a relatively non-selective cation channel, and the selectivity for positive ions is most likely explained by an accumulation of negatively charged

residues in the selectivity filter. AtTPC1 as well as mammalian TPC1 proteins are voltage-gated. Each subunit contains two voltage sensing domains (VSD), VSD1 (IS1-IS4) and VSD2 (IIS1-IIS4). However, it appears that voltage sensing is mainly mediated by VSD2, since it contains positively charged arginine residues in IIS4 and counter anion charge-transfer centers in IIS2 and IIS3. The VSD1 also contains arginines in IS4, but no charge-transfer center in IS2 and is therefore most likely not involved in voltage sensing but serves as a binding site for PI-3,5-P₂ [60, 64].

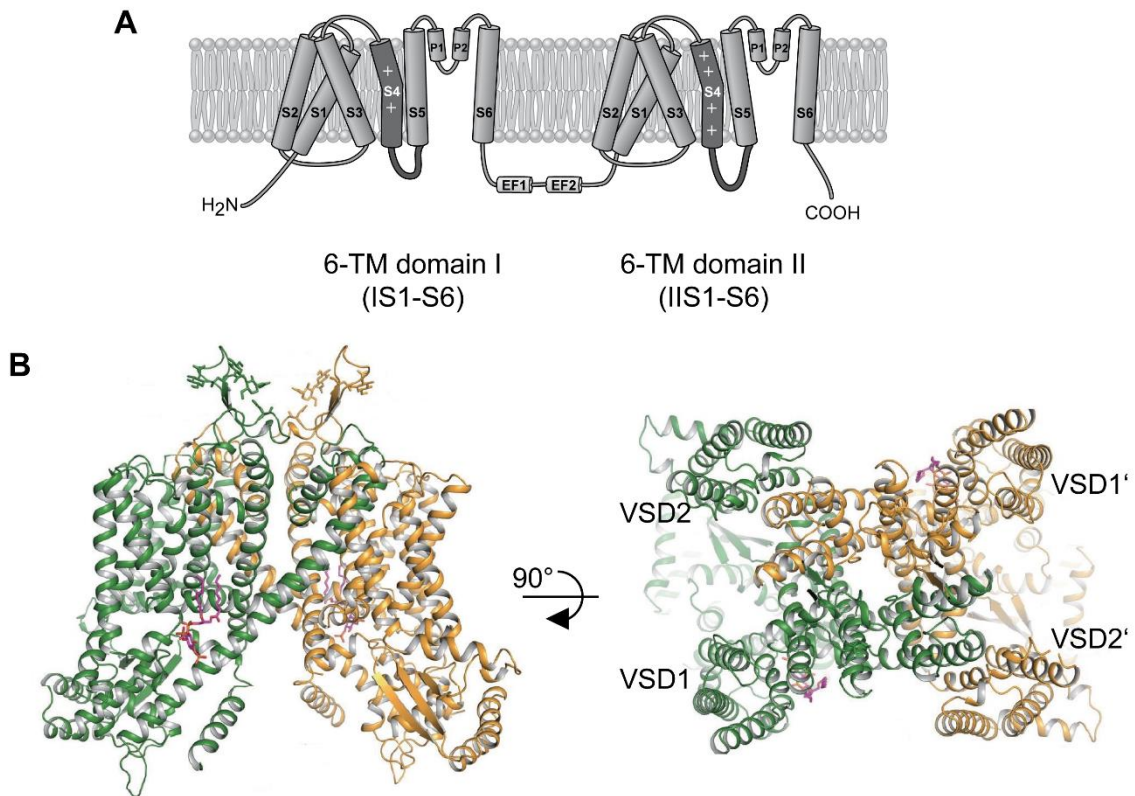


Figure 4 Topology diagram of a mouse TPC1 subunit. **(A)** The TPC1 subunit consists of two fused 6-TM domains (I and II), linked via two EF-hand domains (EF1 and EF2). Both, the C- and the N-terminal ends are facing the cytosol. IS5 and IS6 as well as IIS5 and IIS6 form the channel pore and contain two pore helices (P1 and P2) each. The IIS4 domain serves as voltage sensor. The IS4 domain is not predicted to form a functional voltage sensor, but rather a binding site for PI-3,5-P₂. **(B)** Structure of mTPC1 dimer from a side view (left) or viewed from luminal side (right). The first subunit is depicted in green, and domains from the other subunit in orange. The voltage-sensing domains from one subunit (VSD1 and VSD2) and the second subunit (VSD1' and VSD2') can be seen on the right. VSD2 and VSD2' serve as voltage sensor, whereas VSD1 and VSD1' likely serve as binding site for PI-3,5-P₂. PI-3,5-P₂ is depicted as purple stick. Figure 4B is adapted from [64].

Domain I and domain II of a TPC subunit are connected to each other via two EF-hands (EF1 and EF2) on the cytosolic side (Figure 4A). In AtTPC1, the EF-hands possess two Ca²⁺ binding sites each and can facilitate channel opening by Ca²⁺ ions binding to them. In mTPC1, although the EF hands are structurally similar to AtTPC1 EF hands, essential acidic residues for Ca²⁺ chelation are missing. Furthermore, TPCs contain a cytosolic N- and C-terminus, both being important for proper channel functioning, since deletion of either terminus results in non-operational

channels. The C-terminal region of mTPC1 appears to be longer than the AtTPC1 counterpart [64-66].

In animals, TPCs are located on acidic intracellular organelles of the endolysosomal system (endosomes and lysosomes). Over the last years, it has become evident that TPC2 is mainly found in the membrane of lysosomes, whereas TPC1 locates to different endosomes and generally exhibits a broader distribution in the endolysosomal system than TPC2 does [54, 67, 68]. The endolysosomal system and related organelles are implicated in the recycling and breakdown of several molecules, including lipids and proteins. Although distinct in pH, expression of proteins and in their function, the organelles of the endolysosomal system are closely associated with each other. The diverse endolysosomal organelles represent different stages of the recycling pathway and are eligible to advance into the next stage either by maturation into or by fusion with other organelles [69, 70]. Several studies suggested that TPCs are implicated in trafficking and fusion of such organelles. Exemplarily, Ruas and colleagues found that in mouse embryonic fibroblasts TPC1 is associated to the trafficking of cholera toxin B from the plasma membrane to the Golgi apparatus whereas TPC2 was important for breakdown of the ligand-induced platelet-derived growth factor receptor β , which depends on trafficking to lysosomes [71]. Furthermore, a recent study showed that both TPC isoforms play a role in filoviral infections, since mice lacking both channels were shown to be resistant to an infection with Ebola virus, which might be attributed to a defective virus trafficking [72]. Other studies investigating the role of TPC proteins also found involvement of those channels in cellular processes as exocytosis, nutrient sensing or autophagy [58, 73-75]. Despite the growing body of evidence that TPCs are implicated in numerous physiological processes that are also crucial for neuronal functioning, reports on how these channels could have influence on the central nervous system are scarce. Previous work from this lab points towards a function in transportation of endolysosomal vesicles [76].

Since TPCs have been associated with vesicular exocytosis [73] and neurons are specialized cells that commonly make use of this process, it is nearby to assume that two-pore channels could be involved in neuronal vesicle release as well. Principally, this assumption could be verified by performing patch clamp experiments in neurons of any given brain region where TPCs are expressed. Previous work performed in this lab detected TPC protein via western blot in the cerebellum, hippocampus, thalamus, and brainstem [76]. Hence, to examine the role of TPCs in spontaneous synaptic vesicle release, two different brain regions were chosen to perform patch clamp experiments – the hippocampus and the pre-Bötzing complex (preBötC). The hippocampus was selected for several reasons: (i) according to western blot and RT-PCR experiments TPCs are expressed in the hippocampus [76, 77]; (ii) it represents one of the most

studied brain regions in neuroscience and is implicated in important cognitive processes like learning and memory or spatial navigation [78, 79]; (iii) hippocampal neurons are clearly visible and easily accessible in patch clamp experiments. The other region relevant in context of in this thesis is the pre-Bötzinger complex. This brain stem region is located in the medulla oblongata as part of the ventral respiratory group and appears to be the site of respiratory rhythm generation [80-82]. As for the hippocampus, this nucleus was chosen due to the putative expression of TPCs in the brain stem, its implication in one of the most important physiological processes (breathing), and due to the fact that the medulla oblongata – compared to the hippocampus – represents a very old brain structure from an evolutionary point of view [83].

2 Aim of the study

HCN and two-pore channels are of great importance for basic neuronal functioning as well as for complex regulations of behavior. Although a great effort has been made to elucidate how HCN channels and TPCs influence cellular and systemic processes, many questions regarding their role in the central nervous system remain unanswered. Therefore, the current work aims to elucidate how HCN and TPC regulate basic neuronal functions and complex murine behavior.

In a first step, the expression of HCN3 channels in the murine CNS should be tested. Based on the expression in brain areas important for the control of distinct behavior, testing of WT and HCN3 knockout animals should be carried out to identify the role of HCN3 in the control of fear learning and circadian rhythmicity. In a further step, it should be tested whether HCN3 is the only HCN isoform in the IGL, a nucleus involved in circadian regulation, and perform additional behavioral testing if appropriate.

Another goal of the current thesis was to develop new tools and methods to examine the role of HCN2 in controlling neural oscillations. Previous work had suggested that HCN2 channels in medial septal neurons are critically involved in generating the hippocampal theta rhythm, and the new methods should be established to learn more about the nature of the neurons involved in theta rhythm generation. Furthermore, this thesis aims to clarify whether the endolysosomal channels TPC1 and TPC2 are expressed throughout the mouse CNS. Finally, it should be tested whether the knockout of either channel influences spontaneous synaptic vesicle release in the hippocampus and the pre-Böttinger complex.

3 Materials and methods

3.1 Chemicals and solutions

Unless stated otherwise, all chemicals used were obtained from Biorad, Merck, Roche, Roth, Sigma-Aldrich, or VWR chemicals. The quality of the chemicals was either “pro analysi” or “for molecular biology”. Working solutions were prepared with ultrapure and deionized water (Milli-Q water purification system, Merck Millipore). Solutions prepared for long-term storage were sterile-filtered or autoclaved and working solutions for sensitive applications (e.g. quantitative real-time PCR) were prepared using ISO 3696 grade 3 analytical water (AnalaR NORMAPUR, VWR chemicals).

3.2 Experimental animals

For this thesis, different strains of genetically modified mice - HCN3 KO, HCN2 L2, TPC1 KO, and TPC2 KO - and their respective WT littermates were used. All knockout lines have been generated beforehand, using a Cre/LoxP-based deletion strategy where an exon of the corresponding gene has been flanked with two LoxP-sites and excised upon expression of the Cre-recombinase. For HCN3 and TPC1 KO animals exon 3 of *HCN3* or *TPCN1* has been excised [84, 85], and for the deletion of TPC2 exon 7 of the *TPCN2* gene had been targeted [77]. HCN2 L2 animals still possess two LoxP-sites in their genome that flank exons 2 and 3 of *HCN2*. This strategy has been used to generate conditional HCN2 knockout animals upon stereotaxic delivery of Cre-containing viruses, since global HCN2 KO animals show severe impairments [48]. The mouse lines were mated homo- (HCN2 L2) or heterozygously (HCN3, TPC1, and TPC2) and animals were bred on a mixed 129SvJ / C57-B16/N background. Mice received food (Sniff; regular feed: R/M-H; breeding feed: M-Z Extrudat) and water *ad libitum* and were housed under a 12h light/dark cycle (lights on at 7 am) in accordance with legal regulations.

3.3 Working with nucleic acids

To avoid contamination with nucleases, all glassware and metal gear were baked at 200°C overnight, the filter tips used (VWR) were DNase and RNase free. When working with RNA, all surfaces were treated with RNase AWAY (Thermo Fisher Scientific).

3.3.1 Genomic DNA isolation for genotyping

For extraction of genomic DNA from mouse tissue, the samples were incubated with 50 mM NaOH for 10 min at 95°C. After adding 1 M TrisHCl (pH = 8), the samples were centrifuged for 6 min at 13,000 rpm and the DNA-containing supernatant was utilized for the polymerase chain reaction (PCR).

3.3.2 Polymerase chain reaction

The PCR is a method used for the amplification of DNA fragments. Here it was deployed on the one hand for genotyping animals, and on the other hand, to amplify DNA fragments needed to modify vectors (see 3.3.14 and 3.3.15). Depending on the experiment two different polymerases were used according to the manufacturers' instructions: GoTaq polymerase (Promega) for genotyping and high fidelity Q5 polymerase (New England Biolabs) for all other PCR reactions. The use of custom designed primers allowed the modification of the 5'- as well as the 3'-end of the fragments to, for example, adjoin specific palindromic sequences that are recognized by restriction enzymes. All primer sequences are listed in the appendix (see 10.1). For each pair of primers the annealing temperatures were calculated separately with help of the online tool Tm Calculator (version 1.9.8) at <https://tmcalculator.neb.com/#!/main>.

	PCR protocol GoTaq			PCR protocol Q5		
Initial denaturation	95°C	2 min		98°C	30 sec	
Denaturation	95°C	15 sec		98°C	15 sec	
Annealing	61-67°C	15 sec	38 cycles	58-72°C	15 sec	35 cycles
Elongation	72°C	1 min		72°C	1-2 min	
Final elongation	72°C	5 min		72°C	5 min	

PCR reaction mixture GoTaq		PCR reaction mixture Q5	
Primer 1 (10 μ M)	1.25 μ l	Primer 1 (10 μ M)	2.5 μ l
Primer 2 (10 μ M)	1.25 μ l	Primer 2 (10 μ M)	2.5 μ l
Primer 3 (10 μ M)	1.25 μ l	dNTP's	1 μ l
dNTP's	0.5 μ l	Buffer	10 μ l
10x buffer	2.5 μ l	Q5 Polymerase	0.5 μ l
Taq Polymerase	0.125 μ l	DNA	1-10 ng
DNA	2 μ l	H ₂ O	ad 50 μ l
H ₂ O	ad 25 μ l		

3.3.3 Overlap extension PCR

In order to fuse two DNA sequences of interest, the overlap extension PCR technique was used. An overlap-PCR consists of three polymerase chain reactions. In the parallel first two reactions, each DNA of interest is amplified using gene specific primers (see Appendix 10.1) containing an overlapping part of the corresponding gene of interest. In a third PCR reaction, both DNA product with the overlapping ends serve as templates. The combined DNA is generated using the terminal primer pair.

3.3.4 Nucleic acid quantification

Quantification of nucleic acids was performed using the Nanodrop™2000c spectrophotometer and the associated software (Thermo Fisher Scientific). Determination of DNA or RNA concentration was done by measuring the absorption at 260 nm wavelength. The nucleic acids were used in further experiments only when the 260/280 nm ratio, which provides information about possible protein contamination, exceeded a value of 1.8.

3.3.5 Tissue preparation and RNA extraction

Male mice, aged 1 and 8 weeks, were decapitated and their brains were removed. After the different brain regions (brainstem, cerebellum, cerebral cortex, hippocampus, hypothalamus, olfactory bulb, and thalamus) were separated using a scalpel and a fine spatula, they were shock frozen in liquid nitrogen in 2 ml Eppendorf tubes, and used within 20 min for RNA extraction. RNA was isolated from the tissue samples using the RNeasy Mini Plus Kit (Qiagen) according to the manufacturer's instructions. Briefly, tissue samples were homogenized in 600 μ l lysis buffer containing β -mercaptoethanol to inhibit ribonucleases and genomic DNA was eliminated via the

provided columns. After adding 600 μl of ethanol (70%) to the flow-through, the samples were applied to RNA-binding columns and contaminating molecules were removed by washing the columns with the provided solutions. The RNA was eluted in 30 μl H_2O and concentrations were measured.

3.3.6 First strand cDNA synthesis

From the samples obtained in 3.3.5, three reactions containing 5 μg of RNA each were prepared for reverse transcription. To this end, the RevertAid First Strand cDNA Synthesis Kit (Thermo Fisher Scientific) was used according to the manufacturer's protocol. In the first step, 0.5 μl each of Oligo dT- and random hexamer primers as well as water were added to the template RNA to a total reaction volume of 12 μl . Samples were incubated at 65°C for 5 min and cooled on ice before reaction buffer, RNase Inhibitor, dNTP's, and reverse transcriptase were appended to the reaction mix which was incubated for 5 min at 25°C followed by one hour at 42°C. The reaction was terminated by heating the samples to 70°C for 5 min. Afterwards, the three technical replicates were combined, diluted 1:4 with water, and samples were stored on -80°C until further usage.

3.3.7 Quantitative real-time PCR (qPCR)

Relative quantification of cDNA was performed using SYBR™ Select Master Mix (Thermo Fisher Scientific) and the StepOnePlus real-time PCR system (Applied Biosystems) according to manufacturer's instructions. The primers used (see appendix 10.1) were designed to be exon spanning to avoid amplification of possible contaminating genomic DNA and their amplification efficiency was calculated using the linear regression method [86] for each pair of primers with five cDNA dilutions (1:1; 1:2; 1:10; 1:100; 1:1,000). The threshold cycle (C_t) value was determined from two technical replicates and 2-3 biological replicates for all experiments. Relative quantification was done using hypoxanthine-guanine phosphoribosyltransferase (HPRT) and glyceraldehyde 3-phosphate dehydrogenase (GAPDH) as reference genes. HPRT is an enzyme involved in the purine salvage pathway and stably expressed among several tissues. GAPDH is an enzyme exhibiting an even broader distribution and is involved in glycolysis. Both enzymes show relatively stable expression and are regulated only to a low extent [87].

qPCR protocol			
Initial denaturation	95°C	3 min	
Denaturation	95°C	15 sec	
Annealing	60-65°C	10 sec	45 cycles
Elongation	72°C	15 sec	
Melting	95°C-40°C	~10 min	

qPCR reaction mix	
SYBR Select Master Mix	10 µl
Forward primer (5 pmol/µl)	1.1 µl
Reverse primer (5 pmol/µl)	1.1 µl
cDNA	6 µl
H ₂ O	1.8 µl

3.3.8 Agarose gel electrophoresis

DNA fragments of different sizes were separated using agarose gel electrophoresis. Agarose (peqGOLD, VWR) was solved in TBE buffer (Tris/Borate/EDTA) at different concentrations (0.7-2%), depending on the size of the expected fragments. Peq Green (VWR) was added to the gels to visualize DNA bands under UV light in a molecular imager (GelDoc 2000 or ChemiDoc Universal Hood III, both Bio-Rad). The DNA was separated at 130-190 V in horizontal electrophoresis chambers filled with TBE as running buffer. A 6x loading-dye (Thermo Fisher Scientific) was added to the DNA samples to pursue the course of the separation process. For comparison of the DNA fragment sizes, the 1 kb plus ladder (Thermo Fisher Scientific) was utilized.

3.3.9 Gel extractions

DNA bands were excised under UV light with disposable scalpels (Braun) and stored in 2 ml tubes. To resolve the DNA from the gel, the QIAquick gel extraction kit (Qiagen) was used according to manufacturer's instructions. First, three volumes of solubilization buffer were added and the tubes were incubated on a thermal shaker at 500 rpm and 50°C for 10 min. After adding one volume of Isopropanol (AnalaR NORMAPUR, VWR) and mixing by inverting, the DNA

was bound to the provided columns, washed with washing buffer and eluted with 30 μ l of elution buffer into fresh 1.5 ml tubes.

3.3.10 DNA precipitation

To precipitate DNA from aqueous solutions in order to purify or concentrate it, 0.1 volumes of sodium acetate (3M, pH = 5.2) and 3 volumes of ice cold ethanol were added to the DNA-containing solution. After 10 min of incubation on -80°C the solutions were centrifuged for 10 min at 13,000 rpm and 4°C , the supernatant was discarded and the DNA-pellet washed with 100 μ l of ethanol (70% in H_2O). Following another round of centrifugation (5 min, 13,000 rpm, 4°C) and removal of the supernatant, the DNA was resuspended 50-100 μ l H_2O .

3.3.11 Restriction enzyme digestion

To cut linear or plasmid DNA at specific palindromic sites, high fidelity restriction enzymes from Thermo Scientific were used according to the instructions. Depending on the concentration of the DNA that needed to be cut, a total reaction volume of 15 μ l (low concentration) or 50 μ l (high concentration) was prepared. After the digestion the DNA fragments needed for further use were purified via agarose gel electrophoresis (see 3.3.8) and gel extraction (see 3.3.9).

3.3.12 DNA fragment ligation

In order to insert DNA fragments into linearized vectors to produce modified cyclic plasmids, the T4 Ligase (Thermo Scientific) was used according to the appended protocol. Reactions were incubated at room temperature for 20-30 min and half of the reaction mixture was used for transformation of competent cells (see 3.3.13.2) thereafter. The other half was stored at 4°C as backup.

Ligation mixture	
10x T4 DNA ligase buffer	2 μ l
Linearized vector DNA	20-100 ng
Insert DNA fragment	2x to 5x molar ratio over vector
T4 DNA Ligase (5U/ μ l)	0.2 μ l
H_2O	ad 20 μ l

3.3.13 Amplification and isolation of plasmid DNA

Cloning of DNA fragments, as well as heterologous protein expression in cell culture systems requires the use of different purified plasmids. Plasmids are circular, double-stranded DNA molecules that are self-replicating when introduced into bacteria such as *Escherichia coli* (*E. coli*). In molecular biology synthetic plasmids – so called vectors – are used frequently. They usually possess a bacterial origin of replication, one or several selection markers (e.g. an antibiotics resistance gene), and a multiple cloning site (MCS). The MCS contains several palindromic sequences that are recognized by restriction enzymes and serves to introduce a gene of interest into the plasmid.

3.3.13.1 Plasmids

pAAV2.1

The pAAV2.1 is a plasmid used for heterologous expression of genes of interest delivered by recombinant adeno-associated viruses (rAAV). The vector serves as plasmid for inserting specific promoters and genes of interest to target the expression of the selected genes to a specific subpopulation of eukaryotic cells. The vector contains a MCS for DNA insertion and two inverted terminal repeats (ITR) encoding elements for the efficient replication and packaging of rAAVs upon co-expression with helper plasmids. Further, the plasmid possesses polyadenylation signal of the bovine growth hormone (pA BGH), an ampicillin resistance gene (Amp^R) for the selection of successfully transformed bacterial cells, and a woodchuck hepatitis virus posttranscriptional regulatory element (WPRE) for enhancement of gene expression. For efficient replication and packaging of the DNA into capsids, additional helper plasmids containing replication genes of serotype AAV2 and cap genes, e.g. of serotype AAV1 or AAV2, are needed. In the present thesis the pAD helper plasmid as well as the pAAV2/1 and pAAV2/2 replication/capsid plasmids were used to produce AAV particles.

pAAV2.1-hSyn-eGFP

This plasmid is based on the pAAV2.1 vector and possesses a human synapsin (hSyn) promoter regulating the expression of an enhanced green fluorescent protein (eGFP). It was used to produce AAV particles that later were injected into the thalamus of HCN2 L2 animals (see 3.10). It also served as template for the amplification of the hSyn promoter by PCR. The plasmid had been cloned and produced before the start of this thesis by Dr. Verena Hammelmann.

pAAV2.1-SWS-Cre-p2A-eGFP

This plasmid, based on the pAAV2.1 vector, possesses the retinal blue cone opsin promoter (short wavelength-sensitive, SWS) regulating the expression of a cassette composed of the information for a Cre-recombinase, a p2A sequence, and an eGFP. The p2A sequence encodes for a “self-cleaving” peptide and is used to generate two proteins (here Cre and eGFP) from one transcript. The plasmid was used for the production of the pAAV2.1 vector containing a hSyn promoter and the Cre-p2A-eGFP sequence (see 3.3.14). The plasmid was cloned and produced beforehand by Dr. Verena Hammelmann.

LV-Cre

LV-Cre is a plasmid used for heterologous expression of genes of interest delivered by lentiviruses. The plasmid serves as vector for inserting specific promoters and genes of interest to target the expression of the selected genes to specific populations of eukaryotic cells. This plasmid was purchased from Addgene (no 12106) where it was deposited to by Inder Verma [88]. The vector contains several cloning sites for DNA insertion and two long terminal repeats (LTR) encoding elements for the efficient integration of retroviral DNA via a specific integrase into the host chromosome. Between the two LTRs lies a polypurine tract, a cytomegalovirus (CMV) promoter, a WPRE element and a nuclear localization site (nls)-containing Cre-recombinase. Further, the plasmid possesses an ampicillin resistance gene (Amp^R) for the selection of successfully transformed bacterial cells.

LV-Syn1.1-eGFP

The LV-Syn1.1-eGFP is the plasmid that served as starting material for the cloning of several lentiviral (LV) plasmids. It consists of the LV-Cre backbone, a 1.1 kb fragment of the Syn promoter (Syn1.1) and an eGFP. Before the start of this thesis it had been produced by Dr. Verena Hammelmann based on the LV-Cre plasmid.

LV-Syn1.1-mCherry-HCN2

This LV plasmid cloned by Dr. Verena Hammelmann before the start of this thesis served as a template for the amplification of mCherry by PCR.

pMM403

The pMM403 plasmid was ordered from Addgene (no: 34926) where it was deposited to by the Mark Mayford lab. In the present work it was used to amplify a 1.2 kb fragment of the calcium/calmodulin- dependent protein kinase type II alpha chain (CaMKII α) [89]. This promoter was needed for lentiviral particles (see 3.3.15) which drive expression selectively in glutamatergic neurons.

pXGAD4eGFP

The pXGAD4eGFP plasmid [90] was ordered from Addgene (no: 25866) where it was deposited to by Sergey Kasparov. Here it was used to amplify a 3.7 kb fragment of the glutamic acid decarboxylase (GAD) 67 promoter needed for lentiviral particles (see 3.3.15) driving the expression selectively in GABAergic neurons.

TOPO Cre-t2A-GFP

The TOPO Cre-t2A-GFP plasmid [91] was ordered from Addgene (no: 68450) where it was deposited to by Tyler Jacks. In the present thesis it was used to amplify the Cre-t2A-GFP cassette needed for the production of lentiviral particles. Further, it served as cloning source for the production of a Cre-t2A-mCherry cassette (see 3.3.15).

Helper plasmids for the production of lentiviral particles

In order to produce lentiviral plasmids, the third generation of the HIV-1 derived delivery system was used. As a basis of this viral vector system, it is necessary to separate essential viral genes responsible for replication and production of infectious particles from genes responsible for the pathogenesis of HIV-1. Hence, the native HIV envelope (*env*) is the limiting factor for the use of lentivirus in biological research and therefore it was replaced by coating proteins of heterologous viruses. Commonly, the vesicular stomatitis virus g-protein (VSV.G) is used for pseudotyping [92] which is located in the helper plasmid pMD.2G. In order to reduce the risk of homologous recombination and the resulting production of infectious particles, the HIV genes *vif*, *vpr*, *vpu* and *nef* were removed from the lentiviral genome [93]. The *tat* trans-gene is also non-essential for the efficient production of lentiviral vectors and was replaced by a strong heterologous promoter sequence. An essential part is the *rev* gene which interacts with the *rev* response element (RRE) and enhances the export of the unspliced, full-length genome

transcripts of gag-pol mRNA and the genomic RNA of the transfer vector [93]. In the vector system, the rev gene is located on the pRev and the gag-pol on the pMDL, respectively. The latter encodes a gag-pol precursor protein which is processed to an integrase, a reverse transcriptase and structural proteins essential for the lentivirus particle production.

3.3.13.2 Transformation of *Escherichia coli*

A strain of chemically treated, competent β 10 *Escherichia coli* (*E. coli*, New England Biolabs) was used for transformation with purified plasmid DNA or ligation products. Competent bacteria were stored on -80°C and 100 μl aliquots were thawed on ice. 5-10 μl of the ligation reaction or 5-10 ng of purified plasmid DNA were added. The suspension was mixed by gently pipetting up and down and incubated on ice for 10 min. Thereafter, a heat shock at 42°C was applied in a thermal shaker for 45 seconds and the cells were subsequently incubated for 2 min on ice prior to plating on a LB (+) selection agar plate containing either ampicillin or kanamycin, depending on the resistance provided by the plasmids used. In cases where kanamycin was used, the cell suspension was first incubated for 1 h at 37°C . Plated cells were incubated at 37°C overnight.

LB (+) medium		LB (+) agar	
Peptone	10 g	Agar	15 g
NaCl	5 g	LB (+) medium	Ad 1 l
Yeast extract	5 g	Ampicillin/kanamycin	100 mg
Glucose	1 g		
H ₂ O	ad 1 l		
Adjust to pH 7.4 and autoclave			

3.3.13.3 Inoculation of bacterial cells and alkaline lysis

Colonies of single bacterial clones were picked from the selection plate and transferred into 13 ml tubes (Sarstedt) containing 5 ml of LB (+) medium and ampicillin (100 $\mu\text{g}/\text{ml}$). The suspension was incubated overnight at 37°C and 225 rpm in a thermal shaker. In cases where kanamycin was used, the cell suspension was first incubated for 1 h at 37°C before the antibiotic was added to the tubes. The next day, the suspension was centrifuged at 3500 rpm for 10 min and the supernatant was removed. Thereafter, the bacterial cells were resuspended in 250 μl resuspension buffer and transferred into a 1.5 ml tube before 250 μl of lysis buffer were added. The suspension was mixed by inverting and was allowed to incubate for 5 min at RT. Then 250 μl

of neutralization buffer was added and after a short incubation time the mixture was centrifuged at 13,000 rpm and 4°C for 15 min. The plasmid DNA-containing supernatant was transferred to a fresh 1.5 ml tube and 525 µl of Isopropanol was added for precipitation. The samples were mixed thoroughly and centrifuged at 13,000 rpm and 4°C for 5 min. After removing the supernatant, the DNA pellet was washed with 70% ethanol and centrifuged at 13,000 rpm and 4°C for 5 min. The ethanol was removed and the pellet was allowed to air dry before being resuspended in 30 µl H₂O.

Resuspension buffer	
Tris	6.06 g
EDTA	3.72 g
RNAse A	100 mg
H ₂ O	ad 1 l
Adjust to pH 8 with 37% HCl	

Lysis buffer	
NaOH	8 g
SDS solution (10%)	100 ml
H ₂ O	ad 1 l

Neutralization buffer	
3 M potassium acetate	500 ml
H ₂ O	ad 1 l

3.3.13.4 Medium scale plasmid preparation

The commercially available PureLink HiPure Plasmid Midiprep kit (Invitrogen) was used for larger scale plasmid isolation according to the manufacturer's instructions. Briefly, bacterial colonies picked from selection agar plates were transferred into Erlenmeyer flasks containing 200 ml of LB (+) medium 100 µg/ml ampicillin. After overnight incubation at 37°C and 225 rpm, the suspension was portioned into 50 ml falcon tubes (Sarstedt) and centrifuged at 4000 g and RT for 10 min. Meanwhile, the provided columns were equilibrated with equilibration buffer. The bacterial pellets were resuspended in a total volume of 4 ml resuspension buffer and merged into one tube before adding 4 ml of lysis buffer and 5 min incubation at RT. Then, 4 ml of

precipitation buffer was added and the suspension was mixed by inverting the tube before the lysate was centrifuged at 12,000 g and RT for 10 min. The supernatant was added to the columns and after draining the columns were washed twice with 10 ml of washing buffer. To elute the plasmid DNA the columns were placed into a fresh 50 ml tube and 5 ml of elution buffer was added. Precipitation was carried out by adding 3.5 ml isopropanol to the eluate and after mixing the tubes were centrifuged at 12,000 g and 4°C for 30 min. The supernatant was removed and the DNA pellets were washed with 70% ethanol before being air-dried. The purified plasmid DNA was resuspended in 200 µl TE buffer.

3.3.14 Cloning of the pAAV2.1-hSyn-Cre-p2A-eGFP

To produce a plasmid consisting of the pAAV2.1 backbone, a hSyn promoter, and a Cre-p2A-eGFP cassette the two plasmids pAAV2.1-hSyn-eGFP and pAAV2.1-SWS-Cre-p2A-eGFP were used as templates. An overlap PCR approach was chosen since the different plasmids had no matching restriction sites to simply replace the SWS promoter by the hSyn promoter. Therefore, primer pairs were designed for the amplification of the hSyn promoter (primers A and B) in the first PCR reaction (PCR1) and for the amplification of a part of the Cre-p2A-eGFP cassette (primers C and D) in a second PCR reaction (PCR2). Primers A (PCR1) and D (PCR2) were designed to produce an overhang that can be recognized by specific restriction enzymes (NheI and EcoRV, respectively) later in the procedure and the primers B (PCR1) and C (PCR2) were designed such as they would produce an overhang being complementary to a part of the product from the other PCR reaction. In a subsequent reaction (PCR3), the two products were combined to serve as template for the amplification of the desired hSyn-Cre fragment when amplified using the primers A and D together. In a final step, the Product of PCR3 was incorporated into the pAAV2.1-SWS-Cre-p2A-eGFP plasmid. Therefore, the plasmid was cut with NheI and EcoRV leading to a linearized plasmid with “sticky-ends” lacking the SWS promoter and a part of the Cre-recombinase. The hSyn-Cre fragment was cut with the same enzymes to produce corresponding sticky ends and the plasmid and PCR product were ligated (see 3.3.12) to form the desired plasmid pAAV2.1-hSyn-Cre-p2A-eGFP.

3.3.15 Cloning of vectors used for production of lentiviral particles (LV)

For the production of lentiviral particles (see 3.6) the following 12 plasmids were amplified or produced:

Plasmid	Plasmid name
#1	LV-Syn1.1-eGFP
#2	LV-Syn1.1-mCherry
#3	LV-Syn1.1-Cre-t2A-eGFP
#4	LV-Syn1.1-Cre-t2a-mCherry
#5	LV-CamKII α -eGFP
#6	LV-CamKII α -mCherry
#7	LV-CamKII α -Cre-t2A-eGFP
#8	LV-CamKII α -Cre-t2A-mCherry
#9	LV-GAD67-eGFP
#10	LV-GAD67-mCherry
#11	LV-GAD67-Cre-t2A-eGFP
#12	LV-GAD67-Cre-t2A-mCherry

In general, the LV-Syn1.1-eGFP plasmid (#1), provided by Dr. Verena Hammelmann, served as starting material for the LV-backbone, i.e. the other 11 LV-plasmids used in 3.6 are derived from this vector. In a first step, the eGFP was replaced by mCherry, leading to #2. To do so, mCherry was amplified from the LV-Syn1.1-mCherry-HCN2 vector using primers producing 5'- and 3' overhangs that can be recognized by specific restriction enzymes (see appendix 10.1). Plasmid #2 was then established by digestion of #1 (leading to a linearized vector where eGFP is deleted) and mCherry with the corresponding restriction enzymes and ligation of the two DNA fragments. For the production of #5 and #6 a 1.2 kb fragment of the CamKII α promoter was amplified with the pMM403 plasmid as template using primers producing restriction enzyme recognition sites at the 5' and 3' end (see appendix 10.1). The Syn1.1 promoter of #1 and #2 was excised by digestion and the CamKII α promoter was inserted in place. The plasmids #9 and #10 were produced in a similar way after amplification of a 3.7 kb fragment of the GAD67 promoter from the pXGAD4eGFP plasmid. To build the plasmids containing the Cre-t2A fragment, the TOPO-Cre-t2A-GFP plasmid served as template. To create a second TOPO vector, TOPO-Cre-t2A-mCherry, the mCherry was again amplified from LV-Syn1.1-mCherry-HCN2, however, primers containing different restriction enzyme recognition sites were used (see appendix 10.1). After deleting the GFP, the mCherry was ligated into the TOPO vector. The Cre-t2A-GFP and the Cre-t2A-mCherry cassettes were amplified from the TOPO vectors and replaced the eGFP cassette of the existing vectors to produce #3, #4, #7, #8, #11, and #12.

3.3.16 DNA Sequencing

To verify correct DNA sequences, all modified plasmids were sequenced by the external service provider Eurofins Genomics. The primers used for sequencing were designed in-house and ordered from Eurofins Genomics as well. Primers used can be found in the appendix (see 10.1)

3.4 Cell culture

All work with mammalian cell lines was carried out either in a biosafety level 1 or biosafety level 2 laboratory in biological safety cabinets (HERAsafe, Thermo Fisher Scientific) and cells were maintained at 37°C and 10% CO₂ in incubators (HERAcell, Thermo Fisher Scientific). For the generation of rAAV and lentiviral particles (see 3.5 and 3.6) HEK293T cells were used and maintained in DMEM + GlutaMAX medium containing 4.5 g/l glucose (Life technologies), 10% fetal bovine serum and 1% penicillin/streptomycin (both Biochrom).

3.5 Production of rAAVs

3.5.1 Transfection of HEK293T cells

HEK293T cells were grown in cell culture plates (Cellstar 145 mm, Greiner) and transiently transfected using the calcium phosphate method. The following reaction mix was used for 15 cell culture plates:

Transfection mix	
Hexadimethrine bromide (8 mg/ml)	17.5 µl
Dextran (10 mg/ml)	1750 µl
pAAV2.1 construct	270 µg
pAD helper plasmid	X µg
pAAV2/1 / pAAV2/2 replication/capsid (50:50)	Y µg
CaCl ₂ (2.5 M)	1750 µl
H ₂ O	ad 17.5 ml

The amount of helper and replication/capsid plasmids needed was calculated according to following formulas:

$$X \mu\text{g} = (270 \mu\text{g} / \text{molecular mass pAAV2.1 construct}) * \text{molecular mass pAD helper plasmid}$$

$$Y \mu\text{g} = (270 \mu\text{g} / \text{molecular mass pAAV2.1 construct}) * \text{molecular mass rep-cap plasmid}$$

While vortexing the transfection mix, 17.5 ml of 2x BBS was added dropwise before the mix was allowed to incubate at RT for 12 min to facilitate the formation of homogenous DNA complexes. Then 2.3 ml of transfection solution was added to each cell culture plate dropwise. The HEK293T cells were incubated at 37°C and 5% CO₂ overnight before fresh medium was added, and cells were placed back to 10% CO₂ for 24 – 30 h.

2x BBS	
BES	8 g
NaCl	13.08 g
NaH ₂ PO ₄	0.17 g
H ₂ O	ad 800 ml
Adjust to pH 6.95 with NaOH, sterile filtrate	

3.5.2 Harvest

The transfected cells were abraded off the plates using a cell scraper (VWR) into autoclaved 500 ml centrifugation beakers and centrifuged at 4,000 rpm at 4°C for 15 min (J2-MC centrifuge, JA-10 rotor, Beckman Coulter). The supernatant was removed and the cell pellet resuspended in 7.5 ml lysis buffer and transferred into a 50 ml falcon tube. The cell suspension underwent three cycles of shock-freezing on liquid nitrogen and thawing at 37°C in a water bath, before being stored at -80°C overnight.

Lysis buffer	
NaCl	150 mM
Tris-HCl pH = 8.5	50 mM
Sterile filtrate	

3.5.3 Iodixanol gradient centrifugation

The next day the lysed cells were thawed at 37°C and benzonase was added to a final concentration of 50 U/ml. After 30 min incubation at 37°C cells were pelleted by centrifugation (2,000 g, 25 min, 4°C). The virus-containing supernatant was transferred into a Beckman Quickseal polypropylene tube (Beckman Coulter) and for gradient centrifugation underlain with 7 ml 15% iodixanol, 5 ml 25% iodixanol, 5 ml 40% iodixanol, and 6 ml 60% iodixanol using a sterile glass pipette and a Gilson Minipuls3 pump. The tubes were balanced with PBS-MK and sealed with the Beckman Tube Topper before being centrifuged at 361,000 g for 105 min at 18°C (Optima LE-50K ultracentrifuge, 70 Ti rotor, Beckman Coulter). Afterwards, the top of the tube was pierced with a needle several times for pressure balance, since the 40% phase containing the virus was collected by piercing the tube at the 60-40% interface with a 20-gauge needle attached to a 5 ml syringe (Braun) and aspirating the 40% phase. The virus-containing phase was stored on -80°C until further purification (see 3.5.4).

15% iodixanol		25% iodixanol	
10x PBS	5 ml	10x PBS	5 ml
MgCl ₂ 1 M	50 µl	MgCl ₂ 1 M	50 µl
KCl 2.5 M	50 µl	KCl 2.5 M	50 µl
NaCl 5 M	10 ml	Optiprep	20.9 ml
Optiprep	12.5 ml	1% (v/v) phenol red	50 µl
1% (v/v) phenol red	37.5 µl	H ₂ O	ad 50 ml
H ₂ O	ad 50 ml	Sterile filtrate	
Sterile filtrate			

40% iodixanol		60% iodixanol	
10x PBS	5 ml	MgCl ₂ 1 M	50 µl
MgCl ₂ 1 M	50 µl	KCl 2.5 M	50 µl
KCl 2.5 M	50 µl	Optiprep	50 ml
NaCl 5 M	10 ml	1% (v/v) phenol red	37.5 µl
Optiprep	33.3 ml	H ₂ O	ad 50 ml
H ₂ O	ad 50 ml	Sterile filtrate	
Sterile filtrate			

Tween/PBS-MK	
10x PBS	50 ml
MgCl ₂ 1 M	500 µl
KCl 2.5 M	500 µl
Tween20	0.014% (v/v)
H ₂ O	ad 500 ml
Sterile filtrate	

3.5.4 Anion exchange chromatography

Viral particles were purified using the ÄKTAprime plus chromatography system and a HiTrap Q FF sepharose column (GE Healthcare Life Sciences). First, the column was equilibrated with 30 ml of buffer A (10 ml/min flow rate) and the subsequent manual run was set at 1 ml/min flow rate and 1 ml fraction size. The virus-containing phase was diluted 1:1 in buffer A and injected into the super loop. 1 ml fractions were collected in 1.5 ml tubes and UV- as well as conductance-curves were monitored via the PrimeView software. When the conductance curve returned to baseline values, the system was loaded with buffer B to clear the column from remaining virus particles. To eliminate the remaining salt in the column, the system was cleaned with double distilled water (ddH₂O). As the conductance curve reached zero, washing proceeded for 20 more min. Fractions collected at the peak of the conductance curve were combined and concentrated (see 3.5.5).

Buffer A		Buffer B	
Tris	20 mM	NaCl	2.5 M
NaCl	15 mM	H ₂ O	ad 1 l
H ₂ O	ad 1 l		
Adjust to pH = 8.5 and sterile filtrate		Adjust to pH = 8.5 and sterile filtrate	

3.5.5 Concentration of rAAVs

To gain virus solutions with a high titer, the combined fractions collected in 3.5.4 were applied to an Amicon centrifugal filter unit (Merck Millipore) and centrifuged at 2,000 g and 20°C for 20 min (J2-MC centrifuge, JA-10 rotor, Beckman Coulter). After discarding the flow-through, this procedure was repeated until the whole parent material had been centrifuged and 500 µl of

solution remained above the filter. To wash the filter, 1 mL of 0.014% Tween/PBS-MK solution was added and after mixing by pipetting the solution was centrifuged in 5-10 min steps until ~100 µl of concentrated virus suspension remained in the filter. The ready-to-use virus suspension was aliquoted in 1.5 ml screw cap tubes (Eppendorf) and stored on -80°C until rAAV titer determination (see 3.5.6) and use in stereotaxic injections (see 3.10).

3.5.6 rAAV titer determination

Determination of the rAAV genomic titer was performed using qPCR. Briefly, the WPRE element of the pAAV2.1 vector was amplified by a PCR reaction first (for primers see appendix 10.1). Then the element was purified and its concentration was measured (see 3.3.8, 3.3.9, and 3.3.4). The following equation was used to calculate the concentration of the standard for 10^{10} genomic copies per 5 µl:

$$c = 10^{10} * 660 * 10^{12} \text{ pg/mol} * \text{WPRE fragment size} / (6.022 * 10^{23} / \text{mol} * 5 \text{ } \mu\text{l})$$

whereas $660 * 10^{12}$ pg/mol = mean molar mass of one base pair, and $6.022 * 10^{23}$ is the Avogadro constant. Using this information, a 10-fold serial dilution was generated with the first dilution containing 10^{10} copies / 5µl and the last dilution containing 10^1 copies / 5 µl. The dilutions were tested in a qPCR experiment (see 3.3.7) and the standard curve was calculated by plotting the logarithmized solutions against the C_t values. Then, the rAAV solutions generated in 3.5.5 were diluted 1:500 in H₂O and qPCR was executed using the WPRE forward and WPRE reverse primers (see appendix 10.1). The genomic titers were calculated by correlation of the obtained C_t values to the standard curve.

qPCR reaction mix	
SYBR Select Master Mix	10 µl
Forward primer (10 µM)	1 µl
Reverse primer (10 µM)	1 µl
Template	5 µl
H ₂ O	ad 20 µl

3.6 Production of lentiviral particles

3.6.1 Transfection of HEK293T cells

HEK293T cells were grown in cell culture plates and transiently transfected using the calcium phosphate method. The following reaction mix was used for 6 cell culture plates:

Transfection mix	
LV construct	108 µg
pMDLg/pRRE	70 µg
pRSV-Rev	30.8 µg
pMD2.G	29.2 µg
CaCl ₂ (2.5 M)	700 µl
H ₂ O	ad 7 ml

While vortexing the transfection mix, 7 ml of 2x BBS was added dropwise before the mix was allowed to incubate at RT for 12 min to facilitate the formation of homogenous DNA complexes. Then 2.3 ml of transfection solution was added to each cell culture plate dropwise. The HEK293T cells were incubated at 37°C and 5% CO₂ overnight before fresh medium was added and cells were placed back to 10% CO₂ for 24 – 30 h.

3.6.2 First and second harvest of lentiviral particles

The medium containing the lentiviral particles was collected in a 125 ml Rapid-Flow filter unit (VWR) and filtered by the application of a vacuum. The flow-through was collected into 30 ml conical centrifugation tubes (Beckman Coulter) and these were placed into the swing-out buckets of the Beckman SW28 rotor. The samples were balanced using Hanks' balanced salt solution (HBSS, Life technologies) and centrifuged at 19,400 rpm and 17°C for 2 h (Optima LE-50K ultracentrifuge). After discarding the supernatant, pellets were resuspended in 50 µl HBSS and tubes were rinsed with 200 µl HBSS. The virus-containing solution was stored in screw cap tubes at 4°C until the second harvest was performed using the same protocol the next day.

3.6.3 Concentration of lentiviral particles

The yield of both harvest was combined in a 3 ml conical centrifugation tube (Beckman coulter) that was placed into the swing-out buckets of the Beckman SW55 rotor. Using HBSS the samples were balanced and centrifuged at 21,000 rpm and 17°C for 2h. The pelleted lentiviral particles were resuspended in 50 μ l HBSS and the tubes were rinsed with another 20 μ l of HBSS before the solution was transferred to screw cap tubes and mixed by vortexing. After mixing the samples for 45 minutes at RT and 1,400 rpm in a thermal shaker, they were briefly centrifuged and the supernatant was aliquoted into screw cap tubes. Lentiviral particles were stored on -80°C until further usage.

3.7 Immunohistochemistry

To detect proteins such as HCN channels in native tissues, immunohistochemistry (IHC) was performed on cryo-sectioned mouse brain slices.

3.7.1 Cryo-sectioning of mouse brains

Animals were anaesthetized with Isoflurane (Baxter) and decapitated. The brains were carefully removed and submerged in -20°C to -30°C cold isopentane (AppliChem) for freezing. When frozen, brains were directly processed or stored on -80°C until further usage. Before cryo-sectioning, brains were allowed to adapt to the ambient temperature (-24°C) in the cryostat (CM3050 S, Leica) and mounted onto a cutting plate with embedding medium (Tissue-Tek O.C.T., Sakura Finetek). Three to four serial coronal brain sections (12 μ m) were fused to one superfrost plus microscopic slide (Thermo Fisher Scientific) and allowed to air dry for 20 min before being stored on -25°C until further usage.

3.7.2 Staining of brain slices

The microscopic slides were allowed to thaw at RT before the brain slices were surrounded by a hydrophobic barrier using a liquid blocker (PAP pen, Science Services). Slices were then rehydrated for 5-10 min with 100 μ l of PBS each before being post-fixed by application of 4% PFA in PBS for 3-10 minutes. Alternatively, brain slices were fixed by being submerged in ice-cold methanol (AnalaR NORMAPUR, VWR) for 3-20 minutes. Subsequently, the slices were washed three times with PBS for 5 min. The blocking and permeabilization solution containing

10% ChemiBlocker (Millipore) and 0.3% Triton-X100 in PBS was applied for at least 1 hour. The incubation of the slices with the primary antibodies (see appendix 10.2) diluted in PBS containing 5% ChemiBlocker and 0.2% Triton-X100 was carried out overnight at 4°C. The next day slices were washed with PBS at least thrice for 5 minutes. Slices were then incubated with secondary antibody (see appendix 10.2) diluted in PBS containing 2% ChemiBlocker and 0.1% Triton-X100. After washing with PBS nuclei were stained using 5 µg/ml Hoechst 33342 for 3 minutes, before being washed again twice with PBS. Cover slips (Menzel-Gläser) were mounted onto the brain slices using Fluoromount-G Slide mounting medium (Thermo Fisher Scientific) and the dried slices were stored shielded from light on 4°C until analysis. For HCN channel staining, endogenous peroxidases were inactivated by incubation of the brain slices with 3% H₂O₂ in methanol for 10 minutes before the secondary horseradish peroxidase antibodies were applied. Subsequently, a tyramide signal amplification (TSA) step was performed. Thereby, brain slices were incubated for 5 min with self-made amplification buffer followed by incubation with PE-tyramide diluted 1:50 in TSA amplification buffer (Perkin Elmer) for 8 min and two washing steps with PBS.

Amplification buffer	
NaCl	0.15 M
Tris-HCl	0.1 M
Adjust to pH = 8 with HCl	

PBS	
NaCl	8 g
KCl	0.2 g
Na ₂ HPO ₄	1.42 g
KH ₂ PO ₄	0.27 g
H ₂ O	Ad 1 l
Adjust to pH 7.4 and autoclave	

3.7.3 Microscopy

Images of immunohistochemically stained brain slices were obtained with the TCS SP8 confocal laser scanning microscope (Leica). Images were obtained using the LASX software (Leica).

3.8 Electrophysiology

Electrophysiological recordings were carried out between 11 am and 5 pm in acute brain slices of animals sacrificed between 7 and 8 am. Patch clamp experiments were performed only in coronal sections containing either the IGL, the hippocampus, or the pre-Bötzing complex. The relevant brain regions were identified using the standard mouse brain atlas [94].

3.8.1 Experimental setup

Brain slices were visualized and neurons identified using a Zeiss Axioskop 2 equipped with a 5x objective, a 40x water-immersion objective and an infrared camera (VX55, Photonics). Electrical signals were obtained using an EPC 10 amplifier and PatchMaster software (Version v2x73.2; both HEKA). Using a DMZ universal puller (Zeitz Instruments), patch pipettes were pulled from borosilicate glass (1.5 OD x 1.17 x 100 L mm, Harvard apparatus), heat polished and exhibited a resistance of 2.5 – 5 M Ω when filled with intracellular solution. Whole-cell voltage- and current-clamp recordings were performed at 32°C (23°C when postsynaptic currents were recorded) and brain slices (see 3.8.2) were constantly superfused with carbogenated artificial cerebrospinal fluid (ACSF, extracellular solution).

3.8.2 Acute brain slice preparation

Brain slice preparation was performed as previously described [29, 95, 96], with slight modifications for this study. Male and female mice used for electrophysiology were aged 15-30 days (HCN3 KO and corresponding WT littermates) or 7-12 days (TPC1 KO, TPC2 KO, and corresponding WT littermates). Animals were anaesthetized, decapitated and the head was submerged into ice-cold oxygenated (95% O₂/5% CO₂) slicing solution immediately. The brain was dissected, the cerebellum was removed and the brain was glued onto a slicing platform. For brain slices containing the PreBötC, the brain was glued onto the platform upside-down, i.e. the cerebellum and brainstem remained intact and parts of the prefrontal cortex and forebrain were removed. Coronal slices (225 – 300 μ m) were prepared using a microtome (Microm HM 650 V, Thermo Scientific) and ice-cold carbogenated slicing solution. The sections were transferred to carbogenated storage solution where they were incubated at 37°C for 30 min, and kept under room temperature for at least another hour before use.

3.8.3 Patch clamp protocols

For recordings of I_h , neurons were voltage clamped at -45 mV, and 3 second step pulses were applied in 10 mV increments from -140 mV to -30 mV, followed by a final 250 ms step back to -140 mV (interpulse interval: 14 seconds).

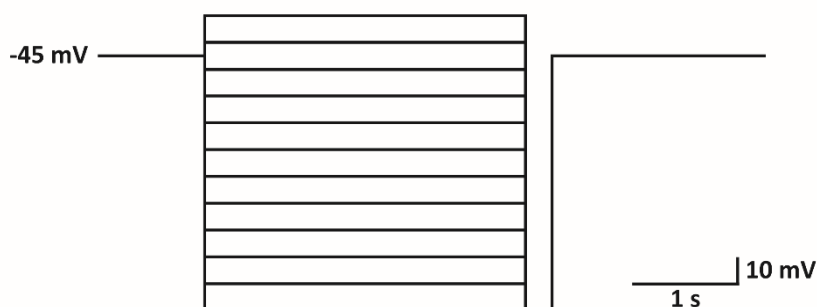


Figure 5 Graphic visualization of the protocol used to measure I_h currents. For details see text.

For the recording of postsynaptic currents, neurons were clamped to a potential of -70 mV and spontaneously occurring currents were measured for 5 min. Due to restrictions of the PatchMaster software, the 5 min recording was sectioned into 30 sweeps lasting 10 seconds each. To monitor changes in access resistance, a -5 mV step (200 ms) was implemented at the beginning of each sweep.

3.8.4 Solutions used in patch clamp experiments

For the experiments in the present study, slightly different intracellular and extracellular solutions were used for distinct ion channels. Furthermore, to isolate the currents of interest, different pharmacological inhibitors were added to the extracellular solution.

High sucrose slicing solution			
NaCl	65 mM		
KCl	2.5 mM		
Na ₂ HPO ₄	1.25 mM		
NaHCO ₃	26 mM		
CaCl ₂	0.5 mM		
MgCl ₂	7 mM		
Sucrose	105 mM		
Glucose	24.7 mM		
Ascorbic acid	1.7 mM		

I_h extracellular solution		I_h intracellular solution	
NaCl	131 mM	KMeSO ₄	140 mM
KCl	2.5 mM	HEPES	10 mM
NaH ₂ PO ₄	1.25 mM	KCl	10 mM
NaHCO ₃	26 mM	Phosphocreatine	10 mM
CaCl ₂	2 mM	MgATP	4 mM
MgCl ₂	1.2 mM	Na ₃ GTP	0.2 mM
Glucose	18 mM	EGTA	0.1 mM
Ascorbic acid	1.7 mM	pH 7.3	
BaCl ₂	1 mM		
TTX	0.001 mM		
pH 7.4			

Postsynaptic currents extracellular solution		Postsynaptic currents intracellular solution	
NaCl	118 mM	KCl	132.5 mM
KCl	3 mM	HEPES	10 mM
NaH ₂ PO ₄	1 mM	CaCl ₂	1 mM
NaHCO ₃	25 mM	MgCl ₂	2 mM
CaCl ₂	1.5 mM	Na ₂ ATP	4 mM
MgCl ₂	1 mM	EGTA	5 mM
Glucose	10 mM	Na ₃ GTP	0.5 mM
pH 7.4		pH 7.3	

For the recording of miniature excitatory or miniature inhibitory postsynaptic currents (mEPSC and mIPSC respectively) tetrodotoxin (TTX) was added to the extracellular solution to a final concentration of 0.5 μ M to block action potentials. Further, mEPSCs were recorded using 1 μ M strychnine to block glycinergic signaling and 10 μ M bicuculline to competitively antagonize GABA_A receptors. On the other hand, the extracellular solution contained 25 μ M of 2R-amino-5-phosphonovaleric acid (AP5) inhibiting NMDA receptors and 10 μ M 6-cyano-7-nitroquinoxaline-2,3-dione (CNQX) blocking AMPA/kainate receptors when recording mIPSCs.

3.8.5 Analysis of electrophysiological data

All analysis was performed offline using PatchMaster, OriginPro8 (OriginLab Corporation) and Clampfit10.5 (Molecular Devices). In I_h -measurements, the current amplitude was determined at -130 mV and the current density was calculated as the current amplitude divided by the cell capacitance. To obtain voltage-dependent steady-state activation curves, tail currents measured immediately after the final step to -140 mV were normalized by the maximal current and plotted as a function of the membrane potential. The curves were fitted to the Boltzmann function, with $I/I_{\max} = (1 + \exp[(V - V_{0.5}/k])^{-1}$, with $V_{0.5}$ being the voltage for half-maximal activation and k the slope factor. Bi-exponential time constants were analyzed by fitting the I_h transient at -120 mV using the Chebychev fitting routine, while ignoring the initial lag at the onset of activation. For qualitative analysis of the currents, only the cells were considered that remained stable throughout the experiment.

Inhibitory and excitatory postsynaptic currents were analyzed semi-automatically using the built-in peak detection function of Clampfit. The threshold for peak detection was set to a value of two standard deviations in regards of the noise level averaged over the whole recording. All postsynaptic currents identified by the software were verified to be postsynaptic currents manually. The software then determined the parameters of the selected currents (e.g. 10% - 90% rise and decay time) automatically. For statistical analysis, current parameters were averaged for each cell. Only cells where the access resistance was stable throughout the whole experiment (i.e. changes in access resistance < 20%) were selected for analysis.

3.9 Preparation of the intact septo-hippocampal formation

To establish the novel preparation technique of the complete septo-hippocampal formation [97, 98], male mice of different ages (P1 – 12 weeks) were anaesthetized with isoflurane (Baxter) if

appropriate and decapitated. The brains were carefully removed and submerged in ice cold extracellular solution (see 3.8.4). The plastic spatulas used for the preparation were crafted from 1 ml syringe plungers (Terumo Syringe) that were carved to be tapered at one end. A detailed description of the preparation procedure is given in the results section. The preparation technique was acquired during a visit of Prof. Christophe Bernard's laboratory at the Aix-Marseille University and refined for the current thesis.

3.10 Stereotaxic surgery

To knock out HCN2 channels specifically in the IGL, 8 – 12 weeks old male HCN2 L2 mice were injected with control (n = 15) or Cre-containing (n = 16) viral particles. Before starting the surgery, all tools used as well as the surfaces were cleaned with 70% ethanol thoroughly. The animals were anesthetized with an intraperitoneal injection of 10 mg/kg Xylazin (Ecuphar) and 100 mg/kg Ketamin (Medistar) in 0.9% NaCl. Eye ointment was applied (Bepanthen, Bayer), the fur was removed from the skull, and the surgical area was disinfected before fixing the animals' heads in the stereotaxic apparatus (Small animal stereotaxic instrument model 902, TSE). For better vision of the surgical area, a dissecting microscope (OPMI 1 FR pro, Zeiss) or magnifying glasses were utilized. Using small surgical scissors, the scalp was cut open along the midline and the subcutaneous tissue was removed. The skull was cleaned with a cotton bud soaked with 3% H₂O₂ to visualize bregma and lambda clearly. Thereafter, the skull and the surrounding skin were cleaned thoroughly with sterile, isotonic 0.9% NaCl solution to remove all remaining hydrogen peroxide and the tissue was kept moist throughout the surgery. Using bregma as reference, the coordinates for the bilateral injection of AAVs were calculated (AP: 2.3 mm; ML: ±2.55 mm). Using a dentist's drill (K-control 4970 with K5 plus-tool holder, KaVo) one hole (< 1mm) at a time was drilled into the skull at the appropriate coordinates. The micro syringe (Nanofil, WPI) loaded with either control (rAAV2/1-hSyn-eGFP; Titer: 2.96×10^{10} vector genomes/ μ l) or Cre-containing (rAAV2/1-hSyn-Cre-t2A-eGFP; Titer: 3.12×10^{10} vector genomes/ μ l) virus and the injection needle (NF33BL, WPI) were brought to the injection site carefully. The needle was lowered to the dura and the depth of the injection was calculated (DV: 3.4 mm). Then the needle was inserted into the brain slowly and after reaching the correct position the injector (UMPIII with Micro4 controlling element, WPI) was started to deliver 150 nl virus at a flow-rate of 1 nl/s. To avoid backflow the needle was kept in place for 3 min after the injection was finished and then withdrawn carefully. The animal was removed from the stereotaxic frame and the scalp wound was sutured. PVP-iodine was applied to the wound for disinfection and the animal received an intraperitoneal injection of analgesic (Carprofen, Norbrook). Mice were allowed to recover for

3 weeks before being sent to the Albrecht lab in Fribourg, Switzerland. For analysis, only mice were included that showed transduction of IGL neurons at least unilaterally.

3.11 Behavioral experiments

All behavioral experiments were performed on HCN3 KO and corresponding wild type littermates or on HCN2 L2 animals in accordance with legal regulations. The testing of the circadian behavior was done in collaboration with the group of Prof. Urs Albrecht at the University of Fribourg, Switzerland.

3.11.1 Circadian testing

The tests for circadian behavior were carried out on male HCN3 KO (n = 10) and corresponding wild type littermates (n = 8) and on HCN2 L2 animals being injected with either pAAV2.1-hSyn-Cre-2A-eGFP (n = 16) or pAAV2.1-hSyn-eGFP (n = 15) according to [99]. Upon arrival in Fribourg, the animals were placed in new cages containing the running wheel and entrained for 7 – 15 days to 12 hour light / 12 hour dark conditions (LD), with lights switched on at 7 am. Then they were released into constant light (LL) or constant dark (DD) conditions and the activity was assessed via the provided running-wheel and evaluated using ClockLab (Actimetrics). The period length was assessed by χ^2 periodogram analysis between days 4 – 10 under DD or LL conditions. Light induced phase shifts were determined using an Aschoff type I protocol [100] after animals had been allowed to stabilize their free-running rhythm for at least 14 days. Within this protocol, animals that display a stable free-running rhythm in constant darkness are subject to a light pulse at different circadian time (CT) points. For each animal, the CT at the beginning of the light pulse was calculated individually. Light pulses (400 lux, white light) of 15 min duration were applied CT 10 (control), CT 14 and CT 22. The timing of the light pulses induces different behavior. A light pulse at CT 10, which corresponds to light perceived during the subjective day should not produce significant phase shifts, whereas light pulses delivered at CT 14 or CT 22 correspond to early or late subjective night should lead to phase delays or advances, respectively. After exposure to one light pulse, mice were allowed to stabilize their rhythms again for at least two weeks before a different light pulse was applied. The induced phase shifts were identified by fitting regression lines through onsets of activity before and after the light pulse and the distance between the two lines on the day after the light pulse determined the amount of phase shifting. HCN3 KO and wild type littermates were further tested in a jet-lag experiment, where, after being kept in a 12 hour light / 12 hour dark cycle for at least 10 days,

mice were exposed to a 6h delay (forwards or backwards) of the LD cycle and the time needed to adapt to the new cycle was measured. In a final experiment, animals were entrained to a 12:12 h LD rhythm for 10 days and then exposed to a 6:6:6:6 h LDLD schedule for two weeks. The number of animals adapting to the new lighting schedule was determined.

3.11.2 Fear conditioning

The fear conditioning paradigm was carried out on male wild type (n = 10) and HCN3 KO (n = 10) animals aged between 6 and 9 weeks according to a protocol by Kamprath and Wotjak [101]. The fear conditioning experiments were performed in two different contexts: a cubic shaped shock chamber (TSE) with a metal grid for shock application (conditioning context), and a cylindrically shaped acrylic glass box with wood shavings as bedding (neutral context). For conditioning (day 0), mice were placed into the shock chamber and after 180 s a tone was presented (9 kHz, 80 dB, 30s). During the final 2 s a foot shock was applied simultaneously (0.7 mA). Animals stayed in the shock context for another 30 s before being returned to their home cages. The day after, mice were exposed to the tone (180 s) in the neutral context and on the second day after conditioning the exposure to the tone took place in the conditioning context (shock chamber). One week later the exposures to the tone in the different contexts were repeated. Behavior was videotaped (Eneo VK-1316s, TSE) and analyzed off-line. Freezing behavior (immobility) served as a measure of fear memory. Martha Schöll-Weidinger carried out experiments manually. Analysis and interpretation of data were performed by myself in collaboration with Dr. Carsten Wotjak from the MPI for psychiatry.

3.12 Statistics

Statistical significance was tested with GraphPad Prism 5. The tests executed were either χ^2 , unpaired t-test, or analysis of variance (ANOVA) for repeated measures. A *post-hoc* test (Bonferroni) for multiple comparisons was applied if appropriate. Statistical significance was accepted if $P \leq 0.05$. All values were calculated and are presented as mean \pm standard error of the mean (SEM) unless indicated otherwise.

4 Results

In the present thesis, the role of second messenger-activated cation channels in the central nervous system (CNS), their expression, function and influence on rodent behavior was examined. In detail, the expression of HCN3 channels in the murine CNS as well as their implication in fear learning and circadian timing was tested. Moreover, new tools, that will help to increase the understanding of the functioning of the channels, were developed and established. Finally, the current work shall give insights into the expression of TPCs in the murine brain and whether knockout of either TPC isoform has influence on basic synaptic functioning.

4.1 HCN channels in the mouse CNS

In a first step, I focused on HCN3 in the CNS and its possible impact on mouse behavior. Using immunohistochemical experiments, HCN3 channels were found to be broadly expressed in neurons of the mouse nervous system (see Table 1, also see [34]), including hypothalamic and thalamic structures, nuclei of the brain stem, limbic areas, retina, and others.

Name of the structure	Expression	Name of the structure	Expression
<i>Hypothalamus</i>		<i>Brainstem</i>	
Hypophysis	++	Locus coeruleus	++
Nucleus dorsomedialis	++	Nucleus parabrachialis lateralis	++
Nucleus hypothalamicus anterior	++	Nucleus parabrachialis medialis	++
Nucleus lateralis	++	Nucleus subparabrachialis	++
Nucleus paraventricularis	++	Nucleus tegmentalis, laterodorsal	++
Nucleus preopticus medialis	++	Periaqueductal grey	++
Nucleus supraopticus	++	Raphe nuclei dorsal part	++
Suprachiasmatic nucleus	-	Raphe nuclei medial part	++
<i>Thalamus</i>		Substantia nigra pars compacta	
Corpus geniculatum mediale	-	<i>Limbic system</i>	
Intergeniculate leaflet	++	Basolateral Amygdala	++
Lateral geniculate nucleus dorsal part	-	Hippocampus, str. Lacunosum mol.	+
Lateral geniculate nucleus ventral part	++	<i>Main olfactory bulb</i>	
Nucleus habenularis lateralis	++	Glomerular layer	++
Nucleus habenularis medialis	++	Internal plexiform layer	++
Nucleus laterodorsalis	++	<i>Telencephalon</i>	
Nucleus paraventricularis Thalamicus	++	Cortex	+
Nucleus reticularis	++	Nucleus basalis	++
<i>Retina</i>		<i>Cerebellum</i>	
Inner plexiform layer	++		+
Outer plexiform layer	+		

Table 1 Overview of HCN3 channel expression in the mouse nervous system. Immunohistochemical experiments revealed that HCN3 channels are expressed in numerous areas of the nervous system. Table adapted from Stieglitz et al. [102] It was created by the combination of data collected by Martha Schöll-Weidinger [34] and by myself.

As evident from IHC experiments, HCN3 channels are expressed in a multitude of nuclei implicated in the regulation of murine behavior, including areas of the limbic system, such as the basolateral amygdala and the hippocampus. These brain regions are implicated in the formation of associative memory, as well as the development, learning and expression of fear. To test whether HCN3 channels are associated with the regulation of fear, HCN3 KO animals (n = 10) and WT littermates (n = 10) were exposed to the fear conditioning paradigm (Figure 6). On the day of conditioning (day 0) mice were placed into a shock chamber. After 3 min of habituation (pre-training) a tone was presented for 30 s and co-terminated with an electric foot shock (Figure 6, first panel). The next day, animals were placed into a novel, cubic shaped chamber (neutral context, NC) and were observed for 3 mins (Figure 6, second panel). Thereafter, a tone, but no shock was applied and the mice were observed for another 3 minutes (Figure 6, third panel). On the second day after conditioning, the animals were re-exposed to the shock chamber (Conditioning context, CC), but this time neither a shock nor a tone were presented (Figure 6, fourth panel). One week later, the exposures to the neutral and the

conditioning context were repeated (i.e. on day 7 and 8 after conditioning). Freezing behavior (immobility) served as a measure of fear.

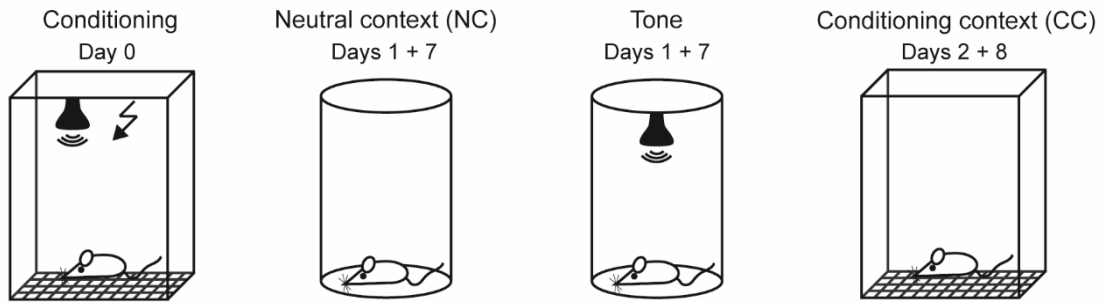


Figure 6 Fear conditioning paradigm. Schematic of the fear conditioning test. WT and HCN3 KO animals were exposed to the shock chamber and a tone that co-terminated with a foot shock (first panel). On day one and seven after conditioning, the behavior in the NC was observed before and during presentation of a tone (second and third panel). One week later, the animals were exposed to the CC without application of a shock or tone (fourth panel).

During pre-training, before application of the tone and the foot shock, both groups of animals were active and exhibited low and statistically indistinguishable levels of freezing (GT: $F_{1,18} = 0.7615$, $p > 0.05$; GT x Time: $F_{2,36} = 1.034$, $p > 0.05$; 2-way ANOVA for repeated measures; data not shown). Upon exposure to the NC the next day, HCN3 KO and WT mice showed similar low levels of immobility before tone presentation (Genotype (GT): $F_{1,18} = 0.2399$; $p > 0.05$; GT x Time: $F_{2,36} = 0.0592$, $p > 0.05$; Figure 7A). However, when re-exposed to the NC on day 7, the freezing behavior of HCN3 KO animals was significantly increased compared to WT mice (GT: $F_{1,18} = 5.427$; $p < 0.05$; Figure 7A). Upon presentation of the tone in the NC on day 1 as well as on day 7, the animals' freezing behavior was found to be increased irrespective of the genotype (GT: $F_{1,18} \leq 0.047$, $p \geq 0.830$; Figure 7B). Furthermore, exposure to the CC did not result in differences in freezing behavior between the two genotypes, both at day 2 (GT: $F_{1,17} = 2.692$; $p > 0.05$) and day 8 (GT: $F_{1,17} = 3.792$; $p > 0.05$) (Figure 7C). Analysis of the specificity of contextual fear, expressed as the difference in immobility in the CC and the NC, also revealed no statistically significant differences between the two genotypes ($t_{17} = 1.415$, $p > 0.05$; unpaired t-test; Figure 7D). When short- and long-term (day 1 to day 7 and day 2 to day 8) changes in freezing were analyzed in more detail, HCN3 KO animals displayed a lack of fear adaptation over the course of tone presentation at day 7 ($F_{2,36} = 4.051$, $p = 0.025$; evident from Figure 7B), but not at day 1 ($F_{2,36} = 0.506$, $p = 0.606$). Furthermore, genotype differences were found in case of freezing in the NC (GT x Day: $F_{1,17} = 8.856$, $p < 0.01$) and the CC (GT x Day: $F_{1,17} = 7.989$; $p < 0.05$), but not in immobility upon presentation of the tone (GT x Day: $F_{1,18} = 0.1909$; $p > 0.05$) (Figure 7E). Moreover, the long-term extinction at the level of the individual animal (separately per genotype) was analyzed. HCN3 KO animals displayed a significant increase in freezing in the NC

($t_9 = 3.564$, $p < 0.01$; paired t-test) which was absent in WT animals ($t_9 = 0.938$, $p > 0.05$) (Figure 7F). Also, freezing to the tone tended to be decreased in WT animals ($t_9 = 2.220$, $p > 0.05$) and was significantly decreased in HCN3 KO mice ($t_9 = 2.462$, $p < 0.05$; paired t-test) (Figure 7G). Contrarily, WT ($t_9 = 3.205$, $p = 0.01$) but not KO animals ($t_8 = 0.329$, $p > 0.05$; Figure 7H) displayed a statistically significant decrease in contextual fear from day 2 to day 8.

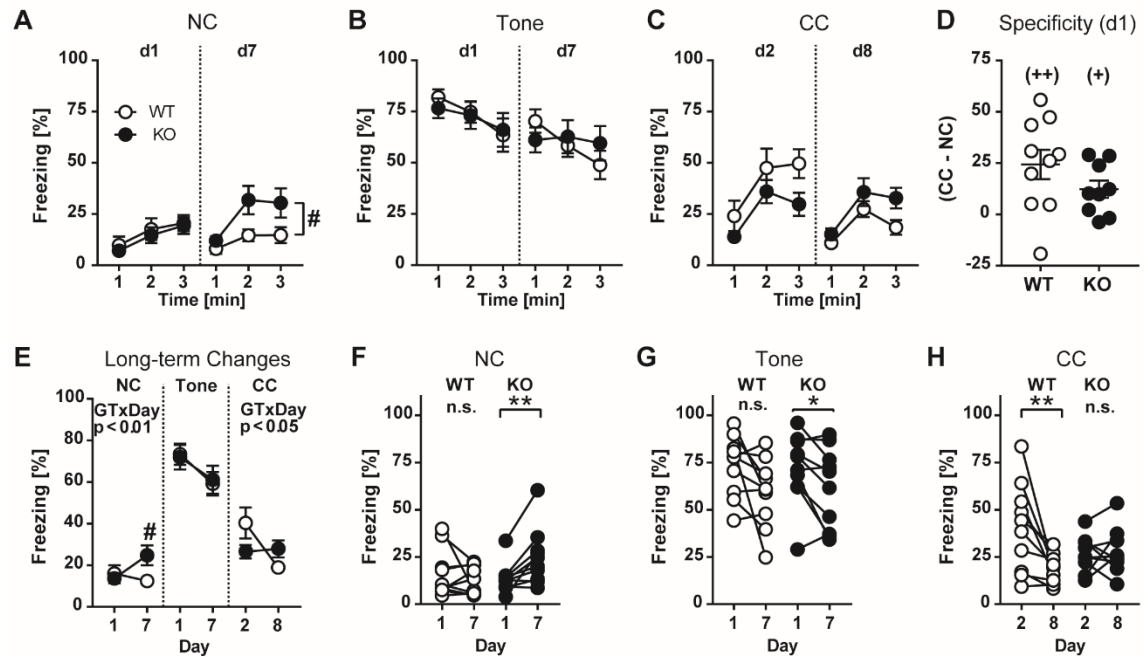


Figure 7 Analysis of the fear conditioning experiment. **(A)** Freezing in the NC before tone presentation (expressed in 1-min intervals) at d1 and d7. **(B)** Freezing to the tone at d1 and d7 (1-min intervals). **(C)** Freezing in the CC at d1 and d7 (1-min intervals). **(D)** Specificity of contextual fear expressed as the difference between freezing in the CC and the NC. **(E)** Long-term changes in freezing (NC, tone and CC) from d1 to d7. **(F-H)** Individual data plots showing long-term changes in freezing from d1 to d7 separately per genotype. * $p < 0.05$, ** $p < 0.01$ (paired t-test), + $p < 0.05$, ++ $p < 0.01$ (one-sample t-test against theoretical value 0), # $p < 0.05$ (KO vs. WT; 2-way ANOVA followed by Bonferroni post-hoc test, if appropriate). [Note: One KO was excluded from further analysis of contextual fear since it was identified as outlier [<http://www.graphpad.com/quickcalcs/grubbs1/>]. Analysis of data was performed in collaboration with Dr. Carsten Wotjak.

Taken together, HCN3 KO mice appear to have deficits in long-term processing of contextual fear as well as acute fear adaption upon re-exposure to the tone. This can be interpreted as lack of fear extinction and increase in context generalization.

Another brain region that exhibited a very prominent HCN3 expression was the IGL, a nucleus important in modulating circadian rhythms [32]. These rhythms are primarily orchestrated by a hypothalamic area named suprachiasmatic nucleus (SCN), which is modulated by inputs arriving from the IGL (Figure 3). In the SCN itself, no HCN3 channels are expressed. The IGL has been suggested to be of importance for the transmission of photic as well as non-photoc cues via the geniculohypothalamic tract to the SCN [32], thereby influencing the central circadian

pacemaker. Since HCN3 shows the highest expression of all HCN channel family members in the IGL, we were interested in testing the hypothesis that the knockout of these channels influences circadian behavior of mice.

Mice were housed in cages where they had access to a running wheel (Figure 8). Therefore, the measurement of wheel revolutions served as an indicator for general locomotive behavior and daily activity did not differ between WT (24091 ± 1960 revolutions) and HCN3 KO animals (20439 ± 2357 revolutions) under 12:12 h LD conditions. When being released into LL conditions, the animals' average activity was also similar between WT and HCN3 KO animals exhibiting 7200 ± 1241 and 8118 ± 1613 wheel revolutions/day, respectively. Interestingly, when the mice were exposed to constant darkness, the animals lacking the HCN3 channel showed significantly reduced activity compared to their WT littermates (HCN3 KO: 17925 ± 1945 ; WT: 23482 ± 1555 ; $p < 0.05$, unpaired two-tailed t-test; Figure 8C). This indicates that HCN3 channels might be implicated in modulation of locomotor activity in the absence of light while being of less importance in the presence of a light cue.

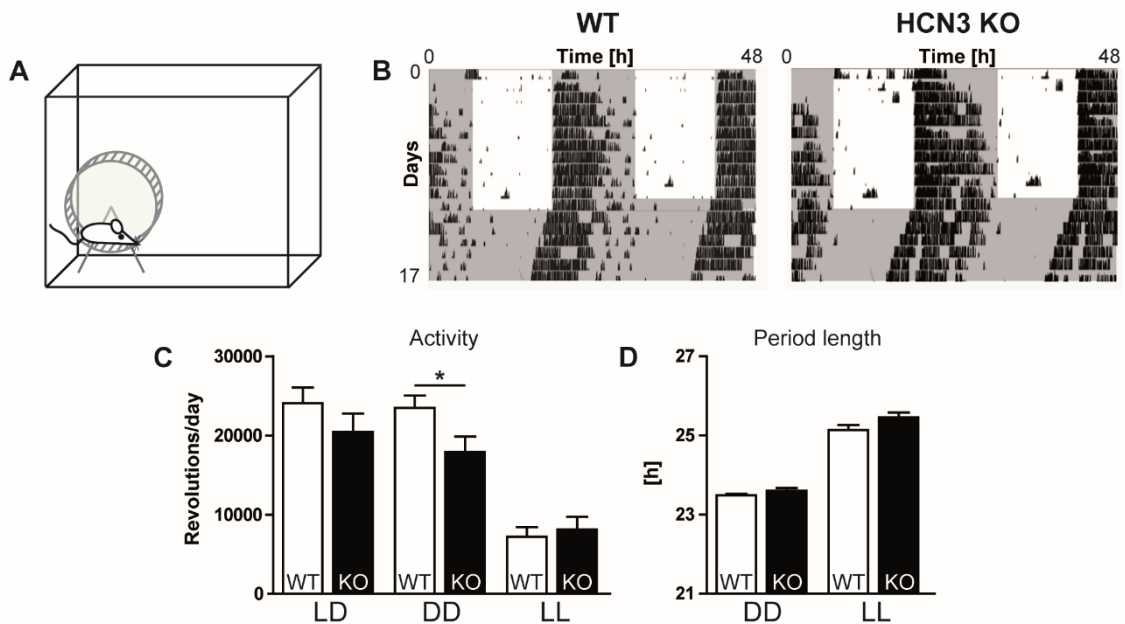


Figure 8 Circadian testing – activity and period length. **(A)** Schematic of the home cage containing the running wheel. **(B)** Wheel-running activity of WT (left) and HCN3 KO (right) animals. White areas indicate light, whereas grey areas indicate darkness. Black bars reflect wheel revolutions. The actograms are double-plotted and show two days per line. **(C)** Quantification of activity counts, represented as wheel revolutions per day, under light dark (LD), constant dark (DD) and constant light (LL) conditions. **(D)** Period lengths under DD or LL conditions. All values are mean \pm SEM. *: $p < 0.05$; unpaired two-tailed t-test. All circadian experiments were done in collaboration with Prof. Dr. Urs Albrecht at Fribourg, Switzerland.

Constant light or constant darkness conditions, LL or DD, were utilized to examine the influence of HCN3 channels on the so-called “free-running” period of the central circadian clock. The

internal clock residing in the SCN usually is entrained to the outside world via information about light conditions being forwarded from the retina to the SCN via the retinohypothalamic tract (Figure 3). Light is considered the major “Zeitgeber” to reset the clock [103] and adjust it to recurring lighting differences: day and night. Under DD conditions, this Zeitgeber is missing and the central clock is allowed to pursue its own internal rhythm; it is free-running. Similarly, when held under LL conditions, the major Zeitgeber light is constantly present, therefore also influencing the running period of the central circadian pacemaker. Since the IGL also forwards photic information to the SCN, the running period of the internal clock, reflected by the length of active and inactive phases, was assessed. When being exposed to DD, the period lengths of WT and HCN3 KO animals were statistically indistinguishable and slightly shorter than the typical 24 h periods under LD conditions (23.49 ± 0.03 h and 23.6 ± 0.07 h). In LL conditions the period lengths determined were 25.14 ± 0.12 h for WT and 23.6 ± 0.07 h for HCN3 KO mice ($p > 0.05$; Figure 8D). Together these findings suggest that the pace of the central circadian clock is not influenced by knockout of HCN3.

In a next step, the mice were tested regarding their clock-resetting behavior when exposed to a light stimulus in DD conditions. Animals were adapted to DD conditions for at least 14 days before being exposed once to a 15 min light pulse during darkness. Thereafter, mice were kept under DD conditions for additional 16 days and the phase shift induced by the nocturnal light pulse was assessed. In a first experiment, WT and HCN3 KO animals were exposed to the light pulse during the early subjective night (CT14). Irrespective of the genotype, both groups of animals responded to the light challenge at CT14 with similar delays in their phases (WT: -93.29 ± 12.88 min and HCN3 KO -107.8 ± 14.24 min) (Figure 9A left). Mice were re-entrained to the DD conditions and subsequently were subjected to a 15 min light pulse at CT22, corresponding to the late subjective night. In this case, both groups exhibited similar phase advances of 39 ± 7.01 min (WT) and 28.44 ± 4.45 min (HCN3 KO) (Figure 9A right), again indicating that HCN3 channels appear to be of less importance for basic circadian behavior.

Thereafter, mice were re-entrained to a 12 h LD period for at least 10 days before the jet-lag experiments were conducted to identify whether HCN3 channels have influence on the circadian behavior when animals are exposed to an abrupt change of photoperiod length. In two experiments, the LD cycle was either delayed or advanced by 6 hours. The completion of adaptation to the delay took WT animals 1.63 ± 0.26 days and HCN3 KO mice needed 1.1 ± 0.1 days ($p > 0.05$) (Figure 9B, backward). When advancing the cycle, both groups took less than 4 days to adapt their clock to the new schedule (WT: 3.88 ± 0.44 d; KO: 4.1 ± 0.67 d) (Figure 9B, forward). Therefore, the deletion of HCN3 channels does not significantly alter the capability to adapt to a new lighting schedule.

In a final set of circadian experiments, WT and HCN3 KO animals were tested regarding their masking behavior since it has been shown that nuclei of the subcortical visual shell (a group of nuclei in the diencephalon receiving direct retinal input), including the IGL, might be implicated in this behavior [32]. Masking is defined as any locomotor behavior that is not driven by the central clock and therefore hinders the deciphering of the internal rhythm [104]. Hence, in mice, darkness increases activity and therefore positively masks, whereas light negatively masks by suppressing locomotor activity. To test this, mice were trained to a 12 h LD rhythm and then released into a 6:6:6:6 LDLD lighting schedule. Expectedly, only few WT animals (2 of 8) could not pursue their 24 h free-running activity under these conditions, however, in HCN3 KO animals the number was equally low (3 of 10; data not shown). Taken together, the circadian experiments performed suggest that the HCN3 channel appears to be dispensable for normal circadian behavior, but might influence locomotor activity in absence of light.

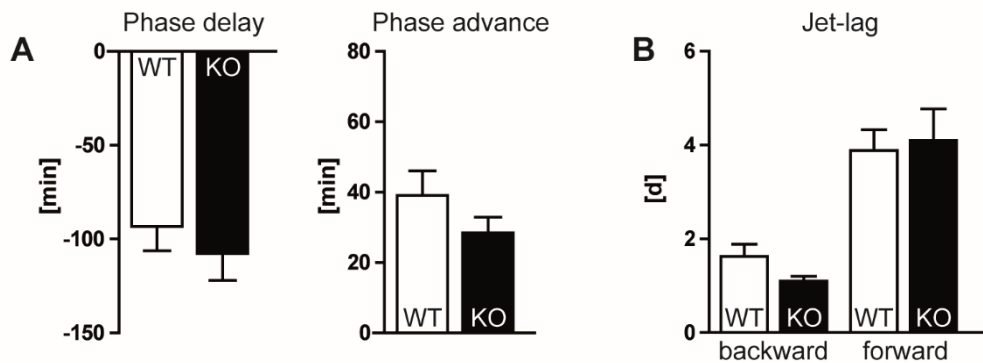


Figure 9 Circadian testing – Phase shift and jet-lag. **(A)** Quantification of clock resetting in response to a 15 minute light pulse applied at CT14 (phase delay, left) or at CT22 (phase advance, right). **(B)** Quantification of time needed to adapt to the delay of light onset by 6 hours (backward shift, left) or to advancing the light onset by 6 hours (forward shift, right). Data are presented as mean ± SEM.

Since the knockout of HCN3 failed to result in a distinct circadian phenotype and Ying et al. [29] showed a clear influence of HCN3 channels on rhythmic IGL burst firing, the hypothesis that other HCN channel isoforms (mainly HCN2), might contribute to the I_h in IGL neurons, was tested. Therefore, whole-cell voltage clamp measurements in IGL neurons of acute brain slices from WT and HCN3 KO animals were undertaken. IGL neurons were clamped to a holding potential of -45 mV and step pulses were applied in 10 mV increments from -140 mV to -30 mV, followed by a final 250 ms step back to -140 mV. In IGL neurons of WT animals, a prominent I_h current (Figure 10) could be measured in 28 of 108 cells. Interestingly, I_h currents were also detected in HCN3 KO IGL neurons, although the number of cells exhibiting such currents (18 of 151) was significantly reduced ($\chi^2 = 8.456$; $p < 0.01$) (Figure 10B).

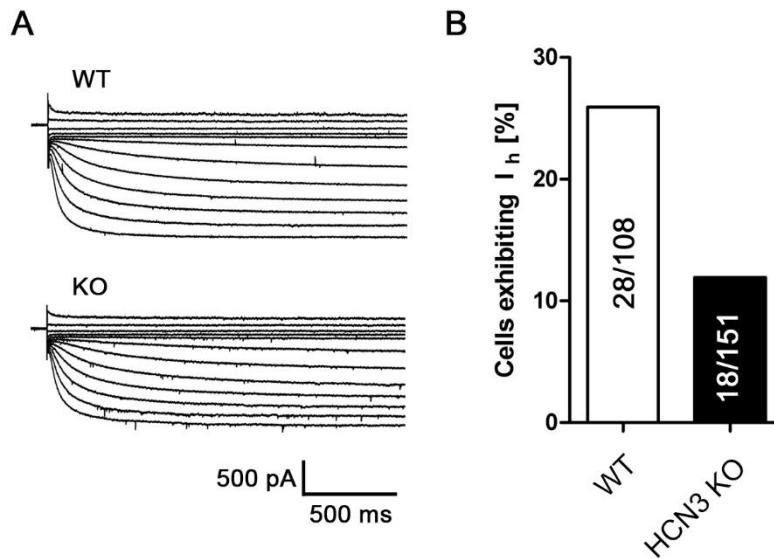


Figure 10 I_h in IGL neurons. **(A)** Representative current traces of I_h in WT and HCN3 KO neurons of the intergeniculate leaflet. For simplicity, capacitive transients and the tail currents are not shown. **(B)** Quantification of IGL neurons exhibiting I_h . In total, 28 of 108 WT neurons and 18 of 151 HCN3 KO neurons displayed a prominent I_h ($p < 0.01$; χ^2 -test)

The current densities, calculated as the absolute value of the current amplitude divided by the cell's capacitance, were 13.28 ± 2.94 $-pA/pF$ in WT and 11.52 ± 2.46 $-pA/pF$ in KO cells and statistically indistinguishable ($p > 0.05$) (Figure 11A). It furthermore appeared that the currents of WT IGL neurons and HCN3 KO neurons did not differ in their kinetics, since both time constants, τ_1 and τ_2 , were similar (Figure 11B) (τ_1 : 615.2 ± 75.89 ms and 780.9 ± 121.9 ms; τ_2 : 104.4 ± 8.62 ms and 123.8 ± 18.93 ms).

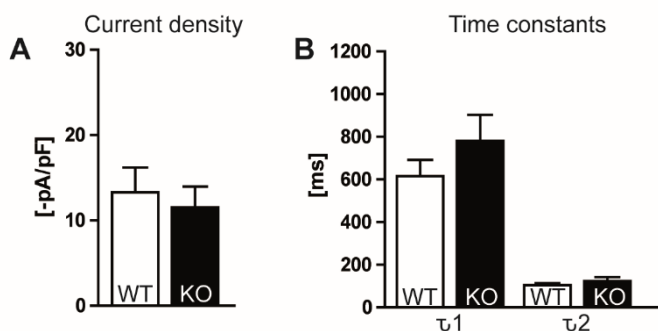


Figure 11 Current density and kinetics of I_h . **(A)** Current densities of WT and HCN3 KO neurons did not differ ($p > 0.05$; unpaired two-tailed t-test). **(B)** The time constants τ_1 and τ_2 , determined from double-exponential fitting routines, were similar in both groups ($p > 0.05$; unpaired two-tailed t-test). Data are presented as mean \pm SEM.

In a next step, the tail currents (Figure 12) were analyzed to determine the steady-state activation curve, the half-maximal activation ($V_{0.5}$) and the slope factor k . To this end, the

amplitudes of the tail currents were normalized and fitted using the Boltzmann equation. The steady-state activation curves of both groups were similar and almost superimposable (Figure 12B). The half-maximal activation values were determined to be -90.70 ± 0.70 mV in WT cells and -91.99 ± 1.79 in HCN3 KO cells ($p > 0.05$)(Figure 12C). Also, the slope of the activation curves was similar for both genotypes (WT: 6.96 ± 0.32 and KO: 7.30 ± 0.57 ; $p > 0.05$) (Figure 12C).

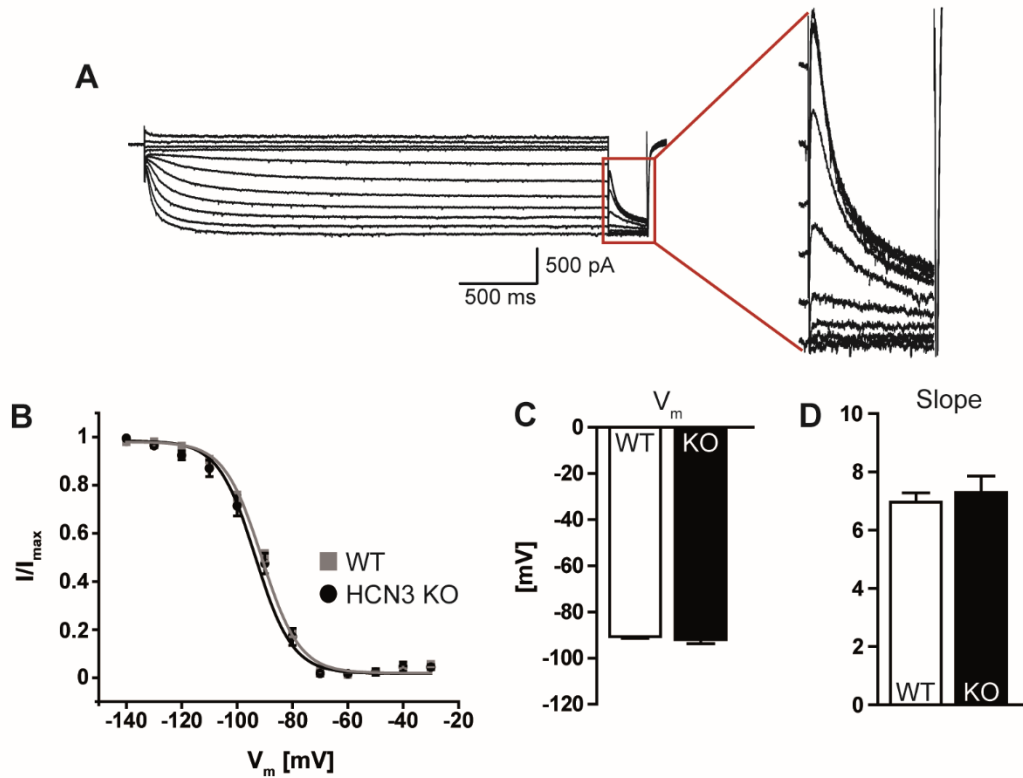


Figure 12 Analysis of the tail currents. **(A)** Representative current trace of a WT cell. Magnification shows the tail currents in more detail. **(B)** Steady-state activation curve of I_h from WT (grey rectangles) and HCN3 KO (black circles) cells. **(C)** Half-maximal activation value and **(D)** slope factor k were similar in both genotypes ($p > 0.05$; unpaired two-tailed t-test). Data are presented as mean \pm SEM.

Taken together, the results from the voltage-clamp experiments in IGL neurons show that the number of cells displaying a prominent I_h is reduced in HCN3 KO animals, however, in almost 12% of cells measured a clear hyperpolarization-activated current is still detectable. Most likely this is due to the expression of HCN2 channels in the IGL. Interestingly, all parameters analyzed, such as current density, kinetics, and half-maximal activation did not differ between the two genotypes.

Hence, HCN2 channels appear to be expressed and functional in the IGL and the hypothesis that these channels might in turn be influencing the mouse circadian behavior was tested. Since global HCN2 KO animals display several neurological and bodily disturbances [48], they could not be tested for their circadian behavior based on wheel running activity. Therefore, HCN2 L2

animals, possessing two LoxP-sites in their genome flanking exons 2 and 3 of the HCN2 gene, were used.

To produce animals that lack a functional HCN2 channel in the IGL specifically, viral particles (see 3.5) driving the expression of a Cre-recombinase were injected into the IGL of HCN2 L2 animals. The recombinase recognizes the two LoxP-sites and excises the part of the genome located between them, resulting in a premature stop codon upon translation and therefore a functional knockout of HCN2 channels in the transduced neurons. For stereotaxic injections and subsequent circadian testing male, littermate-matched HCN2 L2 animals were randomly assigned into two groups. One group (n = 15) received injections with control particles (pAAV2/1-hSyn-eGFP) (Figure 13A) and the other group (n = 16) was injected with viral particles containing the Cre-recombinase (pAAV2/1-hSyn-Cre-t2A-eGFP) (Figure 13B). Immunohistochemical analysis revealed that in 6 of 15 control particle injected animals, at least one IGL was markedly transduced, whereas in the Cre-injected animals 9 mice showed clear transduction of IGL neurons at least on one side. IHC experiments also proved that induction of Cre in IGL neurons leads to a drastic decrease of HCN2 expression (Figure 13B right panel), whereas HCN2 was still present in neurons transduced with control particles (Figure 13A right panel). Furthermore, multiple neurons ventrally of the IGL (in the vLGN) were transduced (Figure 13). However, to date there is no evidence for vLGN neurons contributing to any form of circadian regulation.

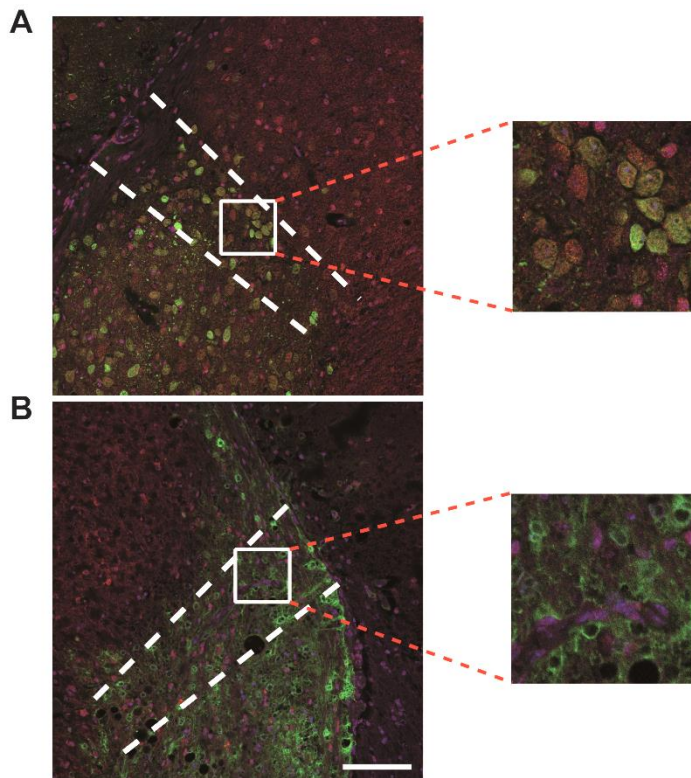


Figure 13 Examples of transduced IGL neurons. **(A)** Brain slice of HCN2 L2 animal injected with control particles. Right panel shows magnification of the enboxed area. **(B)** Brain slice of HCN2 L2 animal injected with Cre-recombinase containing particles. Right panel shows magnification of the enboxed area. White dashed lines indicate the approximate location of the IGL. Blue = DAPI, green = GFP, red = HCN2. Scale bar = 100 μm .

Compared to the work performed in HCN3 KO mice, less experiments were carried out to assess only the most important parameters as activity in LD and DD, period length in DD and phase delay towards a light pulse presented at CT14. When housed under 12:12 h LD conditions, the daily activity between control injected (GFP: 22450 ± 1285) or Cre-injected (Cre: 25120 ± 2130) animals did not differ (Figure 14A left). The same was true for activity in constant darkness, where control animals exhibited 20980 ± 1607 and Cre-injected animals 24780 ± 1302 wheel revolutions per day (Figure 14A right). The free-running periods, assessed under DD conditions, did also not differ significantly. Animals injected with control particles displayed a free-running period of 22.99 ± 0.18 h and animals treated with Cre particles exhibited a free-running period of 23.38 ± 0.06 h (Figure 14B). Lastly, when mice were exposed to a 15 min light pulse during the early subjective night (CT14), the animals reacted with the expected phase delay, which was similar in both groups (GFP: -152.00 ± 21.90 min; Cre: -121.10 ± 15.31 min) (Figure 14C).

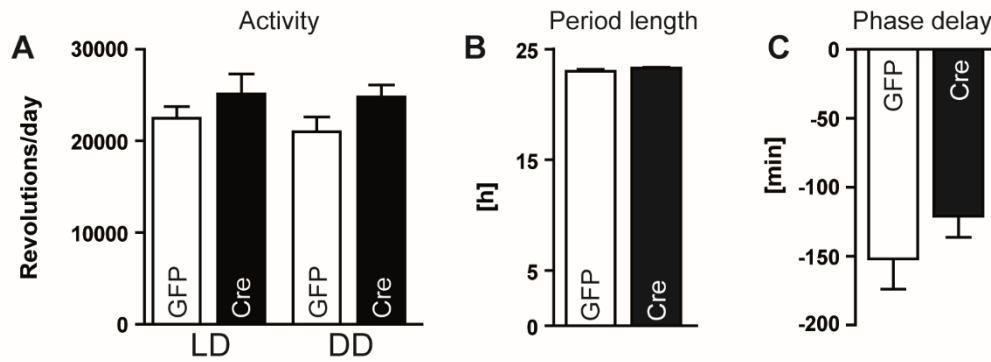


Figure 14 Circadian behavior of injected HCN2 L2 animals. **(A)** Quantification of activity counts, represented as wheel revolutions per day, under LD and DD conditions. **(B)** Period length under DD conditions. **(C)** Quantification of clock resetting in response to a 15 minute light pulse applied at CT14. Data are presented as mean \pm SEM.

4.2 Establishment of new tools to study theta rhythm generation

HCN2 channels are widely expressed in the rodent brain. Apart from the IGL they can for example be found in the olfactory bulb, cerebral cortex, brain stem, thalamic areas, forebrain and others. Of particular interest for the present thesis was the medial septum/diagonal band of Broca, where HCN2 channels are expressed to a high degree [23, 105, 106]. The MS/DBB is a region critically involved in the formation of the theta rhythm, a prominent neural oscillation in the 4-12 Hz frequency band that can be measured in many parts of the brain, especially in the septo-hippocampal system. Previous experiments from this group suggest HCN2 channels of the MS/DBB to play an exceptional role in the generation and maintenance of theta oscillations. When HCN2 channels have been knocked out in all classes of neurons in the MS/DBB using a viral approach, a drastic reduce in theta power during wakefulness and REM sleep has been observed, which also had influence on murine behavior such as hippocampus-dependent learning in the water cross maze [51]. However, the mechanism underlying this effect remains elusive and the focus had not been laid on identifying the contribution of different neuronal classes on theta rhythm generation. Therefore, another goal of the current thesis was the development and establishment of new tools and preparations to manipulate and analyze theta rhythm generation.

Since HCN2 channels are expressed in different subpopulations of medial septal neurons, i.e. GABAergic and glutamatergic neurons (cholinergic neurons only to a lesser extent), one goal will be to clarify whether HCN2 channels in these neurons contribute to theta rhythm generation to the same extent and whether the knockout of HCN2 in all MS/DBB neurons or different subpopulations produces similar cellular, physiological and behavioral alterations. To answer this, HCN2 channels will be deleted from all neurons or the different neuronal populations

specifically using a Cre-LoxP approach by delivering Cre-recombinase to HCN2 L2 animals using viral particles. Targeting gene expression to specific neuronal subpopulations requires the usage of relatively large promoter sequences. Since lentiviral particles have a larger packaging capacity (~8 kb) compared to AAV particles (~5 kb) they are more suitable to include large promoters and were therefore produced in the current thesis. In a first step, the plasmids containing the promoters and the genes of interest were cloned based on an already existing plasmid: LV-Syn1.1-eGFP. In total, 12 different plasmids were produced, each containing one of three promoters (see below) combined with either eGFP or mCherry as fluorophore, and either the genetic information for a Cre recombinase or not. The three different promoters utilized were a fragment of the synapsin promoter (Syn1.1) to drive expression in all neurons, a validated fragment of the glutamate-decarboxylase 67 (GAD67) promoter to drive expression in GABAergic cells [90], and a validated fragment of the Calcium/calmodulin- dependent protein kinase type II (CamKII α) promoter to drive expression in glutamatergic neurons [89]. Two different fluorophores were chosen to ensure versatile application of the final particles, even in reporter mouse lines where green or red fluorophores might be expressed endogenously. The production of the viral particles was carried out in HEK293T cells (Figure 15). To do so, the cells were transfected with four different plasmids at once: one of the cloned LV plasmids and helper plasmid needed for packaging and production of the lentiviral particles in eukaryotic cells.

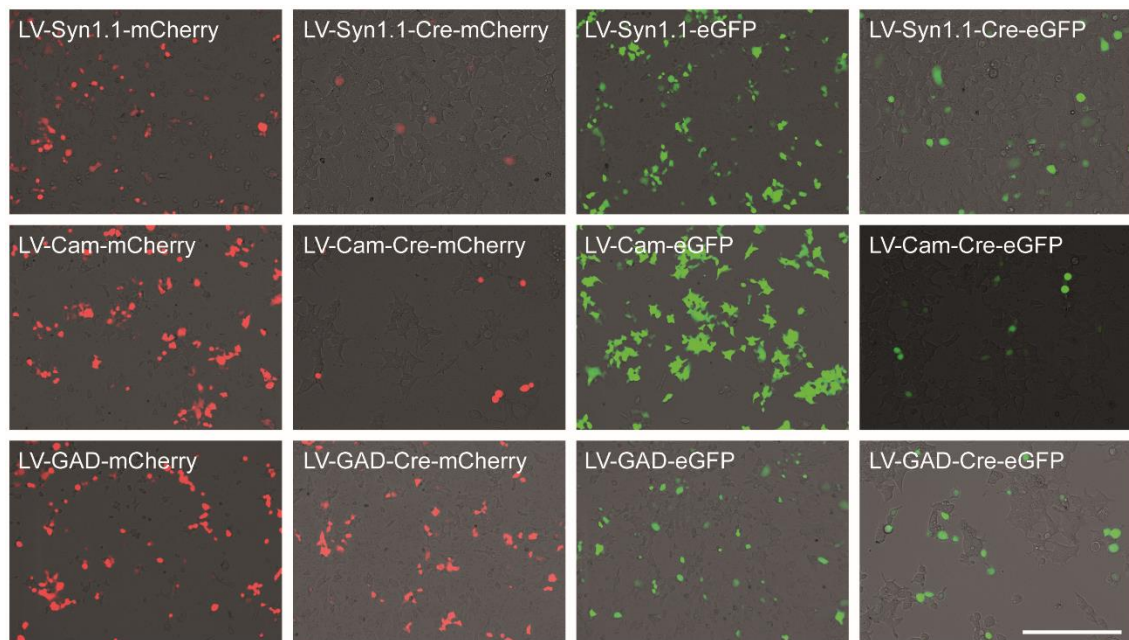


Figure 15 HEK293T cells producing lentiviral particles. Images of HEK293T cells 24 h after transfection with one of 12 different LV constructs and helper plasmids. The expression of the fluorophore (mCherry = red or eGFP = green) indicates that transfection has been successful. Scale bar = 400 μ m.

From the cell culture supernatant, the ready-to-use lentiviral particles were harvested on two consecutive days, concentrated, stored on -80°C and are now accessible to the whole group.

In addition to preparing tools for *in vivo* experiments, a novel *in vitro* model to study theta rhythm generation was established, whereby the septo-hippocampal complex is prepared from the intact brain. This preparation was acquired in cooperation with the Bernard group in Marseille and refined for the current thesis. The advantage of a preparation containing the hippocampus as well as the septal complex is that spontaneously occurring oscillations in the theta frequency band can be investigated [97, 107-109]. In addition, oscillations can also be induced experimentally. Therefore, the preparation of the intact septo-hippocampal complex has also been established in the current work, adapting different protocols [44, 97]. First, animals were anaesthetized and decapitated. The brain was removed and submerged into ice cold extracellular solution (Figure 16A). Using a scalpel, the frontal part of the neocortex and the cerebellum were removed and the brain was placed on the rostral cut surface (Figure 16B). The brain was then fixed by sticking a hand-made plastic forceps into the remaining brainstem/midbrain region and a plastic spatula was used to dissociate these regions from the surrounding cortex (Figure 16C). Then, the brain was flipped on the dorsal side (Figure 16D) and the spatula was used to set a cut just anterior to the hypothalamus, thereby removing remaining brainstem, midbrain, hypothalamus and major parts of the diencephalon (Figure 16E). When flipping back the brain to the rostral cut surface, the hippocampus as well as the septal complex were visible already. Using the two plastic spatulas, the hippocampus was loosened by gently sliding one of the spatulas under either the right or the left fimbria of the hippocampus and thereby dissociating it from the cortex (Figure 16F). After this step was repeated on the contralateral side, the septo-hippocampal complex could be dissociated from the remaining cortex. This was achieved by holding down the cortex with one spatula, while using the other spatula to slide beneath the complex and lift it into anterior-dorsal direction (Figure 16G). Figure 16H and 16I show the intact septo-hippocampal complex from a caudal and rostral point of view, respectively. Preliminary experiments I performed at the laboratory of Christophe Bernard in Marseille showed that the preparations are viable, exhibit spontaneous oscillations, and patch clamp measurements of septal neurons can be combined with recording local field potentials in the hippocampus (data not shown).

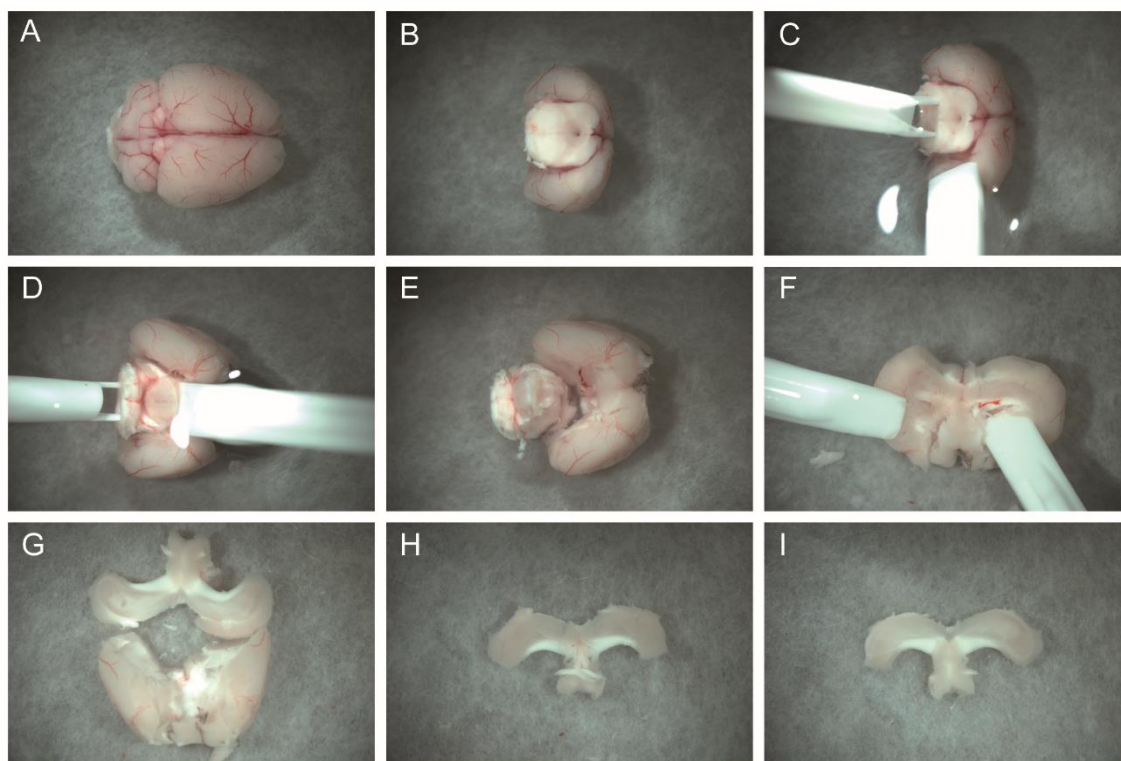


Figure 16 Complete septo-hippocampal preparation. Step-by-step preparation of the intact septo-hippocampal complex. For details, see text.

4.3 The influence of TPC1 and TPC2 on spontaneous synaptic transmission

In a first step, the distribution of TPC1 and TPC2 in the murine brain was examined. Since antibodies of comparably good quality for both channel subtypes are lacking and a low central expression was expected, qPCR was the method of choice to detect TPC transcripts in the murine brain. To this end, one week ($n = 3$) and 8 week ($n = 2$) old male mice were sacrificed and decapitated. After removal of the brain, the regions of interest (see Figure 17) were carefully separated and processed for qPCR.

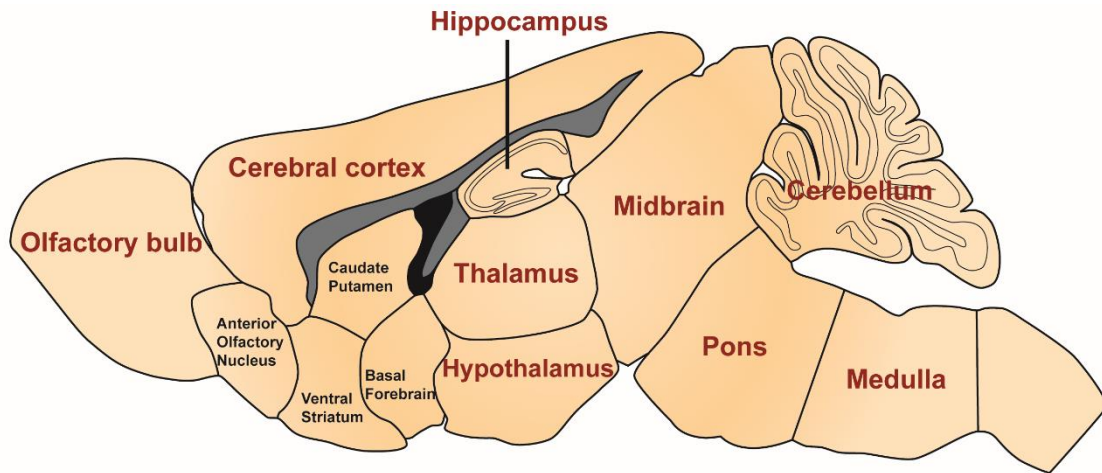


Figure 17 Schematic of the murine brain. Sagittal section of the murine brain close to the midline. For clarity, the brain areas are depicted without much detail. The regions used for qPCR are labelled in red. Importantly, the brainstem, consisting of medulla, pons and midbrain, was prepared and evaluated as one structure. The two gray regions represent two heavily myelinated structures, the corpus callosum and the fornix. The black structure represents the lateral ventricle.

The relative quantification was carried out using the ubiquitously expressed hypoxanthine-guanine phosphoribosyltransferase (HPRT) as reference gene, since its expression was more stable across the different animals and brain regions than the expression of glyceraldehyde 3-phosphate dehydrogenase (GAPDH). At one week of age, TPC1 was found to be expressed moderately in all brain regions tested, with highest relative expression in the cerebellum and hippocampus and lowest in the cerebral cortex. Expression of TPC1 appeared to be slightly reduced in older mice (Figure 18A). In comparison, TPC2 was expressed only at very low levels, close to the detection limit (Figure 18B). As for TPC1, in one week old animals the expression of TPC2 appeared to be highest in cerebellum and lowest in the cortex. In older animals, TPC2 expression was similar or slightly reduced and in case of the cerebellum it appeared to be slightly enhanced. Since the focus was laid on a qualitative rather than a quantitative statement and due to the low n-numbers, statistical tests for significance were not performed.

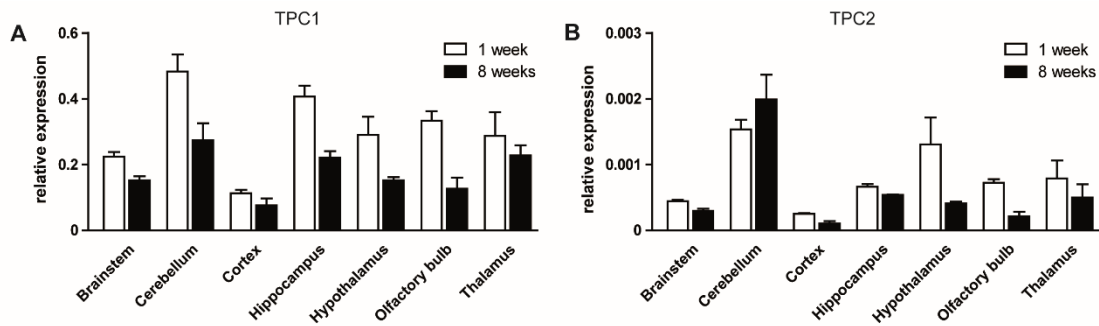


Figure 18 Expression of TPCs in different brain regions at two ages. **(A)** TPC1 is moderately expressed across all regions tested at both ages (1 week = white bars; 8 weeks = black bars). **(B)** Transcripts of TPC2 are less frequent and in general at a very low level in the murine brain at 1 week (white bars) and 8 weeks (black bars) of age. All values are quantified in relation to HPRT expression in the corresponding brain region and all data are presented as mean \pm SEM. Three (1 week) or two biological (8 weeks) and two technical replicates were used for qPCR experiments.

It appeared that both TPC isoforms are expressed throughout the entire murine brain, although to a different extent depending on the channel family member and the brain regions analyzed. Over the last decade, evidence that TPCs might be implicated in vesicular fusion processes and regulation of endo/lysosomal trafficking, accumulated [57, 110, 111]. Furthermore, pilot experiments suggested that two-pore channels might also be involved in regulation of synaptic function, especially in the hippocampus and the pre-Böttinger complex (PreBötC). Hence, the possible influence of neuronal TPCs on this function was addressed in the present thesis in more detail.

The hypothesis, that TPCs have influence on spontaneous synaptic vesicle release and vesicle content was tested by analyzing miniature postsynaptic currents (mPSCs) in either the hippocampus or the PreBötC recorded from acute brain slices. These currents reflect the postsynaptic response to neurotransmitter released by the presynapse via vesicles fusing with the presynaptic membrane. The mPSCs persisted in presence of the voltage-gated sodium channel blocker TTX, which was added to the extracellular solution in all experiments. Hence, mPSCs are not dependent on voltage changes and therefore reflect spontaneous fusion of vesicles to the presynaptic membrane. Furthermore, postsynaptic currents can arise from the release of excitatory as well as inhibitory neurotransmitters and are then called mEPSCs or mIPSCs, respectively. To isolate the two forms of mPSCs in different experiments, multiple blockers were used. Excitatory currents were obtained by adding strychnine and bicuculline to inhibit PSCs arising from glycine and GABA. On the other hand, AP5 (NMDA receptor antagonist) and CNQX (AMPA/kainate receptor antagonist) were applied to record mIPSCs. The mPSCs were analyzed regarding their occurrence (frequency), their amplitude and their kinetics (10% - 90% rise time and 10% - 90% decay time) (Figure 19).

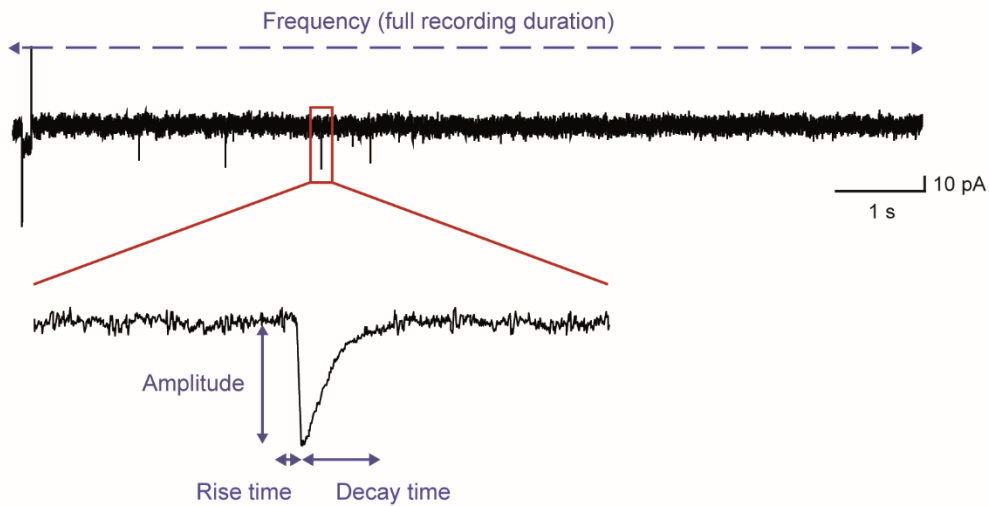


Figure 19 miniature postsynaptic parameters analyzed. Miniature postsynaptic currents were recorded from acute brain slices of WT, TPC1 KO and TPC2 KO animals. The current trace shown is taken from a TPC1 KO recording. The frequency was determined as the number of events / time. The magnification shows a schematic of an excitatory miniature postsynaptic current. The software determined the amplitude, the 10-90% rise time and the 10-90% decay time automatically from the selected currents.

In a first experiment, mPSCs were recorded from hippocampal CA1 pyramidal neurons of WT and TPC1 KO littermate animals. mEPSCs occurred with a similar frequency in WT ($n = 52$) as well as in TPC1 KO ($n = 33$) neurons (0.42 ± 0.04 Hz and 0.44 ± 0.08 Hz, $p > 0.05$) (Figure 20A). Likewise, the amplitudes of the currents were not significantly different and determined to be 27.25 ± 0.99 pA for WT and 25.92 ± 1.38 pA for TPC1 KO cells (Figure 20B). The current kinetics, reflected by rise time and decay time of the currents also turned out to be statistically indistinguishable (rise time: 1.71 ± 0.07 ms in WT and 1.57 ± 0.08 ms in TPC1 KO animals; decay time: 4.91 ± 0.16 ms in WT and 4.85 ± 0.37 ms in TPC1 KO animals)(Figure 20C). In a next step, the mIPSCs were analyzed from 4 WT and 5 TPC1 KO neurons. As for mEPSCS, neither the frequencies (0.41 ± 0.27 Hz in WT and 0.52 ± 0.21 Hz in TPC1 KO), the amplitudes (40.72 ± 6.10 pA and 43.72 ± 3.82 pA), nor the kinetics (rise time: 3.35 ± 0.23 ms and 3.78 ± 0.36 ms; decay time: 28.19 ± 3.10 ms and 51.45 ± 13.33 ms) did differ significantly in the two genotypes (Figure 20D-F).

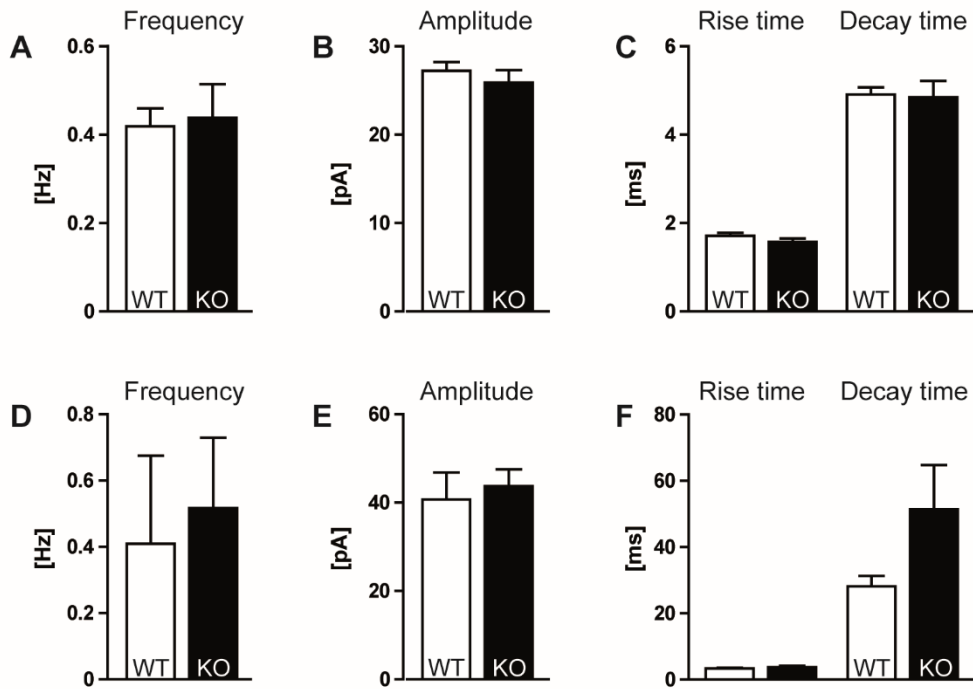


Figure 20 mPSCs in hippocampal CA1 pyramidal neurons (TPC1). **(A-C)** mEPSCs in hippocampal pyramidal CA1 neurons of WT and TPC1 KO animals. They occur with the same frequency **(A)**, exhibit a similar amplitude **(B)** and indistinguishable kinetics **(C)**. **(D-F)** mIPSCs in hippocampal CA1 neurons of the two genotypes. Likewise, the parameters assessed appeared to be similar in both genotypes. Data are presented as mean \pm SEM.

In a next step, the recordings of hippocampal mPSCs were also carried out in TPC2 KO animals and corresponding WT littermates. To investigate the influence of knock out of TPC2 on mEPSCs, currents of 25 WT and 17 TPC2 KO neurons were analyzed. The frequency of mEPSCs turned out to be similar in both genotypes (0.19 ± 0.03 Hz in WT and 0.23 ± 0.07 Hz in TPC2 KO animals) (Figure 21A). The same was true for the current amplitudes (19.77 ± 1.34 pA and 21.22 ± 1.86 pA) (Figure 21B) and kinetics (rise time: 1.79 ± 0.10 ms and 1.65 ± 0.11 ms; decay time: 5.04 ± 0.86 ms and 4.50 ± 0.58 ms) (Figure 21C). When mIPSCs were examined (WT: $n = 21$; TPC2 KO: $n = 6$), the frequencies determined were 0.32 ± 0.07 Hz in WT and 0.36 ± 0.07 Hz in TPC2 KO neurons ($p > 0.05$) (Figure 21D). Moreover, the amplitudes of the mIPSCs were similar as well (33.77 ± 2.58 pA and 34.44 ± 1.63 pA) (Figure 21E). Likewise, the currents' rise times did not differ between the two genotypes and were determined to be 2.75 ± 0.23 ms in WT and 2.81 ± 0.29 ms in TPC2 KO animals. Lastly, the decay times of WT currents (21.81 ± 2.03 ms) and TPC2 KO currents (26.83 ± 2.32 ms) were similar as well (Figure 21F).

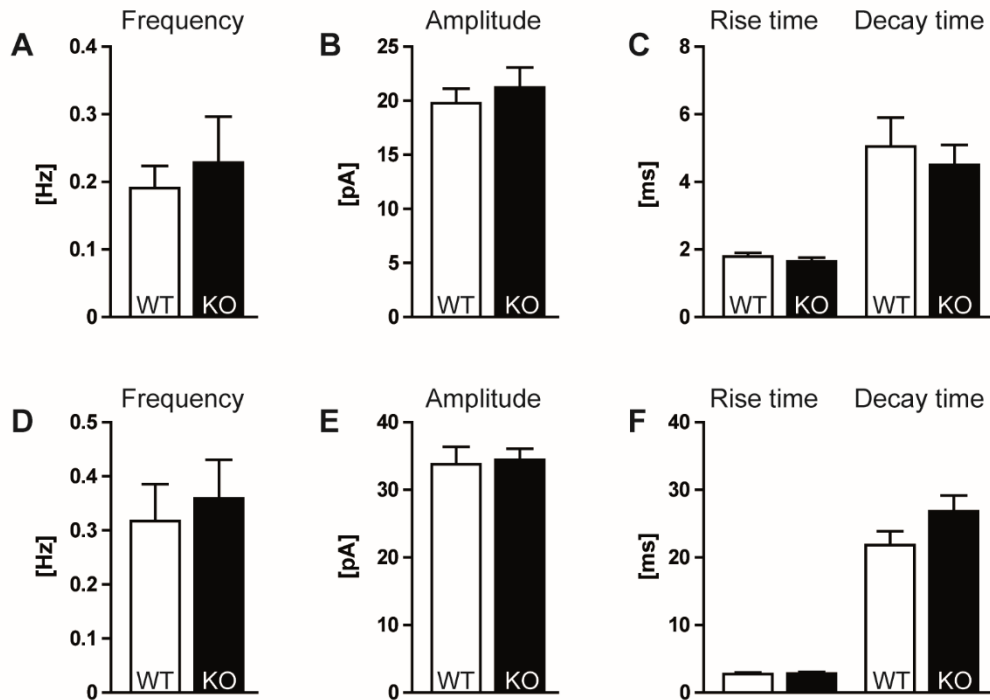


Figure 21 mEPSCs in hippocampal CA1 pyramidal neurons (TPC2). **(A-C)** mEPSCs in hippocampal pyramidal CA1 neurons of WT and TPC2 KO animals. They occur with the same frequency **(A)**, exhibit a similar amplitude **(B)** and indistinguishable kinetics **(C)**. **(D-F)** mIPSCs in hippocampal CA1 neurons of the two genotypes. The parameters assessed were similar in both groups. Data are presented as mean \pm SEM.

In further experiments, miniature postsynaptic currents in neurons of the PreBötC were analyzed. Interestingly, when comparing currents of WT animals to the ones of TPC1 KO animals it appeared that the frequency of mEPSCs was significantly increased in TPC1 KO animals (2.51 ± 0.47 Hz, $n = 12$) compared to control WT littermates (1.04 ± 0.42 , $n = 9$) (Figure 22A), while the difference in amplitudes did not differ significantly (WT: 15.79 ± 2.24 pA; TPC1 KO: 21.19 ± 1.67 pA) (Figure 22B). In addition, the currents measured in both groups exhibited comparable kinetics, reflected by similar rise times (WT: 0.96 ± 0.09 ms; TPC1 KO: 0.85 ± 0.05 ms) and decay times (WT: 2.23 ± 0.15 ms; TPC1 KO: 2.55 ± 0.19 ms) (Figure 22C). Intriguingly, a difference in the frequency of mIPSCs could not be found, since inhibitory currents occurred in WT neurons ($n = 17$) with a frequency of 0.67 ± 0.12 Hz and in TPC1 KO cells ($n = 11$) with 0.67 ± 0.23 Hz (Figure 22D). The amplitudes of mIPSCs (60.81 ± 10.43 pA for WT and 53.51 ± 10.51 pA for TPC1 KO) did not differ either (Figure 22E). Likewise, the rise times were determined to be 2.06 ± 0.25 ms in WT neurons and 1.69 ± 0.23 ms in TPC1 KO cells and a significant difference was not found. Neither did the decay times of the currents diverge significantly when comparing mIPSCs of WT (19.61 ± 2.26 ms) and of TPC1 KO cells (15.02 ± 3.24 ms) (Figure 22F).

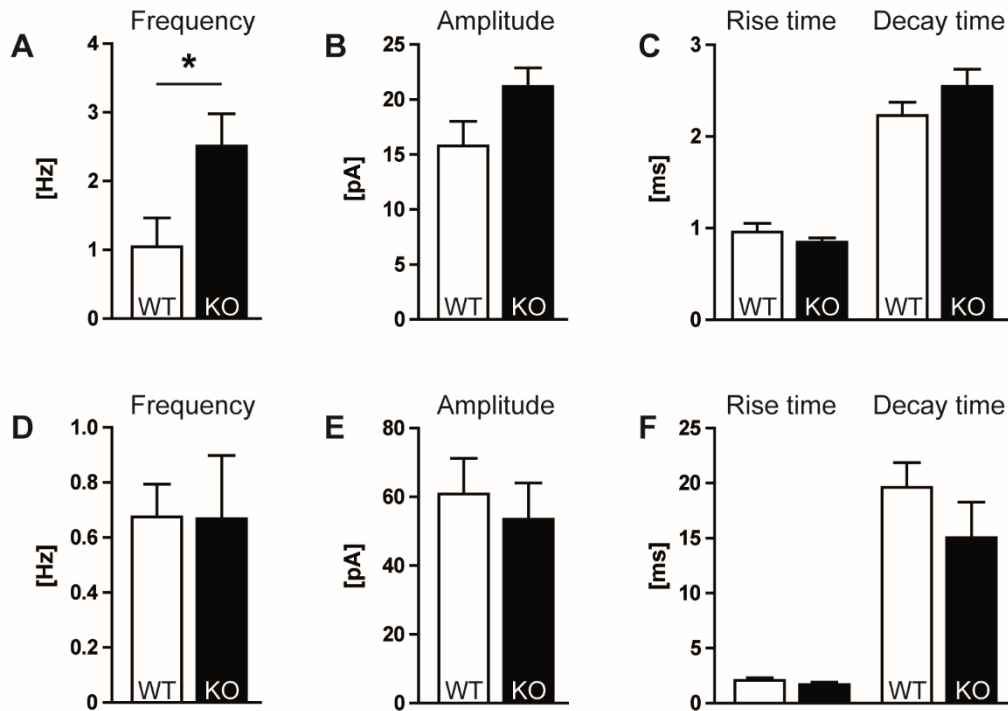


Figure 22 mEPSCs in neurons of the PreBötC (TPC1). **(A-C)** mEPSCs in PreBötC neurons of WT and TPC1 KO animals. mEPSCs are significantly increased in TPC1 KO neurons compared to WT cells **(A)**. However, they exhibit a similar amplitude **(B)** and indistinguishable kinetics **(C)**. **(D-F)** mIPSCs in PreBötC neurons of the two groups. All parameters assessed appeared to be similar in both genotypes. Data are presented as mean ± SEM. * $p < 0.05$.

Finally, miniature postsynaptic currents were also assessed in PreBötC neurons of TPC2 KO animals and their WT littermates. The analysis of mEPSCs revealed that all parameters measured did not differ between WT ($n = 6$) and TPC2 KO ($n = 4$) neurons. They occurred at similar frequencies (0.99 ± 0.38 Hz in WT and 1.21 ± 0.81 Hz in TPC2 KO), exhibited comparable amplitudes (WT: 19.39 ± 3.68 pA; TPC2 KO: 19.77 ± 4.64 pA) and the kinetics (rise time: WT: 0.65 ± 0.08 ms, TPC2 KO: 0.81 ± 0.13 ms; decay time: WT: 1.78 ± 0.16 ms, TPC2 KO: 2.52 ± 0.35 ms) were similar as well (Figure 23A-C). The same was true when examining mIPSCs in PreBötC neurons of the two groups. The frequencies were 0.49 ± 0.29 Hz in WT ($n = 4$) and 0.60 ± 0.12 Hz in TPC2 ($n = 5$) neurons. They displayed statistically indistinguishable amplitudes (WT: 23.83 ± 4.03 pA, TPC2 KO: 48.44 ± 25.54 pA) as well as rise and decay times (WT: rise time: 1.59 ± 0.40 ms, decay time: 20.85 ± 6.98 ms; TPC2 KO: rise time: 1.50 ± 0.36 ms, decay time: 18.54 ± 2.17 ms) (Figure 23D-F).

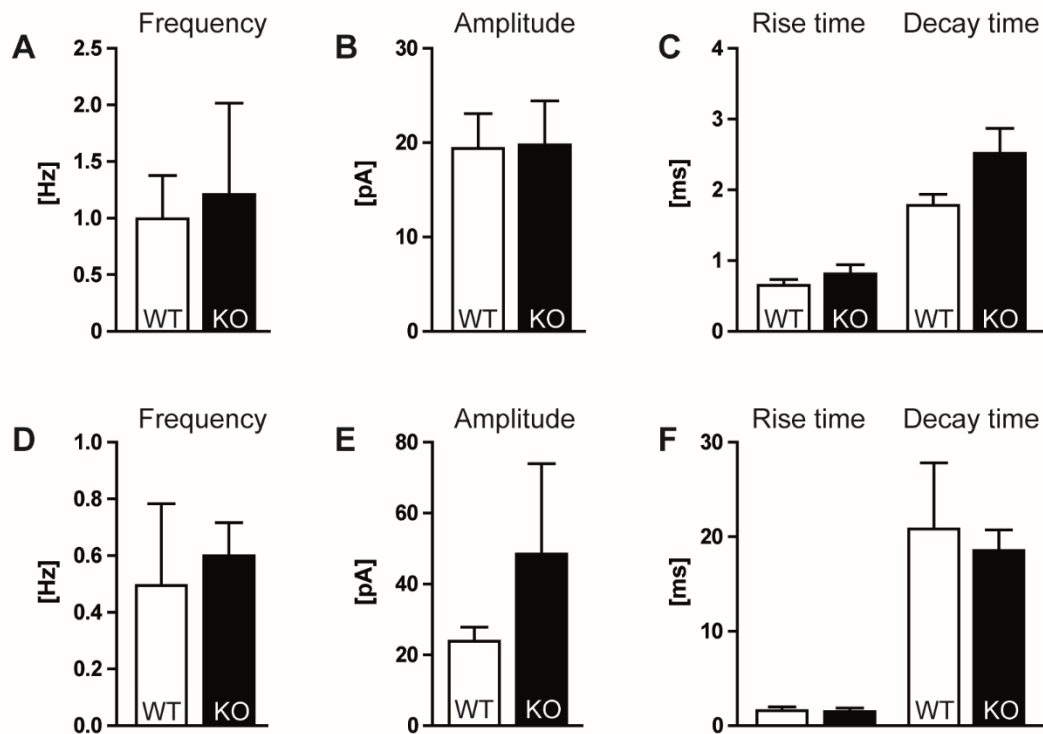


Figure 23 mPSCs in neurons of the PreBötC (TPC2). **(A-C)** mEPSCs in PreBötC neurons of WT and TPC2 KO animals did not differ in their frequency **(A)**, amplitude **(B)** or kinetics **(C)**. **(D-F)** mIPSCs in PreBötC neurons of the two groups. All parameters assessed appeared to be similar in both genotypes. Data are presented as mean \pm SEM.

Taken together, it appeared that only the knockout of TPC1 has an influence on spontaneous synaptic vesicle release, reflected by a higher frequency of mEPSCs in the PreBötC of TPC1 KO animals. Interestingly, this effect appears to be dependent on the brain region (hippocampus vs. PreBötC) as well as on the nature of the synapse (inhibitory vs. excitatory). Furthermore, a change in frequency was only found in TPC1 KO neurons and not in TPC2 KO neurons of the PreBötC. The amplitudes of the postsynaptic currents were similar in all experiments tested, indicating that TPCs apparently have no influence on the content of neurotransmitter vesicles. Similarly, the rise and decay time of the currents were similar between the groups (WT vs. TPC1 KO and WT vs. TPC2 KO), providing an indication that the composition and density of postsynaptic receptors remained unchanged upon knockout of either channel.

5 Discussion

The current thesis focuses on the examination of two families of second messenger-activated cation channels in the mouse CNS and how their knockout influences basic neuronal functions as well as behavioral aspects. In addition, new tools to study the role of HCN2 channels in theta rhythm generation are established.

5.1 HCN3 and its role in regulating murine behavior

5.1.1 Expression of HCN3

Among the four members of the HCN channel family, HCN3 is the least studied channel. Especially regarding the murine brain, studies investigating the expression of the channel, as well as the physiological role of HCN3 are largely missing. Therefore, in a first step, the presence of HCN3 channels in the murine brain was examined by immunohistochemistry. In line with previous work from this lab [34], HCN3 was found to be expressed in the murine CNS among several brain regions. HCN3 protein was detected in hypothalamic areas as the paraventricular nucleus, some thalamic nuclei such as the IGL, but also in brainstem nuclei and parts of the limbic system (amygdala and hippocampus). Furthermore, HCN3 can be found in the olfactory bulb, cortex, striatum, cerebellum and retina to name a few. These findings are in line with several studies that looked at HCN3 protein or mRNA expression in distinct areas of the CNS, where the channel was for example found in retina [112], IGL [29], or olfactory bulb [21]. Interestingly, comparing these results to a large study that examined the expression of all HCN members in the rat brain [23], HCN3 expression is conserved in many brain areas and nuclei across both species. In line with the present study, Notomi and Shigemoto demonstrated moderate to strong HCN3 expression in the olfactory bulb, hypothalamic areas such as the paraventricular nucleus, thalamic structures including the IGL and habenula, or the brainstem raphe nuclei. Likewise, low to moderate expression of HCN3 channels was found in the cerebellum, hippocampus or amygdala of the rat brain. Nevertheless, brain areas where the expression of HCN3 appears to differ between the two species exist as well. Exemplarily, in the SCN of the rat brain Notomi and Shigemoto describe moderate HCN3 expression, whereas in the present study it was shown that HCN3 signal is clearly absent in the SCN of mice. The overlapping expression of HCN3 in many shared brain regions might suggest a similar role of the channel in both species. To what extent this holds true and how exactly HCN3 channels influence physiology and behavior, especially in the rat, needs to be determined in future experiments.

5.1.2 Influence of HCN3 on auditory cued fear conditioning

In a next step, the role of HCN3 channels in regulating complex murine behavior was assessed. Former experiments using WT and HCN3 KO animals revealed only very mild phenotypes of the HCN3 KO animals. Using the rotarod it was shown that HCN3 KO animals display normal motor learning and coordination. Furthermore, anxiety-related behavior appeared to be unchanged when tested in the elevated plus maze or the dark-light transition test. In addition, stress-coping, which was tested with the forced swimming paradigm, and hippocampus dependent navigation learning (Morris water maze) were similar as well. Interestingly, HCN3 KO animals buried more marbles in the marble burying test, a behavioral task to test for motor stereotypies. Additionally, in the open field horizontal movement was slightly reduced on the second day of exposure, however, reduction of movement was similar in both genotypes when comparing day 1 and day 2 of exposure. All other parameters were unchanged [34, 102, 113]. Given the expression of HCN3 in the basolateral amygdala and the hippocampus, both important brain areas for learning and expression of conditioned fear, HCN3 KO and WT littermates were tested in the auditory cued fear conditioning paradigm for the present thesis. Therefore, mice were conditioned to a tone using a foot shock. After conditioning the animals were exposed to a novel (neutral) context and the conditioning context again. The paradigm revealed that HCN3 KO animals show impaired processing of contextual fear upon repeated (re)exposure to the conditioning and the neutral context. It appears, that from day 2 to day 8 of the paradigm, WT animals show extinction of the contextual fear, whereas HCN3 KO animals fail to do so. Furthermore, HCN3 KO animals show increases in freezing behavior in the neutral context from day 1 to day 7, whereas WT animals do not. This could be interpreted as the development of a generalized fear in HCN3 KO animals, since the formerly neutral context now produces a sustained fear response. Explanations for the observed phenotype can be manifold. Firstly, picking up the animals by their tail might be a sufficient stressful stimulus to induce context generalization in HCN3 KO animals. Secondly, the observed failure to decrease freezing behavior in the neutral context could be attributed to second-order conditioning. In this form of conditioning, the animals learn to associate the neutral context to the aversive tone during testing at day 1. Thirdly, an unspecific increase in general anxiety would also explain the observed effects. Alternatively, one might assume that general changes in locomotor activity or habituation processes can explain the observed phenotype, however, given that both groups of animals show similar decreases in activity over two consecutive exposures to the open field, this seems rather unlikely. Further, changes in auditory function of HCN3 KO animals might influence the obtained results. Although auditory function in HCN3 KO animals has not been studied in the present thesis, a major

auditory phenotype can be ruled out, given that freezing behavior upon tone presentation was similar in both groups. Although subtle differences in auditory function still might exist, they should not interfere with the paradigm used. Lastly, differences in pain perception could, to some extent, account for changes in the effectivity of the fear conditioning paradigm. It is known, that HCN channels (especially HCN1 and HCN2) are expressed at mRNA and protein level in dorsal root ganglia of several rodent species, including mice and rats [114-116]. One study found evidence that HCN2 channels are involved in the regulation of inflammatory and neuropathic pain [117]. However, evidence that HCN channels play a role in mediating acute somatosensory nociceptive pain, the type of pain important for fear conditioning, are lacking. In addition, the study of Emery and colleagues [117] found that pain reactions towards acute mechanical and heat stimuli are not affected by application of the non-selective HCN channel blocker ZD7288, which argues against an involvement of HCN channels in regulation of acute somatosensory nociceptive pain.

Regarding the biological processes underlying the observed phenotypes of increased fear generalization and impairments in fear extinction in the present study and the enhanced marble burying previously found [34] a contribution of corticothalamic projections to the observed phenotypes appears to be a likely explanation, since: first, Kobayashi and colleagues showed a close correlation between (pharmacologically) enhanced monoamine levels in the medial prefrontal cortex (mPFC) and alterations in marble burying [118]. Second, several studies suggested that the mPFC plays a role in fear extinction [119]. And third, projections from the mPFC to the thalamus are implicated in the generalization of contextual fear [120]. In line with this is the finding of Wang and colleagues, who showed that HCN channels are present in dendritic spines of mPFC neurons [121]. Furthermore, as stated above, HCN3 channels are expressed in the basolateral amygdala and hippocampus of mice and rat, both regions important for the formation of associative memory, learning, and expression of fear. On the cellular level, HCN channels have been associated with multiple physiological processes in the brain, such as controlling of the excitability of a given neuron by setting the resting membrane potential, as well as synaptic integration and plasticity. Therefore, deletion of HCN3 might change the activity of brain cells in the amygdala or hippocampus, thereby disturbing proper processing of learned fear. Still, future studies will need to reveal how exactly HCN3 channels in these brain areas are involved in the regulation of fear learning, expression, and generalization.

5.1.3 HCN channels in the intergeniculate leaflet and their influence on circadian behavior

In line with a previous study from Ying et al. [29] it could be confirmed that HCN3 channels are expressed in the IGL, whilst sparing the key player of circadian regulation, the SCN. In previous studies it has been demonstrated that the IGL is an important nucleus upstream of the SCN, integrating photic as well as non-photoc information to the SCN and thereby likely influencing circadian behavior [32]. This seems plausible, since the IGL receives input from several brain regions implicated in the regulation of arousal, sleep, stress and food intake [122]. Within the framework of the current thesis, the hypothesis, that the knockout of HCN3 channels influences the circadian regulation in the mouse, was tested. Activity profiles of WT and HCN3 KO animals revealed, that circadian locomotor behavior was unchanged under standard 12h:12h light-dark conditions and, furthermore, the same was true when animals were kept in conditions, where the light was switched on constantly (LL). This indicates, that under normal light-dark and constant light conditions, HCN3 channels play a negligible role in regulating locomotor behavior. Interestingly, when held under constant darkness conditions (DD), HCN3 KO animals display significantly less activity than their WT littermates, which suggests that HCN3 is important for reinforcing locomotor activity in the absence of light cues. Notably, whether this effect reflects improper functioning of the IGL remains inconclusive, since the animals used were global and not IGL-specific HCN3 KO mice. Possibly, changes in activity might also be mediated by other brain areas with high HCN3 expression, such as the locus coeruleus, a region critically involved in general arousal [5]. Next, when internal free-running periods of the central circadian clock were assessed under LL and DD conditions, it appeared that in none of the two experiments HCN3 KO animals behaved differently than their control WT littermates. Furthermore, light-induced resetting of the circadian clock was tested by applying light pulses during the early subjective (CT14) or late subjective (CT22) night. In both cases, the light pulse led to the expected phase delay (CT14) or phase advance (CT22) of the circadian clock [99], which was indistinguishable between the two genotypes. Using Jet lag experiments, the speed of adaptation of the clock towards a new lighting schedule was tested by advancing or delaying the LD cycle by 6 hours, a schedule mimicking situations where several time zones are skipped during longer aviation journeys. However, the time for adaptation towards both LD shifts was similar in WT and HCN3 KO animals. Although the HCN3 component of the I_h in IGL neurons might be responsible for rhythmic oscillations mediated by spontaneous low threshold spike burst firing of IGL pacemaker neurons [29], the knockout of HCN3 comes with no consequence for IGL dependent modulation of the SCN and SCN dependent circadian behavior in the presence of light cues. It might be possible, that other HCN family members undergo compensatory

upregulation which masks a possible phenotype when HCN3 is knocked out, however, so far no evidence points towards this possibility. Contrarily, a microarray study performed in 2011 argues against upregulation of HCN1, HCN2 or HCN4 in HCN3 KO animals [84].

Noteworthy, voltage clamp experiments in IGL neurons revealed that there exist different populations regarding their functional expression of HCN channels. In WT animals, ~25% of all neurons exhibited a noticeable I_h upon hyperpolarization, whereas the majority did not. Contrarily to Ying et al. [29] who suggested that other HCN channels do not significantly contribute to I_h in IGL neurons, it was found that in HCN3 KO animals still 18 of 151 neurons exhibited prominent I_h . In cases where an I_h was present, all of the parameters assessed to evaluate the currents in WT and HCN3 KO animals, like current density, time constants and half-maximal activation were similar in both genotypes. This argues for the currents in HCN3 KO animals being conducted by HCN2 channels, since HCN2 and HCN3 channels expressed in heterologous systems exhibit similar properties, whereas HCN1 channels are faster and HCN4 channels slower regarding their kinetics [123]. This conclusion is also in line with the IHC experiments performed previously [34, 102], that show expression of HCN2 channels in the mouse IGL. The similarity between the currents measured in WT and HCN3 KO animals could also explain why Ying et al. [29] drew the conclusion, that I_h in IGL neurons is almost solely carried by HCN3. In their work the currents of WT and HCN2 KO animals were compared, and no differences were detected, which, in the light of the present thesis, appears comprehensible. Still, the current work provides evidence that both HCN channel family members contribute significantly to the I_h in IGL neurons. Due to the findings of the patch clamp experiments, it appeared plausible to conduct another experiment knocking out HCN2 channels in the IGL. Using the viral approach it was possible to knock down HCN2 expression in IGL neurons. However, the circadian testing performed in injected HCN2 L2 animals revealed no obvious alterations in circadian regulation between animals injected with control or Cre-containing viral particles. It could be possible that HCN3 channels, which are expressed to a higher degree in the IGL, can compensate for the loss of HCN2 under the conditions tested. Since the dynamics of the currents measured in WT and HCN3 KO animals are similar, this might be a plausible explanation. It might therefore be interesting to knock out both channels at the same time to reduce possible compensatory effects. This could be achieved by cross-breeding HCN3 KO with HCN2 L2 animals, and repeat the injections of viral particles. In this case all HCN channel members could be deleted (or reduced) in IGL neurons and possible effects on circadian rhythms could be tested.

5.2 New tools to study theta rhythm generation

The medial septum, functioning as the main theta rhythm generator, contains mainly three different types of neurons: GABAergic, glutamatergic, and cholinergic. Except for cholinergic cells, these neurons functionally express HCN2 channels [50]. It appears, that GABAergic as well as glutamatergic neurons can drive or modulate theta rhythm generation. Although the circuits participating in the generation of theta are well known, the exact mechanisms and the proteins and ion channels involved remain largely elusive; especially the role of HCN2 in theta rhythm generation needs to be investigated in more depth [45, 109, 124].

The tools – lentiviral vectors and intact septo-hippocampal preparation – generated and established in the current thesis will help to answer the following questions when used in future experiments:

- (1) How do HCN2 channels affect the firing patterns of medial septal neurons *in vitro*?
- (2) What is the role of HCN2 for theta generation in intact septo-hippocampal preparations?
- (3) How does HCN2 influence theta generation *in vivo* and what are behavioral consequences?
- (4) Are GABAergic and glutamatergic neurons involved in theta rhythm generation to the same extent?

To answer these questions, the viral particles that were produced, will be delivered to the medial septum of HCN2 L2 mice by stereotaxic injections. With this technique it will be possible to knock out HCN2 channels only specifically in the medial septum (or any other desired part of the brain where HCN2 channels are expressed) upon the expression of Cre which is driven by the Cre-containing lentiviral particles. To analyze how the knockout of HCN2 influences firing patterns of MS neurons *in vitro*, patch clamp experiments in acute brain slices of control- and Cre-injected animals should be performed. Neurons that are transduced with control viral particles and Cre-containing particles can then be compared to evaluate the contribution of HCN2 to tonic or burst firing of these neurons. It will be of particular interest to see, whether knocking out HCN2 in the medial septum imposes similar effects on neuronal firing patterns as the knockout of HCN2 in thalamocortical neurons. Ludwig et al. [48] found that thalamocortical neurons deficient of the HCN2 channel are locked in burst mode and lose their ability to fire in tonic mode under physiological conditions. This phenomenon is most likely explained by the effect of HCN2 channels on resting membrane potential and the interplay between HCN2 and Cav3.1 T-type calcium channels. The deletion of HCN2 reduces the depolarizing current close to the resting membrane potential, which results in a shift of the potential to more hyperpolarized values. This in turn renders T-type calcium channels active, by removing the inactivating factor (relative

depolarization), which promotes low-threshold burst firing in response to incoming depolarizing inputs [48]. Using viral particles that drive Cre expression under different neuronal promoters (GAD67 promoter for GABAergic and CamKII α promoter for glutamatergic neurons), it will also be possible to investigate, whether the different neuron types are affected by the knockout of HCN2 in the same way.

Furthermore, the combination of stereotactic injection and preparing the intact septo-hippocampal preparation can be used to further deepen the understanding of theta rhythm generation and modulation. Since the intact preparation is intrinsically competent to produce theta oscillations [97, 107, 109], this approach is suitable to study aspects of theta-rhythm generation without confounding influences that might be imposed on the rhythm by brain areas not *per se* involved in the generation process. Possible experiments include the insertion of linear silicon probes (linear electrode arrays) into the dissected hippocampus, to record hippocampal depth profiles of current flow. This will give insights into hippocampal layer-specific changes in theta activity that might occur upon deletion of HCN2 in the selected neuronal population. In addition, this preparation also gives rise to the possibility of combining hippocampal depth profile analysis with simultaneous patch clamp experiments in MS neurons to decipher the firing mode of these neurons and their relation to the theta cycle. In the current thesis, the already established preparation protocols for the intact septo-hippocampal system were changed and optimized. Several studies only describe the use of the hemi-intact septo-hippocampal system, meaning that only half the septum and half the hippocampus were dissected from the ipsilateral hemisphere. This was achieved by hemi-sectioning the whole brain prior to extracting the septo-hippocampal complex [97, 107, 108]. Within the framework of the current thesis, it was possible to renounce from hemi-sectioning the brain and extract the hippocampi and the septal complex bilaterally from the intact organ. This enables the study of the whole complex, rather than only one half of it and fornix fibers from the MS to the contralateral hippocampus remain intact. Furthermore, since most preparations only use the lateral septal complex and only parts of the MS, the current preparation was optimized in such a way, that now the complete MS as well as the diagonal band of Broca (DBB) remain intact if desired. This gives rise to the opportunity of studying whether the integrity of the MS/DBB complex plays a pivotal role in theta rhythm generation, or whether the absence of the DBB leads to no changes at all. Importantly, by using the septo-hippocampal preparation as a model to study theta rhythm generation and modulation with state of the art techniques, the amount of additional *in vivo* experiments needed can be reduced to a minimum.

Finally, the different lentiviral particles can be injected into the MS of HCN2 L2 animals to study theta rhythm generation *in vivo* and whether the knockout of HCN2 has influences on murine

behavior. By using linear electrode arrays in living animals, it will be possible to not only study theta rhythm, but also how it is related to other brain rhythms that are present in living mice (e.g. gamma oscillations), and whether the knockout of HCN2 in either neuronal population changes the interplay or coupling of the different brain oscillations. Furthermore, the *in vivo* approach can be used to study the influence of HCN2 channels on vigilance states (awake, different sleep stages) and how theta, usually occurring during REM sleep, might be affected. Moreover, behavioral tests targeting MS function (e.g. object exploration paradigm) or hippocampal function (e.g. spatial navigation, social memory) can be performed to evaluate the influence of HCN2 in different neuronal subpopulations on murine behavior.

5.3 The influence of two-pore channels on spontaneous synaptic transmission

TPC1 and TPC2 are ion channels that are located on acidic intracellular organelles of the endolysosomal system. In general, this system is implicated in trafficking, recycling and breakdown of diverse intracellular molecules and proteins. TPCs were shown to be of importance for trafficking and fusion of acidic organelles and are further involved in many cellular processes such as exocytosis, nutrient sensing or autophagy [58, 73-75]. Studies from different laboratories have shown that TPCs are almost ubiquitously expressed in different tissues. They can be found in the liver, heart, kidney, spleen, testis, immune cells (macrophages), and in the brain, just to name a few [76, 77, 110, 125]. However, it also appears that the expression of TPC protein can vary in different compartments of the same organ. Exemplarily, whereas TPC1 and TPC2 mRNA are expressed in the sinus node of the heart, they are not expressed in the atria, and only TPC2 can be found in the ventricle [77]. At least for TPC2, this also seems to hold to for the brain when looking at previous work performed in this lab. Using *in situ* hybridization or RT-PCR, it could be demonstrated that TPC2 mRNA is expressed highest in the cerebellum and lowest in the cortex (of 3-5 different brain areas analyzed) [76, 77]. So far, conclusive data dealing with the expression of TPC1 in the brain is largely lacking. To fill this gap, the expression of both channel isoforms was tested in seven different areas of the mouse brain using qPCR. TPC1 mRNA was found to be expressed in all areas tested, with highest expression in the Cerebellum, followed by hippocampus, thalamus and brainstem. In the cortex, TPC1 mRNA was lowest, whereas olfactory bulb and hypothalamus showed intermediate levels of expression. In general, the levels of TPC1 mRNA were slightly higher in animals aged 1 week, compared to animals at 8 weeks of age. For TPC2 mRNA the qualitative results were quite similar, meaning that TPC2 transcripts were detected in all areas tested. In line with the aforementioned studies, highest expression was found in the cerebellum, and the lowest in the

cortex. Again, except for the cerebellum, the levels of TPC2 mRNA appeared to be slightly higher in young animals compared to 8 weeks old mice, although statistical analysis was not performed due to the low n-numbers. Furthermore, comparing the relative expression of TPC1 and TPC2 across all brain areas it appears that TPC1 mRNA transcript number is higher than TPC2 mRNA transcripts. This finding is in line with several studies that also found TPC1 mRNA to be much more abundant than TPC2 mRNA in different tissues or cell types, such as sea urchin eggs and PC12 cells [67], or different brain areas [77]. Overall, both TPC isoforms are expressed among all brain areas tested. However, as for TPC expression in the heart, it might still be the case that distinct brain nuclei or even cell types (e.g. neurons, astrocytes, oligodendrocytes, or microglia) express TPCs to a different extent. Future studies should therefore try to elucidate the expression pattern and compartmentation of TPC expression in more detail, for example by using single-cell qPCR or high-resolution imaging techniques.

Since TPCs are widely expressed in the CNS, the question arises how they are implicated in neuronal physiology. Especially neurons seem to rely on an intact endolysosomal system, which is reflected by the fact, that lysosomal storage disorders heavily impair neuronal functioning [126, 127]. The present work aimed to elucidate whether the knockout of either TPC1 or TPC2, both found in the endolysosomal system, influences aspects of basic synaptic functioning. Using patch clamp experiments in acute brain slice preparations containing the hippocampus or the pre-Bötzing complex, it was tested whether spontaneous synaptic vesicle release was changed. Here, spontaneous refers to vesicle release which is independent of action potentials, a form of vesicle release often occurring at CNS synapses [128]. In the current work, spontaneous synaptic currents were analyzed according to their origin (excitatory or inhibitory currents), their occurrence (frequency), their amplitude, and their shape (kinetics). In general, changes in the frequency of spontaneous currents point towards an altered presynapse. Changes in amplitude could be an indication for altered vesicular neurotransmitter content or a change in postsynaptic receptor density. Alterations in the kinetics of the currents would point towards changes in the composition of postsynaptic receptors [129].

In the hippocampus, the knockout of TPC1 or TPC2 did not produce any differences in spontaneous synaptic vesicle release from inhibitory or excitatory synapses when compared to release in WT animals. Miniature postsynaptic currents occurred with the same frequency and displayed statistically indistinguishable amplitudes and kinetics. However, when mPSC's were analyzed in the PreBötC, it appeared that the frequency of excitatory currents was more than doubled in TPC1 KO animals compared to WT littermates. As for currents analyzed in hippocampal neurons, in all experiments in the PreBötC, the amplitudes and kinetics of the currents were unchanged. Since only the frequency of excitatory currents was affected, the

conclusion can be drawn that TPC1 expression influences the presynapse rather than the postsynapse [129]. How can an increase in frequency of mEPSC's be possibly explained? Several mechanisms could be considered. An increase in the number of postsynaptic currents could either be mediated by more vesicles being released from the same number of synapses, or vice versa, the number of synapses that release vesicles could be increased. So far, evidence that TPCs could be responsible for an increase in synapse number is lacking. Contrarily, a recent study performed by Padamsey and colleagues [130] reported that chronically treating hippocampal slice cultures with the TPC antagonist Ned-19 leads to a change in postsynaptic dendritic spine structure and a loss of dendritic spines overall. A loss of postsynaptic spines would mean that less functioning synapses are formed, which in turn should rather decrease the occurrence of postsynaptic currents. Although it cannot be ruled out that a loss of functioning synapses would induce compensational effects at the remaining synapses, it seems more likely that the observed effect is explained by an increased spontaneous release of vesicles per synapse. Several mechanisms could underlie this effect. Firstly, since synaptic vesicle release is often dependent on calcium signals, increases in local calcium could lead to more vesicles fusing with the presynaptic membrane and releasing their contents into the synaptic cleft. TPCs are known to conduct and release calcium from organelles of the endolysosomal system [67], therefore a change in local calcium levels seems to be a plausible consequence of the knockout of TPC1. However, a loss of TPC1 as a conductor of calcium release from endolysosomal stores, would argue against local increases in Ca^{2+} , and therefore against the rise of spontaneous synaptic vesicle release due to increased Ca^{2+} levels. Secondly, the increased occurrence of mEPSC's could also be due to vesicles of the endolysosomal system fusing with neurotransmitter containing vesicles of the synapse leading to increased exocytosis of these fused vesicles. This mechanism was found recently by Parks et al. [131], who analyzed several forms of exocytosis in a mucopolipidosis type IV mouse model. Mucopolipidosis type IV is a lysosomal storage disorder resulting in severe neuronal phenotypes such as neuronal degeneration and impairments at the neuromuscular junction. Underlying the disease are mutations in the mucolipin-1 (*MCOLN1*) gene, coding for a nonselective, Ca^{2+} -permeable channel, called TRPML1, expressed in the endolysosomal system. In their study, Parks and colleagues found compelling evidence that knocking out TRPML1 leads to the fusion of lysosomes to secretory organelles in pancreatic and brain cells, and this in turn, by a yet unknown mechanism, renders the exocytosis of these vesicles uncontrollable. In their work, an increase of mEPSC's was found in acute brain slices, and an increase of glutamate release could be demonstrated in cultured cerebral cortical neurons. Whether a similar mechanism could underlie the effect seen in the present work is speculative. However, future experiments could address this issue by several means. For

example, electron microscopy could be used to test whether synaptic vesicles in TPC1 KO mice are increased in size, as is the case for synaptic vesicles in TRPML1 KO animals. Furthermore, immunohistochemistry could clarify whether lysosomal or endosomal markers (e.g. Lamp1, Rab5 or Rab7) colocalize with markers usually found on neurotransmitter vesicles, as would be the case when fusion takes place. Finally, the increase in mEPSC frequency in TPC1 KO animals could also be explained by an increase in the total number of synaptic vesicles in the synapses, a known cause for increases in spontaneous vesicle release [129]. The amount of releasable vesicles is determined by a balance between neogenesis, recycling, and degradation of synaptic vesicles [132].

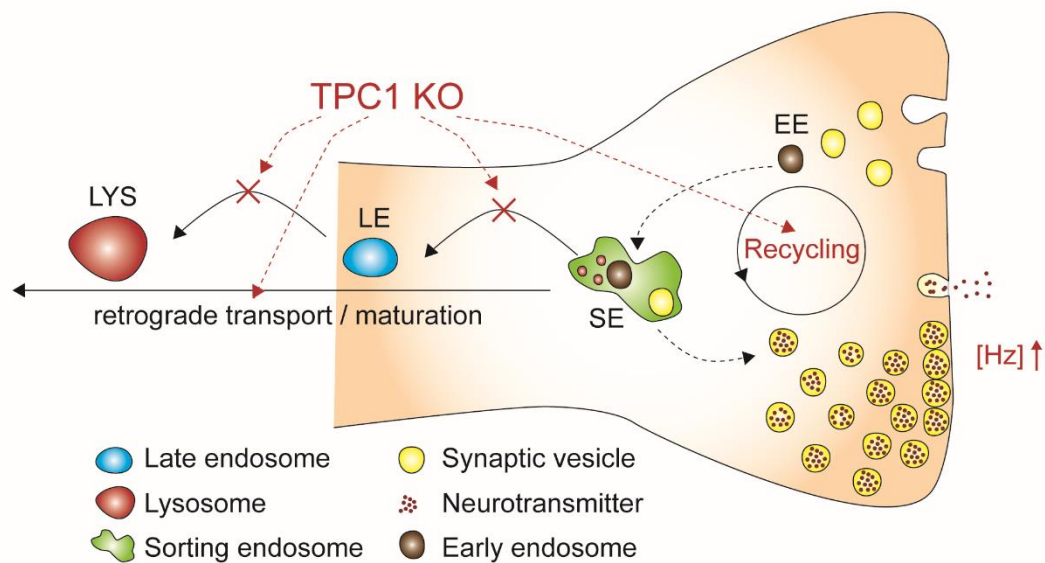


Figure 24 Possible influence of TPC1 on synaptic vesicle release. The knockout of TPC1 might influence several steps in the recycling pathway of synaptic vesicles. Local recycling of endocytosed vesicles could be increased, leading to an increase in vesicle number in the synapse. TPC1 could also be involved in the degradation pathway of synaptic vesicles by influencing fusion and maturation processes or retrograde transport to the soma per se. These processes could lead to an accumulation of synaptic vesicles in the presynapse, which in turn might increase spontaneous synaptic vesicle release. EE = early endosome; SE = sorting endosome; LE = late endosome; LYS = lysosome.

The steps where TPC1 protein is most likely involved, are local recycling of synaptic vesicles or retrograde transport of (possibly damaged and poly-ubiquitinated) vesicle components towards the soma (Figure 24). Recycling occurs in the presynapse, starting with endocytosis of presynaptic membrane [133]. The thereby formed vesicle is pushed away from the presynaptic membrane by microfilaments, and now may fuse to an endosome (early endosome). After maturation, endosomal sorting (sorting endosome) and budding, the newly recycled synaptic vesicle is now ready to be acidified and subsequently filled with neurotransmitter, before it can be reused at the active zone of the synapse [133]. Since TPC1 protein is found in several organelles along this pathway (early endosomes, sorting endosome) it seems plausible that it

might be important for proper recycling of synaptic vesicles. Although to date not much is known about the exact function of TPC1, as an ion channel permeable for Ca^{2+} it could be involved in local Ca^{2+} signaling, which is an important factor for fusion and fission processes in the endolysosomal system [134]. Disturbing the fine-tuned balance between neogenesis, recycling and degradation of synaptic vesicles might lead to an accumulation of vesicles in the presynapse, for example by enhanced recycling of endocytosed vesicles (Figure 24). Furthermore, damaged vesicle parts may be tagged for retrograde transport to the soma. Later, these particles mature to late endosomes and can fuse with lysosomes to undergo degradation. It could be that TPC1 is involved in maturation and fusion processes in this pathway and that knocking out TPC1 inhibits these processes (Figure 24). A reduced trafficking of synaptic vesicle components back to the soma could also account for an increase in available vesicles in the presynapse, followed by enhanced spontaneous exocytosis due to an increase in vesicle number [135].

As described, there are several ways how endolysosomal ion channels could interfere with spontaneous synaptic vesicle release. It will be interesting to elucidate the exact pathway and gain deeper understanding of the physiological role of TPC channels in the central nervous system in future experiments.

6 Summary

Ion channels play an exceptional role in the functioning of the central nervous system. They are involved in ion homeostasis, setting of the membrane potential and signal propagation in the brain, to name a few. Ion channels can be classified according to their gating mechanisms, the type of ions they pass, sequence homology, based on their location within the cell or combinations of the defining factors [3]. Certain families of ion channels, such as HCN and two-pore channels (TPC), are furthermore gated by second messengers. Over the last decades great efforts have been made to identify how HCN channels and TPCs are involved in regulating cellular and systemic processes in the brain. Still, the influence of (especially) HCN3 and TPC1/2 on basic neuronal functioning and complex behaviors has not been studied.

Within the framework of this thesis it was shown that HCN3 shows a relatively broad distribution in the murine brain, including areas implicated in different behaviors like fear expression and memory (amygdala and hippocampus) or circadian regulation (intergeniculate leaflet; IGL). To test whether HCN3 channels are associated with the regulation of fear, wild type and mice lacking the HCN3 channel were exposed to the fear conditioning paradigm. HCN3 KO animals show deficits in long-term processing of fear, reflected by increases in freezing behavior towards the neutral context and the inability to decrease freezing in the condition context. Due to the high expression of HCN3 in the IGL, global HCN3 KO animals were also tested for their circadian behavior. The “free-running” periods of the internal clock under constant dark (DD) or constant light conditions were similar in WT and HCN3 KO animals. The clock resetting behavior, assessed by administering light pulses during the early subjective day or night to animals that were entrained to constant darkness, did also not differ between the genotypes and neither did the capability to adapt to a new lighting schedule which was tested with the jet-lag experiment. However, the activity of HCN3-deficient animals was significantly decreased under DD conditions, pointing towards a role of HCN3 in influencing locomotor behavior in the absence of light. Whole-cell patch clamp recordings revealed that another HCN channels family member is present in IGL neurons. The number of cells displaying the I_h in HCN3 KO animals is decreased, however, all other parameters assessed (current density, kinetics, half maximal activation) are similar, pointing towards HCN2 being present in IGL neurons. Nevertheless, knocking down HCN2 channels in the IGL did not alter the circadian behavior of the animals tested. Furthermore, to study the role of HCN2 channels in the generation of neural oscillations in future experiments, new tools were developed within the framework of this thesis. Lentiviral vectors that can be used to knock down HCN2 in specific neuronal subpopulations as well as the preparation of the intact septo-hippocampal system are instruments that will help to decipher how HCN2 channels

control neuronal excitability and influence the generation of the theta rhythm *in vitro* and *in vivo*.

The other family of ion channels important for the current work are two-pore channels. TPCs are expressed on organelles of the endolysosomal system. They play a role many cellular processes, such as recycling of different molecules, trafficking and fusion of endolysosomal vesicles, autophagy or exocytosis. To date, reports on TPC expression in the central nervous system or how TPCs influence neuronal functioning are vastly lacking. qPCR experiments revealed that both TPC isoforms are expressed throughout all brain areas analyzed, with highest transcript numbers in the cerebellum, followed by thalamus, hippocampus and brain stem. In general, TPC1 appears to be more abundant in the CNS than TPC2. Furthermore, patch clamp experiments in the hippocampus and the pre-Bötzinger complex of WT, TPC1 KO and TPC2 KO animals were performed. The current thesis shows that knocking out TPC2 has no influence on number, amplitude or kinetics of spontaneously occurring excitatory or inhibitory postsynaptic currents. On the other hand, the knockout of TPC1 leads to an increase in excitatory postsynaptic currents in the pre-Bötzinger complex. Future studies will need to elucidate the mechanism leading to the observed increase.

7 Bibliography

1. Azevedo, F.A., et al., *Equal numbers of neuronal and nonneuronal cells make the human brain an isometrically scaled-up primate brain*. J Comp Neurol, 2009. **513**(5): p. 532-41.
2. Standring, S., *Gray's anatomy e-book: the anatomical basis of clinical practice*. 2015: Elsevier Health Sciences.
3. Purves, D.E., et al., *Neuroscience*. 1997.
4. Alberts, B., *Molecular biology of the cell*. 2017: Garland science.
5. Baer, M., B.W. Connors, and M.A. Paradiso, *Neuroscience: Exploring the brain*. 2007, Lippincot, Williams and Wilkins, Philadelphia.
6. Noma, A. and H. Irisawa, *A time- and voltage-dependent potassium current in the rabbit sinoatrial node cell*. Pflugers Arch, 1976. **366**(2-3): p. 251-8.
7. Halliwell, J.V. and P.R. Adams, *Voltage-clamp analysis of muscarinic excitation in hippocampal neurons*. Brain Res, 1982. **250**(1): p. 71-92.
8. Gauss, R., R. Seifert, and U.B. Kaupp, *Molecular identification of a hyperpolarization-activated channel in sea urchin sperm*. Nature, 1998. **393**(6685): p. 583-7.
9. Ludwig, A., et al., *A family of hyperpolarization-activated mammalian cation channels*. Nature, 1998. **393**(6685): p. 587-91.
10. Ludwig, A., et al., *Two pacemaker channels from human heart with profoundly different activation kinetics*. Embo j, 1999. **18**(9): p. 2323-9.
11. Santoro, B., et al., *Identification of a gene encoding a hyperpolarization-activated pacemaker channel of brain*. Cell, 1998. **93**(5): p. 717-29.
12. Biel, M., et al., *Hyperpolarization-activated cation channels: from genes to function*. Physiol Rev, 2009. **89**(3): p. 847-85.
13. Much, B., et al., *Role of subunit heteromerization and N-linked glycosylation in the formation of functional hyperpolarization-activated cyclic nucleotide-gated channels*. J Biol Chem, 2003. **278**(44): p. 43781-6.
14. Zagotta, W.N., et al., *Structural basis for modulation and agonist specificity of HCN pacemaker channels*. Nature, 2003. **425**(6954): p. 200-5.
15. Doyle, D.A., et al., *The structure of the potassium channel: molecular basis of K⁺ conduction and selectivity*. Science, 1998. **280**(5360): p. 69-77.
16. Lee, C.H. and R. MacKinnon, *Structures of the Human HCN1 Hyperpolarization-Activated Channel*. Cell, 2017. **168**(1-2): p. 111-120.e11.
17. Green, M.E., et al., *Pharmacological characterization of the inwardly-rectifying current in the smooth muscle cells of the rat bladder*. Br J Pharmacol, 1996. **119**(8): p. 1509-18.
18. Seifert, R., et al., *Molecular characterization of a slowly gating human hyperpolarization-activated channel predominantly expressed in thalamus, heart, and testis*. Proc Natl Acad Sci U S A, 1999. **96**(16): p. 9391-6.
19. El-Kholy, W., et al., *Hyperpolarization-activated cyclic nucleotide-gated channels in pancreatic beta-cells*. Mol Endocrinol, 2007. **21**(3): p. 753-64.

20. Wahl-Schott, C., S. Fenske, and M. Biel, *HCN channels: new roles in sinoatrial node function*. *Curr Opin Pharmacol*, 2014. **15**: p. 83-90.
21. Moosmang, S., et al., *Differential distribution of four hyperpolarization-activated cation channels in mouse brain*. *Biol Chem*, 1999. **380**(7-8): p. 975-80.
22. Santoro, B., et al., *Molecular and functional heterogeneity of hyperpolarization-activated pacemaker channels in the mouse CNS*. *J Neurosci*, 2000. **20**(14): p. 5264-75.
23. Notomi, T. and R. Shigemoto, *Immunohistochemical localization of Ih channel subunits, HCN1-4, in the rat brain*. *J Comp Neurol*, 2004. **471**(3): p. 241-76.
24. Mistrik, P., et al., *The murine HCN3 gene encodes a hyperpolarization-activated cation channel with slow kinetics and unique response to cyclic nucleotides*. *J Biol Chem*, 2005. **280**(29): p. 27056-61.
25. Cao-Ehlker, X., et al., *Up-regulation of hyperpolarization-activated cyclic nucleotide-gated channel 3 (HCN3) by specific interaction with K⁺ channel tetramerization domain-containing protein 3 (KCTD3)*. *J Biol Chem*, 2013. **288**(11): p. 7580-9.
26. Kanyshkova, T., et al., *Differential regulation of HCN channel isoform expression in thalamic neurons of epileptic and non-epileptic rat strains*. *Neurobiol Dis*, 2012. **45**(1): p. 450-61.
27. Battfeld, A., et al., *Distinct perinatal features of the hyperpolarization-activated non-selective cation current I(h) in the rat cortical plate*. *Neural Dev*, 2012. **7**: p. 21.
28. Kretschmannova, K., et al., *The expression and role of hyperpolarization-activated and cyclic nucleotide-gated channels in endocrine anterior pituitary cells*. *Mol Endocrinol*, 2012. **26**(1): p. 153-64.
29. Ying, S.W., et al., *PIP2-mediated HCN3 channel gating is crucial for rhythmic burst firing in thalamic intergeniculate leaflet neurons*. *J Neurosci*, 2011. **31**(28): p. 10412-23.
30. Leist, M., et al., *Two types of interneurons in the mouse lateral geniculate nucleus are characterized by different h-current density*. *Sci Rep*, 2016. **6**: p. 24904.
31. Moore, R.Y., *The geniculohypothalamic tract in monkey and man*. *Brain Research*, 1989. **486**(1): p. 190-194.
32. Delogu, A., et al., *Subcortical visual shell nuclei targeted by ipRGCs develop from a Sox14⁺-GABAergic progenitor and require Sox14 to regulate daily activity rhythms*. *Neuron*, 2012. **75**(4): p. 648-62.
33. Vrang, N., N. Mrosovsky, and J.D. Mikkelsen, *Afferent projections to the hamster intergeniculate leaflet demonstrated by retrograde and anterograde tracing*. *Brain Res Bull*, 2003. **59**(4): p. 267-88.
34. Schöll-Weidinger, M., *Charakterisierung einer HCN3-defizienten Mauslinie*. 2008.
35. Colgin, L.L., *Mechanisms and functions of theta rhythms*. *Annu Rev Neurosci*, 2013. **36**: p. 295-312.
36. Colgin, L.L., *Rhythms of the hippocampal network*. *Nat Rev Neurosci*, 2016. **17**(4): p. 239-49.
37. Vega-Flores, G., A. Gruart, and J.M. Delgado-Garcia, *Involvement of the GABAergic septo-hippocampal pathway in brain stimulation reward*. *PLoS One*, 2014. **9**(11): p. e113787.
38. Colgin, L.L. and E.I. Moser, *Hippocampal theta rhythms follow the beat of their own drum*. *Nat Neurosci*, 2009. **12**(12): p. 1483-4.

39. Pignatelli, M., A. Beyeler, and X. Leinekugel, *Neural circuits underlying the generation of theta oscillations*. *J Physiol Paris*, 2012. **106**(3-4): p. 81-92.
40. Vandecasteele, M., et al., *Optogenetic activation of septal cholinergic neurons suppresses sharp wave ripples and enhances theta oscillations in the hippocampus*. *Proc Natl Acad Sci U S A*, 2014. **111**(37): p. 13535-40.
41. Shin, J., et al., *Genetic dissection of theta rhythm heterogeneity in mice*. *Proc Natl Acad Sci U S A*, 2005. **102**(50): p. 18165-70.
42. Gangadharan, G., et al., *Medial septal GABAergic projection neurons promote object exploration behavior and type 2 theta rhythm*. *Proc Natl Acad Sci U S A*, 2016. **113**(23): p. 6550-5.
43. Freund, T.F. and M. Antal, *GABA-containing neurons in the septum control inhibitory interneurons in the hippocampus*. *Nature*, 1988. **336**(6195): p. 170-3.
44. Manseau, F., et al., *The hippocamposeptal pathway generates rhythmic firing of GABAergic neurons in the medial septum and diagonal bands: an investigation using a complete septohippocampal preparation in vitro*. *J Neurosci*, 2008. **28**(15): p. 4096-107.
45. Huh, C.Y., R. Goutagny, and S. Williams, *Glutamatergic neurons of the mouse medial septum and diagonal band of Broca synaptically drive hippocampal pyramidal cells: relevance for hippocampal theta rhythm*. *J Neurosci*, 2010. **30**(47): p. 15951-61.
46. Pape, H.C., *Queer current and pacemaker: the hyperpolarization-activated cation current in neurons*. *Annu Rev Physiol*, 1996. **58**: p. 299-327.
47. Anderson, M.P., et al., *Thalamic Cav3.1 T-type Ca²⁺ channel plays a crucial role in stabilizing sleep*. *Proc Natl Acad Sci U S A*, 2005. **102**(5): p. 1743-8.
48. Ludwig, A., et al., *Absence epilepsy and sinus dysrhythmia in mice lacking the pacemaker channel HCN2*. *EMBO J*, 2003. **22**(2): p. 216-24.
49. Kocsis, B. and S. Li, *In vivo contribution of h-channels in the septal pacemaker to theta rhythm generation*. *Eur J Neurosci*, 2004. **20**(8): p. 2149-58.
50. Xu, C., et al., *Hippocampal theta rhythm is reduced by suppression of the H-current in septohippocampal GABAergic neurons*. *Eur J Neurosci*, 2004. **19**(8): p. 2299-309.
51. Spahn, S., *Functional characterization of HCN2 channels in the septo-hippocampal system*. 2015, Ludwig-Maximilians-Universität München.
52. Brailoiu, E., et al., *An ancestral deuterostome family of two-pore channels mediates nicotinic acid adenine dinucleotide phosphate-dependent calcium release from acidic organelles*. *J Biol Chem*, 2010. **285**(5): p. 2897-901.
53. Ruas, M., et al., *Expression of Ca²⁺(+)-permeable two-pore channels rescues NAADP signalling in TPC-deficient cells*. *EMBO J*, 2015. **34**(13): p. 1743-58.
54. Calcraft, P.J., et al., *NAADP mobilizes calcium from acidic organelles through two-pore channels*. *Nature*, 2009. **459**(7246): p. 596-600.
55. Arredouani, A., et al., *Nicotinic Acid Adenine Dinucleotide Phosphate (NAADP) and Endolysosomal Two-pore Channels Modulate Membrane Excitability and Stimulus-Secretion Coupling in Mouse Pancreatic beta Cells*. *J Biol Chem*, 2015. **290**(35): p. 21376-92.
56. Ruas, M., et al., *Purified TPC isoforms form NAADP receptors with distinct roles for Ca²⁺ signaling and endolysosomal trafficking*. *Curr Biol*, 2010. **20**(8): p. 703-9.

57. Wang, X., et al., *TPC proteins are phosphoinositide- activated sodium-selective ion channels in endosomes and lysosomes*. Cell, 2012. **151**(2): p. 372-83.
58. Cang, C., et al., *mTOR regulates lysosomal ATP-sensitive two-pore Na(+) channels to adapt to metabolic state*. Cell, 2013. **152**(4): p. 778-790.
59. Ambrosio, A.L., et al., *TPC2 controls pigmentation by regulating melanosome pH and size*. Proc Natl Acad Sci U S A, 2016. **113**(20): p. 5622-7.
60. Kintzer, A.F. and R.M. Stroud, *Structure, inhibition and regulation of two-pore channel TPC1 from Arabidopsis thaliana*. Nature, 2016. **531**(7593): p. 258-62.
61. Yu, F.H. and W.A. Catterall, *The VGL-chnome: a protein superfamily specialized for electrical signaling and ionic homeostasis*. Sci STKE, 2004. **2004**(253): p. re15.
62. Patel, S., *Function and dysfunction of two-pore channels*. Sci Signal, 2015. **8**(384): p. re7.
63. Guo, J., et al., *Structure of the voltage-gated two-pore channel TPC1 from Arabidopsis thaliana*. Nature, 2016. **531**(7593): p. 196-201.
64. She, J., et al., *Structural insights into the voltage and phospholipid activation of the mammalian TPC1 channel*. Nature, 2018. **556**(7699): p. 130-134.
65. Churamani, D., et al., *The N-terminal region of two-pore channel 1 regulates trafficking and activation by NAADP*. Biochem J, 2013. **453**(1): p. 147-51.
66. Larisch, N., et al., *The function of the two-pore channel TPC1 depends on dimerization of its carboxy-terminal helix*. Cell Mol Life Sci, 2016. **73**(13): p. 2565-81.
67. Brailoiu, E., et al., *Essential requirement for two-pore channel 1 in NAADP-mediated calcium signaling*. J Cell Biol, 2009. **186**(2): p. 201-9.
68. Marchant, J.S. and S. Patel, *Two-pore channels at the intersection of endolysosomal membrane traffic*. Biochem Soc Trans, 2015. **43**(3): p. 434-41.
69. Huotari, J. and A. Helenius, *Endosome maturation*. Embo j, 2011. **30**(17): p. 3481-500.
70. Bonifacino, J.S. and B.S. Glick, *The mechanisms of vesicle budding and fusion*. Cell, 2004. **116**(2): p. 153-66.
71. Ruas, M., et al., *TPC1 has two variant isoforms, and their removal has different effects on endo-lysosomal functions compared to loss of TPC2*. Mol Cell Biol, 2014. **34**(21): p. 3981-92.
72. Sakurai, Y., et al., *Ebola virus. Two-pore channels control Ebola virus host cell entry and are drug targets for disease treatment*. Science, 2015. **347**(6225): p. 995-8.
73. Davis, L.C., et al., *NAADP activates two-pore channels on T cell cytolytic granules to stimulate exocytosis and killing*. Curr Biol, 2012. **22**(24): p. 2331-7.
74. Pereira, G.J., et al., *Nicotinic acid adenine dinucleotide phosphate (NAADP) regulates autophagy in cultured astrocytes*. J Biol Chem, 2011. **286**(32): p. 27875-81.
75. Pereira, G.J., et al., *Glutamate induces autophagy via the two-pore channels in neural cells*. Oncotarget, 2017. **8**(8): p. 12730-12740.
76. Hassan, S., *Funktionelle Charakterisierung des Two-Pore-Loop-Kanals 2 (TPC2) im endolysosomalen System*. 2014.
77. Cuny, H., *Klonierung und funktionelle Charakterisierung neuer Vertreter der Superfamilie spannungsaktivierter Kationenkanäle*. 2008.

78. Moser, M.B., D.C. Rowland, and E.I. Moser, *Place cells, grid cells, and memory*. Cold Spring Harb Perspect Biol, 2015. **7**(2): p. a021808.
79. Hartley, T., et al., *Space in the brain: how the hippocampal formation supports spatial cognition*. Philos Trans R Soc Lond B Biol Sci, 2014. **369**(1635): p. 20120510.
80. Feldman, J.L., G.S. Mitchell, and E.E. Nattie, *Breathing: rhythmicity, plasticity, chemosensitivity*. Annu Rev Neurosci, 2003. **26**: p. 239-66.
81. Feldman, J.L., C.A. Del Negro, and P.A. Gray, *Understanding the rhythm of breathing: so near, yet so far*. Annu Rev Physiol, 2013. **75**: p. 423-52.
82. Richter, D.W. and J.C. Smith, *Respiratory rhythm generation in vivo*. Physiology (Bethesda), 2014. **29**(1): p. 58-71.
83. Rovainen, C.M., *Respiratory bursts at the midline of the rostral medulla of the lamprey*. J Comp Physiol A, 1985. **157**(3): p. 303-9.
84. Fenske, S., et al., *HCN3 contributes to the ventricular action potential waveform in the murine heart*. Circ Res, 2011. **109**(9): p. 1015-23.
85. Arndt, L., et al., *NAADP and the two-pore channel protein 1 participate in the acrosome reaction in mammalian spermatozoa*. Mol Biol Cell, 2014. **25**(6): p. 948-64.
86. Scheffe, J.H., et al., *Quantitative real-time RT-PCR data analysis: current concepts and the novel "gene expression's CT difference" formula*. J Mol Med (Berl), 2006. **84**(11): p. 901-10.
87. Radonić, A., et al., *Guideline to reference gene selection for quantitative real-time PCR*. Biochemical and Biophysical Research Communications, 2004. **313**(4): p. 856-862.
88. Pfeifer, A., et al., *Delivery of the Cre recombinase by a self-deleting lentiviral vector: efficient gene targeting in vivo*. Proceedings of the National Academy of Sciences, 2001. **98**(20): p. 11450-11455.
89. Dittgen, T., et al., *Lentivirus-based genetic manipulations of cortical neurons and their optical and electrophysiological monitoring in vivo*. Proc Natl Acad Sci U S A, 2004. **101**(52): p. 18206-11.
90. Wang, S., et al., *Mechanism of nitric oxide action on inhibitory GABAergic signaling within the nucleus tractus solitarii*. Faseb j, 2006. **20**(9): p. 1537-9.
91. Akama-Garren, E.H., et al., *A Modular Assembly Platform for Rapid Generation of DNA Constructs*. Sci Rep, 2016. **6**: p. 16836.
92. Verma, I.M. and M.D. Weitzman, *Gene therapy: twenty-first century medicine*. Annu Rev Biochem, 2005. **74**: p. 711-38.
93. Delenda, C., *Lentiviral vectors: optimization of packaging, transduction and gene expression*. J Gene Med, 2004. **6 Suppl 1**: p. S125-38.
94. Paxinos, G. and K.B. Franklin, *The mouse brain in stereotaxic coordinates*. 2004: Gulf professional publishing.
95. Ying, S.W. and P.A. Goldstein, *Propofol-block of SK channels in reticular thalamic neurons enhances GABAergic inhibition in relay neurons*. J Neurophysiol, 2005. **93**(4): p. 1935-48.
96. Kuisle, M., et al., *Functional stabilization of weakened thalamic pacemaker channel regulation in rat absence epilepsy*. J Physiol, 2006. **575**(Pt 1): p. 83-100.
97. Khalilov, I., et al., *A novel in vitro preparation: the intact hippocampal formation*. Neuron, 1997. **19**(4): p. 743-9.

98. Goutagny, R., et al., *In vitro activation of the medial septum-diagonal band complex generates atropine-sensitive and atropine-resistant hippocampal theta rhythm: an investigation using a complete septohippocampal preparation*. *Hippocampus*, 2008. **18**(6): p. 531-5.
99. Jud, C., et al., *A guideline for analyzing circadian wheel-running behavior in rodents under different lighting conditions*. *Biol Proced Online*, 2005. **7**: p. 101-16.
100. Aschoff, J.C., *[Sulpiride in the prevention of migraine. A mechanism of hormonal interaction?]*. *Fortschr Med*, 1977. **95**(8): p. 523-7.
101. Kamprath, K. and C.T. Wotjak, *Nonassociative learning processes determine expression and extinction of conditioned fear in mice*. *Learn Mem*, 2004. **11**(6): p. 770-86.
102. Stieglitz, M.S., et al., *Disturbed Processing of Contextual Information in HCN3 Channel Deficient Mice*. *Frontiers in Molecular Neuroscience*, 2018. **10**.
103. Berson, D.M., F.A. Dunn, and M. Takao, *Phototransduction by retinal ganglion cells that set the circadian clock*. *Science*, 2002. **295**(5557): p. 1070-3.
104. Mrosovsky, N., *Masking: History, Definitions, and Measurement*. *Chronobiology International*, 2009. **16**(4): p. 415-429.
105. Varga, V., et al., *The presence of pacemaker HCN channels identifies theta rhythmic GABAergic neurons in the medial septum*. *J Physiol*, 2008. **586**(16): p. 3893-915.
106. Morris, N.P., R.E. Fyffe, and B. Robertson, *Characterisation of hyperpolarization-activated currents (I(h)) in the medial septum/diagonal band complex in the mouse*. *Brain Res*, 2004. **1006**(1): p. 74-86.
107. Amilhon, B., et al., *Parvalbumin Interneurons of Hippocampus Tune Population Activity at Theta Frequency*. *Neuron*, 2015. **86**(5): p. 1277-89.
108. Wong, T., et al., *Postnatal development of intrinsic GABAergic rhythms in mouse hippocampus*. *Neuroscience*, 2005. **134**(1): p. 107-20.
109. Robinson, J., et al., *Optogenetic Activation of Septal Glutamatergic Neurons Drive Hippocampal Theta Rhythms*. *J Neurosci*, 2016. **36**(10): p. 3016-23.
110. Grimm, C., et al., *High susceptibility to fatty liver disease in two-pore channel 2-deficient mice*. *Nat Commun*, 2014. **5**: p. 4699.
111. Grimm, C., et al., *Two-Pore Channels: Catalyzers of Endolysosomal Transport and Function*. *Front Pharmacol*, 2017. **8**: p. 45.
112. Muller, F., et al., *HCN channels are expressed differentially in retinal bipolar cells and concentrated at synaptic terminals*. *Eur J Neurosci*, 2003. **17**(10): p. 2084-96.
113. Mader, R., *Inaktivierung des murinen Gens des Hyperpolarisations-aktivierten Zyklonukleotid-gesteuerten Kationenkanals Typ Drei (HCN3)*. 2004.
114. Hou, B., et al., *Characteristics of hyperpolarization-activated cyclic nucleotide-gated channels in dorsal root ganglion neurons at different ages and sizes*. *Neuroreport*, 2015. **26**(16): p. 981-7.
115. Kouranova, E.V., et al., *Hyperpolarization-activated cyclic nucleotide-gated channel mRNA and protein expression in large versus small diameter dorsal root ganglion neurons: correlation with hyperpolarization-activated current gating*. *Neuroscience*, 2008. **153**(4): p. 1008-19.
116. Usoskin, D., et al., *Unbiased classification of sensory neuron types by large-scale single-cell RNA sequencing*. *Nat Neurosci*, 2015. **18**(1): p. 145-53.

117. Emery, E.C., et al., *HCN2 ion channels play a central role in inflammatory and neuropathic pain*. *Science*, 2011. **333**(6048): p. 1462-6.
118. Kobayashi, T., et al., *Neurochemical responses to antidepressants in the prefrontal cortex of mice and their efficacy in preclinical models of anxiety-like and depression-like behavior: a comparative and correlational study*. *Psychopharmacology (Berl)*, 2008. **197**(4): p. 567-80.
119. Maren, S., K.L. Phan, and I. Liberzon, *The contextual brain: implications for fear conditioning, extinction and psychopathology*. *Nat Rev Neurosci*, 2013. **14**(6): p. 417-28.
120. Xu, W. and T.C. Sudhof, *A neural circuit for memory specificity and generalization*. *Science*, 2013. **339**(6125): p. 1290-5.
121. Wang, M., et al., *Alpha2A-adrenoceptors strengthen working memory networks by inhibiting cAMP-HCN channel signaling in prefrontal cortex*. *Cell*, 2007. **129**(2): p. 397-410.
122. Morin, L.P. and J.H. Blanchard, *Descending projections of the hamster intergeniculate leaflet: relationship to the sleep/arousal and visuomotor systems*. *J Comp Neurol*, 2005. **487**(2): p. 204-16.
123. Wahl-Schott, C. and M. Biel, *HCN channels: structure, cellular regulation and physiological function*. *Cell Mol Life Sci*, 2009. **66**(3): p. 470-94.
124. Hangya, B., et al., *GABAergic neurons of the medial septum lead the hippocampal network during theta activity*. *J Neurosci*, 2009. **29**(25): p. 8094-102.
125. Ishibashi, K., M. Suzuki, and M. Imai, *Molecular cloning of a novel form (two-repeat) protein related to voltage-gated sodium and calcium channels*. *Biochem Biophys Res Commun*, 2000. **270**(2): p. 370-6.
126. Jeyakumar, M., et al., *Storage solutions: treating lysosomal disorders of the brain*. *Nat Rev Neurosci*, 2005. **6**(9): p. 713-25.
127. Platt, F.M., B. Boland, and A.C. van der Spoel, *The cell biology of disease: lysosomal storage disorders: the cellular impact of lysosomal dysfunction*. *J Cell Biol*, 2012. **199**(5): p. 723-34.
128. Kavalali, E.T., *The mechanisms and functions of spontaneous neurotransmitter release*. *Nat Rev Neurosci*, 2015. **16**(1): p. 5-16.
129. Han, E.B. and C.F. Stevens, *Development regulates a switch between post- and presynaptic strengthening in response to activity deprivation*. *Proc Natl Acad Sci U S A*, 2009. **106**(26): p. 10817-22.
130. Padamsey, Z., L. McGuinness, and N.J. Emptage, *Inhibition of lysosomal Ca(2+) signalling disrupts dendritic spine structure and impairs wound healing in neurons*. *Commun Integr Biol*, 2017. **10**(5-6): p. e1344802.
131. Park, S., et al., *Fusion of lysosomes with secretory organelles leads to uncontrolled exocytosis in the lysosomal storage disease mucopolipidosis type IV*. *EMBO Rep*, 2016. **17**(2): p. 266-78.
132. Willeumier, K., S.M. Pulst, and F.E. Schweizer, *Proteasome inhibition triggers activity-dependent increase in the size of the recycling vesicle pool in cultured hippocampal neurons*. *J Neurosci*, 2006. **26**(44): p. 11333-41.
133. Rizzoli, S.O., *Synaptic vesicle recycling: steps and principles*. *Embo j*, 2014. **33**(8): p. 788-822.

134. Shen, D., X. Wang, and H. Xu, *Pairing phosphoinositides with calcium ions in endolysosomal dynamics: phosphoinositides control the direction and specificity of membrane trafficking by regulating the activity of calcium channels in the endolysosomes*. *Bioessays*, 2011. **33**(6): p. 448-57.
135. Murthy, V.N., et al., *Inactivity produces increases in neurotransmitter release and synapse size*. *Neuron*, 2001. **32**(4): p. 673-82.

8 List of figures

FIGURE 1 SCHEMATIC OF A HCN CHANNEL SUBUNIT.....	3
FIGURE 2 STRUCTURE OF THE HUMAN HCN1 CHANNEL.....	4
FIGURE 3 MAIN PATHWAY OF THE CIRCADIAN SYSTEM IN MAMMALS INVOLVING SCN AND IGL.....	6
FIGURE 4 TOPOLOGY DIAGRAM OF A MOUSE TPC1 SUBUNIT.....	9
FIGURE 5 GRAPHIC VISUALIZATION OF THE PROTOCOL USED TO MEASURE I_H CURRENTS.....	35
FIGURE 6 FEAR CONDITIONING PARADIGM.....	43
FIGURE 7 ANALYSIS OF THE FEAR CONDITIONING EXPERIMENT.....	44
FIGURE 8 CIRCADIAN TESTING – ACTIVITY AND PERIOD LENGTH.....	45
FIGURE 9 CIRCADIAN TESTING – PHASE SHIFT AND JET-LAG.....	47
FIGURE 10 I_H IN IGL NEURONS.....	48
FIGURE 11 CURRENT DENSITY AND KINETICS OF I_H	48
FIGURE 12 ANALYSIS OF THE TAIL CURRENTS.....	49
FIGURE 13 EXAMPLES OF TRANSDUCED IGL NEURONS.....	51
FIGURE 14 CIRCADIAN BEHAVIOR OF INJECTED HCN2 L2 ANIMALS.....	52
FIGURE 15 HEK293T CELLS PRODUCING LENTIVIRAL PARTICLES.....	53
FIGURE 16 COMPLETE SEPTO-HIPPOCAMPAL PREPARATION.....	55
FIGURE 17 SCHEMATIC OF THE MURINE BRAIN.....	56
FIGURE 18 EXPRESSION OF TPCS IN DIFFERENT BRAIN REGIONS AT TWO AGES.....	57
FIGURE 19 MINIATURE POSTSYNAPTIC PARAMETERS ANALYZED.....	58
FIGURE 20 MPSCS IN HIPPOCAMPAL CA1 PYRAMIDAL NEURONS (TPC1).....	59
FIGURE 21 MPSCS IN HIPPOCAMPAL CA1 PYRAMIDAL NEURONS (TPC2).....	60
FIGURE 22 MPSCS IN NEURONS OF THE PREBÖTC (TPC1).....	61
FIGURE 23 MPSCS IN NEURONS OF THE PREBÖTC (TPC2).....	62
FIGURE 24 POSSIBLE INFLUENCE OF TPC1 ON SYNAPTIC VESICLE RELEASE.....	73

9 List of abbreviations

(m)EPSC	(Miniature) excitatory postsynaptic current
(m)IPSC	(Miniature) inhibitory postsynaptic current
(m)PSC	(Miniature) postsynaptic current
AAV	Adeno-associated virus
Amp ^R	Ampicillin resistance gene
ANOVA	Analysis of variance
AP5	2R-amino-5-phosphonovaleric acid
AtTPC1	<i>Arabidopsis thaliana</i> TPC1
BBS	Borate buffered saline
CaMKII	Calcium/calmodulin- dependent protein kinase type II
cAMP	Cyclic adenosine monophosphate
CC	Conditioning context
cDNA	Complementary DNA
CMG	Cytomegalovirus
CNBD	Cyclic nucleotide binding domain
CNQX	6-cyano-7-nitroquinoxaline-2,3-dione
CNS	Central nervous system
CO	Carbon oxide
CT	Circadian time
DBB	Diagonal band of Broca
DD	Constant darkness
ddH ₂ O	Double distilled water
dLGN	Dorsolateral geniculate nucleus
DNA	Desoxyribonucleic acid
E. coli	Escherichia coli
eGFP	Enhanced GFP
GAD	Glutamic acid decarboxylase
GAPDH	Glyceraldehyde 3-phosphate dehydrogenase
GDP	Guanosine diphosphate
GFP	Green fluorescent protein
GHT	Geniculohypothalamic tract
GT	Genotype
GTP	Guanosine triphosphate

HBSS	Hanks' balanced salt solution
HCN channel	Hyperpolarization-activated cyclic nucleotide-gated cation channel
HPRT	Hypoxanthine-guanine phosphoribosyltransferase
hSyn	Human synapsin promoter
IGL	Intergeniculate leaflet
I_h	Hyperpolarization-activated cation current
IHC	Immunohistochemistry
IP_3	Inositol trisphosphate
ITR	Inverted terminal repeat
kb	kilobases
KO	Knockout
LL	Constant light
LTR	Long terminal repeat
LV	lentiviral
MCS	Multiple cloning site
mPFC	Medial prefrontal cortex
MS	Medial septum
mTPC1	Mouse TPC1
NAADP	Nicotinic acid adenine dinucleotide phosphate
NC	Neutral context
NO	Nitric oxide
pA BGH	Polyadenylation signal of the bovine growth hormone
PBS	Phosphate buffered saline
PCR	Polymerase chain reaction
PFA	Paraformaldehyde
PI-3,5-P ₂	Phosphatidylinositol-3,5-bisphosphate
PreBötC	Pre-Bötzinger complex
qPCR	Quantitative real-time PCR
rAAV	Recombinant AAV
REM sleep	Rapid eye movement sleep
RHT	Retinohypothalamic tract
RNA	Ribonucleic acid
RT	Room temperature
RT-PCR	Reverse transcription PCR
SCN	Suprachiasmatic nucleus
SEM	Standard error of the mean

Syn1.1	1.1 kb fragment of the synapsin promoter
TC	Thalamocortical
TM	Transmembrane
TPC(s)	Two-pore channel(s)
TRP (channel)	Transient receptor potential (channel)
TSA	Tyramide signal amplification
TTX	Tetrodotoxin
vLGN	Ventrolateral geniculate nucleus
VSD	Voltage sensing domain
VSV-G	Vesicular stomatitis virus glycoprotein
WPRE	Woodchuck hepatitis virus posttranscriptional regulatory element
WT	Wild type

10 Appendix

10.1 Primers used for PCR and qPCR experiments

Primers for Genotyping

Primer name	Sequence 5' – 3'	Use
HCN2 14F	GGT CCC AGG CAC TTC CAT CCT TT	Genotyping of HCN2 L2 animals
HCN2 15R	GGA AAA ATG GCT GCT GAG CTG TCT C	Genotyping of HCN2 L2 animals
HCN2 16F	CAG CTC CCA TTT GCC CTT GTG C	Genotyping of HCN2 L2 animals
HCN3 A66F	GAG CCA CGA CTA GAT GCT GA	Genotyping of HCN3 KO animals
HCN3 RM15F	GCT CTA GAT TTG CCC AAC CTA	Genotyping of HCN3 KO animals
HCN3 RM13R	ACA CCG TCT GAA CTG ATA AGA	Genotyping of HCN3 KO animals
TPC1 138F	TCA GCT GCC TGT GAG CCA GAG	Genotyping of TPC1 KO animals
TPC1 32F	GGA GCT CAC CTG GTT GTG CCA TA	Genotyping of TPC1 KO animals
TPC1 141R	CCA TGC CTT TGA TCC CAA CAA T	Genotyping of TPC1 KO animals
TPC2 36R	GAT GAG ACC TTG TCA AGA TCG	Genotyping of TPC2 KO animals
TPC2 38R	GAG TTG AAG GCT CCA AGA GC	Genotyping of TPC2 KO animals
TPC2 33F	TCA GAC ATT ACA GAC TCA GAC C	Genotyping of TPC2 KO animals

Primers for qPCR

Primer name	Sequence 5' – 3'
TPC1 forward	TAT CAA GAG GCG GCA ATC TAC C
TPC1 reverse	AGA AGT GGT TGT GGA CGA AGA
TPC2 forward	TAA AGT ACC GCT CCA TCT ACC A
TPC2 reverse	GCA GAC GTT CGA GTA ATA CCA G
HPRT forward	GCT CGA GAT GTC ATG AAG GAG AT
HPRT reverse	AAA GAA CTT ATA GCC CCC CTT GA
WPRE forward	AGT TCC GCC GTG GCA ATA GG
WPRE reverse	CAA GGA GGA GAA AAT GAA AGC C

Primers for cloning of pAAV plamids

Primer name	Sequence 5' – 3'	Use
Primer A	CCA GCT AGC ATC GGA ATT CGC CCT TAA GC	Forward primer for amplification of hSyn from pAAV2.1-hSyn-eGFP

Primer B	GGG CAT GGT GAT CCA ATC TAT TGC TCA CCA TGG TGG C	Reverse primer to primer A
Primer C	GCC ACC ATG GTG AGC AAT AGA TTG GAT CAC CAT GCC C	Forward primer for amplification of Cre-p2A-eGFP from pAAV2.1- SWS-Cre-p2A-eGFP
Primer D	TTC TCC CAC CGT CAG TAC G	Reverse primer to primer C

Primers for cloning of LV plasmids

Primer name	Sequence 5' – 3'	Use
mCherry For	CGA CCC ACT GCC CCT TGG ATC C	Amplification of mCherry and insertion of BamHI restriction site
mCherry Rev	TAT GTC GAC TTA CTT GTA CAG CTC GTC CAT GCC G	Amplification of mCherry and insertion of Sall restriction site
CamKII For	AGG TTA ACC ATT ATG GCC TTA GGT CAC TTC ATC	Amplification of CamKII promoter and insertion of HpaI restriction site
CamKII Rev	TAT GGA TCC GCT GCC CCC AGA ACT AGG GGC	Amplification of CamKII promoter and insertion of BamHI restriction site
GAD67 For	AGG TTA ACC GTG GAT TTT GCT AAA GCC CTA GG	Amplification of GAD67 promoter and insertion of HpaI restriction site
GAD67 rev	TAT GGA TCC CGC TCC CGC GTT CGA GGA GG	Amplification of GAD67 promoter and insertion of BamHI restriction site
mCherry EcoRI For	ATG AAT TCA TGG TGA GCA AGG GCG AGG AG	Amplification of mCherry and insertion of EcoRI restriction site
mCherry Not Rev	GAT CGC GGC CGC TTA CTT GTA CAG CTC GTC CAT G	Amplification of mCherry and insertion of NotI restriction site
Cassette For	ACG ATT AGA TCT GCT GTG CGA TCG TTT ACC ATG C	Amplification of Cre-t2A-fluorophore and insertion of BglII restriction site
Cassette Rev	TGA GTC GAC CCT CTA GAT GCA TGC TCG AG	Amplification of Cre-t2a-fluorophore and insertion of Sall restriction site

Sequencing primers

Primer name	Sequence 5' – 3'	Use
Primer E	AGTGGGTCGTTCTAGTCGACC	Forward primer to sequence hSyn-Cre-p2A-eGFP
Primer F	TAACCAGCGTTTTCGTTCTGCC	Reverse primer to primer F
LV_Prom for	AGATCCATTCGATTAGTGAACG	Forward primer to sequence all LV constructs
LV_Rev2	AGCAACATAGTTAAGAATACC	Reverse primer to sequence all LV constructs

GadSeq250	CCTGACTGATGTCACTATATCTT	Forward primer to sequence the GAD67 promoter
GadSeq1212	GCCACCCTCCATGCTCTGCT	Forward primer to sequence the GAD67 promoter
GadSeq2087	CGTACTCCTGTGACAGAGCCGA	Forward primer to sequence the GAD67 promoter
Seq Cre Mid rev	CCTCCTCGCCCTTGCTCAC	Reverse primer to sequence all Cre-containing plasmids
Seq CamCre301 rev	GACGATGAAGCATGTTTAGCTG	Reverse primer to sequence constructs containing the CamKII promoter and Cre
Seq GadCre700 rev	GATCATCAGCTACACCAGAGAC	Reverse primer to sequence constructs containing the GAD67 promoter and Cre
M13 uni (-43)	AGGGTTTTCCCAGTCACGACGTT	Forward primer to sequence the TOPO vector
Seq Cret2A mid rev	GTATTGAAACTCCAGCGCGGG	Reverse primer to sequence all Cre-containing constructs

10.2 Antibodies used

Primary antibodies:

Name	Producer/antibody name	Dilution
ms anti-GFP	Neuromab 75-131	1:1000
rb anti-HCN3	Own production [24] #9495/1	1:1000
rb anti-HCN2	Alomone APC030	1:200

Secondary antibodies:

Name	Producer/antibody name	Dilution
gt anti-ms Alexa488	Invitrogen A11001	1:800
dk anti-rb HRP	Jackson 715-035-150	1:1000

10.3 Publications

Kraus TF, Kilinc S, Steinmaurer M, **Stieglitz M**, Guibourt V, Kretzschmar HA. *Profiling of methylation and demethylation pathways during brain development and ageing*. J Neural Transm, 2016

Stieglitz MS, Fenske S, Hammelmann V, Becirovic E, Schöttle V, Delorme JE, Schöll-Weidinger M, Mader R, Deussing J, Wolfer DP, Seeliger MW, Albrecht U, Wotjak CT, Biel M, Michalakis S, Wahl-Schott C. *Disturbed processing of contextual information in HCN3 channel deficient mice*. Front Mol Neurosci, 2018

Hammelmann V, **Stieglitz MS**, Hülle H, Le Meur K, Gruner C, Hartmann J, Zott B, Lüthi A, Spahn S, Zong X, Fenske S, Moser M, Isbrandt D, Ludwig A, Konnerth A, Wahl-Schott C, Biel M. *Gating of HCN2 channels by cyclic AMP controls firing pattern and information processing in thalamic nuclei*. Submitted, 2018

10.4 Acknowledgements

Zuallererst möchte ich Herrn Professor Dr. Martin Biel für die Übernahme des Zweitgutachtens und die exzellente Ko-Betreuung danken. Auch für Ihre Unterstützung und die offene Tür bei aller Art von Problemen möchte ich Ihnen danken.

Besonderer Dank gilt Prof. Dr. Christian Wahl-Schott. Danke für die Aufnahme in den Arbeitskreis und die Möglichkeit diese Dissertation zu verwirklichen. Besonders danke ich dir für dein Vertrauen, deine herausragende Betreuung, die vielen wissenschaftlichen Diskussionen und die amüsanten Nachmittage in der Laborküche.

Prof. Dr. Urs Albrecht und seinen Mitarbeitern möchte ich für die Durchführung der circadianik Experimente danken. Besonders hervorheben möchte ich Tomaz Martini, danke für die vielen Diskussionen und Telefonate.

Danke auch an Prof. Dr. Christophe Bernard und seinen Arbeitskreis für die entgegengebrachte Gastfreundschaft und Hilfe bei der Präparation.

Dr. Carsten Wotjak gilt mein Dank für die Unterstützung bei der Analyse des Experiments zur Angstkonditionierung.

Verena H, vielen Dank dass du mir unzählige Methoden näher gebracht hast und immer ein offenes Ohr für alle meine kleinen und großen Laborproblemchen hattest.

Steffi, danke für die Einführung in die Elektrophysiologie und überhaupt für den Umstand, dass ich hier gelandet bin.

Henne, auch dir danke ich für die vielen gemeinsamen Stunden am Setup und für dein offenes Ohr bei allen Hard- und Softwareproblemen.

Karim möchte ich für die nützlichen Hinweise zur Verbesserung meiner Patch clamp Technik danken.

Ella, es war eine große Freude mit dir von deiner Diplomarbeit bis jetzt zu arbeiten. Danke, dass du mir immer den Rücken freigehalten hast, ohne Dich wäre das letzte Jahr sehr viel anstrengender geworden.

Labormädels, euch allen danke ich ganz besonders für die tolle Zeit hier. Ich bin froh, dass es euch gibt und ihr den Arbeitsalltag so viel unterhaltsamer gestaltet habt. Vielen Dank auch für die eine oder andere Hilfestellung bei den mir bis dahin unbekannteren Methoden.

Auch allen anderen nicht namentlich genannten Kollegen die mich in jeder erdenklichen Weise hier unterstützt haben möchte ich gerne nochmal für die Hilfe und die gute Zeit danken.

Zu guter Letzt möchte ich der wichtigsten Person in meinem Leben danken, meiner Frau. Stephe, du hast mich unermüdlich unterstützt, mir zugehört, mir Tipps gegeben und mich niemals aufgegeben. Du bist meine Inspiration und meine Motivation und es lässt sich nicht in Worte fassen wie unendlich dankbar ich dir für alles bin.